Alma Mater Studiorum – Università di Bologna

DOTTORATO DI RICERCA IN CHIMICA

Ciclo XXXI

Settore Concorsuale: 03/A2

Settore Scientifico Disciplinare: CHIM/02

Beyond Li-ion batteries: novel concepts and designs

Presentata da: Irene Ruggeri

Coordinatore Dottorato

Prof. Aldo Roda

Relatore

Prof.ssa Catia Arbizzani

Correlatore

Prof.ssa Francesca Soavi

Esame finale anno 2019

To my family Piero, Teresa and Roberta

Table of Contents

Acknowledgments

My deepest gratitude goes to my thesis supervisors Prof. Catia Arbizzani and Prof. Francesca Soavi, who have been invaluable mentors and guided me in an exceptional way during the thesis work in the Laboratory of Electrochemistry of Materials for Energetics (LEME) of the Department of Chemistry "Giacomo Ciamician" of Bologna University, allowing me to achieve remarkable results and professionally grow.

I am also thankful to all my precious co-workers of LEME, especially Dr. Francesca De Giorgio, Federico Poli and Antonio Terella for their friendship, as well as to Prof. Marina Mastragostino for the scientific support and reassurance during these years, although her retirement.

I am also grateful to Prof. Fabio Cicoira for the 4 months-internship at the Polytechnic of Montréal (CA) and for the pleasure of the useful scientific inputs, as well as to Prof. Karl-Heinz Pettinger for have visited the Hochschule Landshut (D) and the Technology Center Energy (TZE) of Ruhstorf ad Rott (D).

I would like to sincerely thank Prof. Stefano Passerini and Dr. Dominic Bresser for have given me the great chance to spend unforgettable six months at the Helmholtz Institute Ulm (HIU, Ulm - Germany), and Dr. Alberto Varzi, Dr. Arianna Moretti, Dr. Sangsik Jeong and Dr. Guk-Tae Kim for their helpful discussions.

I would also thank Prof. Holger Saage (Hochschule Landshut), Dr. Maria Roberta Randi (University of Bologna), Dr. Davide Fabris (Horiba), Dr. Andrea Fiorani (University of Bologna), Dr. Micaela Pasquini (University of

Bologna), Prof. Ferruccio Doghieri (University of Bologna), Dr. Matteo Minelli (University of Bologna), Stefano Degli Esposti (Centro Ceramico Bologna) , Elisa Rambaldi (Centro Ceramico Bologna), Dr. Damiano Genovese (University of Bologna), and Prof. Luca Prodi (University of Bologna) for CT, TEM, micro Raman, rheological measurements and optical fluorescence microscope investigation.

A special thank goes to Prof. Stefania Rapino (University of Bologna) for the SECM measurements and the numerous and more than fruitful scientific discussions.

I kindly acknowledge the financial support provided by the Italian National Agency for New Technologies, Energy and Sustainable Economic Development (ENEA) and the Italian Ministry of Economic Development (MSE), the MIUR-DAAD Joint Mobility Programme for the period at the Hochschule Landshut (D) and at the Technology Center Energy (TZE) of Ruhstorf ad Rott (D), "Le Fonds de recherche du Québec – Nature et technologies (FRQNT)" that founded the four-month internship at the Polytechnic of Montréal and the Karlsruhe Institute of Technology (KIT) for the scholarship of my six-month internship at HIU.

I am also grateful to all my previous colleagues of my master thesis in Sapienza University of Rome that became my close friends, motivating me a lot even during the PhD in Bologna: Dr. Giuseppe Antonio Elia, Dr. Ivana Hasa, Dr. Carmen Cavallo, Giovanna Maresca, Dr. Ulderico Ulissi and Dr. Daniele Di Lecce, as well as to Prof. Jusef Hassoun and Dr. Marco Agostini who enthusiastically guided me in that time.

Last but not least, I would also thank my precious family, without whom I certainly could not have succeeded in getting this great achievement.

Abstract

Efforts are being globally spent today to boost stored energy produced by renewable sources and to encourage a sustainable electric transportation. High-energy conversion systems like batteries can satisfy these demands in an efficient way. Although Li-ion batteries (LIBs) are the best batteries on the market in terms of energy content, a drastic change is desirable to increase both energy and power performance. In this context, Li/O_2 is the next generation system due to the theoretical 10-fold higher specific energy than commercial LIBs (3500 vs. 250 Wh kg^{-1}).

The aim of this PhD thesis is the development of novel concepts and cell designs with the purpose to increase the performance of the aprotic Li and Li/O_2 batteries.

Specifically, a novel design of electrolyte (i.e. solvent-in-salt "SIS" solutions, where the salt-to-solvent ratio is higher than 1), and an innovative concept of semi-solid lithium redox flow air (O_2) battery (SLRFAB) technology, based on the use of a O_2-saturated semi-solid catholyte, have been proposed.

Chapter 1 reports the state of art in the fields of Li, redox flow and Li/O_2 batteries operating in organic electrolytes.

In Chapter 2 are reported the chemicals as well as the preparation of the electrolytes, protective layers, catholytes and electrodes, the description of the instruments used for the chemical-physical and the electrochemical characterizations, and the battery configurations.

Chapter 3 compares the use of a conventional low-concentrated solution with the superconcentrated SISs as electrolytes in Li/O_2 battery.

Indeed, the chemical physics characterizations of the electrolyte (Paragraph 3.1), as well as the voltammetric study of the ORR (Paragraph 3.2) and the galvanostatic test in Li/O_2 battery (Paragraph 3.3) are reported.

In Chapter 4 are presented the results obtained by the scanning electrochemical microscopy (SECM) technique, as well as by the electrolyte-gated transistor, the latter carried out during the internship at the Polytechnic of Montréal. Both techniques were used as analytical tool to investigate in situ the ORR products in different electrolyte media for Li/O_2 battery.

In Chapter 5, the explorative study carried out during the internship at the Helmholtz Institute of Ulm of solid Poly-Ionic-Liquids (PILs) as binder in the Li/O_2 cathode (Paragraph 5.2) and as protective layer with graphene oxide on the Li metal (Paragraph 5.3) is discussed.

Chapter 6 deals about the demonstration of the SLRFAB technology by two different electrochemical tests: the first in an electrochemical glass cell, where the catholyte was stirred to simulate the flowing condition (Paragraph 6.1.1), and the second in a lab-scale prototype where the catholyte constantly flowed (Paragraph 6.1.2). The concept was demonstrated by adding of 2% wt. of Super-P to 0.5 m lithium bis(trifluoromethanesulfonyl)imide (LiTFSI) - tetraethylene glycol dimethyl ether (TEGDME).

Chapter 7 reports some strategies to increase both the specific energy and the energy density, as well the power values of the SLRFAB. The projections of the SLRFAB performance consider the Li/catholyte mass ratio, Li and current collector thickness and the increasing of the carbon content in the catholyte (% wt. carbon).

Chapter 8 deals with the comparison of different formulations of carbon-based catholytes (2% wt. of Super-P or Pureblack and 10% wt. of Pureblack added to 0.5 m LiTFSI - TEGDME) in SLRFAB. The study is focused on how the electrochemical performances are affected by electronic conductivity, morphology and rheological properties of the slurries used as liquid electrode.

In conclusion, the Li^+ concentration in the electrolyte drives the ORR products stability and formation mechanism in a Li/O_2 battery. SIS-based electrolytes can be strategic candidates for Li/O_2 batteries because can favour better cycling performance. Additionally, for the first time a Li/O_2 battery with a catholyte containing conductive carbon in the electrolyte has been proposed (SLRFAB).

The energy content of the SLRFAB is dramatically increased respect to the conventional air-breathing Li/O_2 battery. The passivation of the cathode, indeed, is limited using the catholyte, which is the phase mainly involved during the electrochemical redox reaction. Considering that high carbon content slurries, i.e. high-energy content catholytes, are usable in SLRFAB by selecting the suitable carbon type, a proper formulation of the catholyte ameliorate the results, as the case of 10% wt. of Pureblack added to 0.5 m LiTFSI in TEGDME.

Chapter 1. Introduction

1.1 General Overview

Nowadays the global need to develop novel strategies that improve the quality of renewable energy and the efficiency of related power plants is emerging. The electrical energy storage is feasible in several ways and with different energy storage systems (ESS): i) mechanical (pumped hydroelectric, compressed air, flywheel), ii) thermal (solar ponds), iii) electrical including electrostatic (capacitor and supercapacitors) and superconducting magnetic and iv) chemical, including electrochemical (rechargeable batteries) ESS (1).

Each of these storage systems has its own characteristic in terms of stored energy , cost, duration and maintenance. However, the pumped hydroelectric and the compressed air ESS are well established, the former being the most widely implemented large-scale one (up to 1000 MW).

On the other hand, rechargeable batteries are perhaps the most versatile systems. They can be built and assembled in different sizes thanks to their high modularity. For this reason, they have reached in the last few years wider and wider application, for instance in the home photovoltaic (PV) systems. A rechargeable (or secondary) battery can in fact store the energy during its charge (by PV) and can deliver it during its discharge.

The great advantage lies on rendering energy thus usable in a specific and desired time, without being affected by any climate conditions or availability. The battery also buffers all the fluctuation of the energy

production related to the discontinuities/intermittency of renewable sources. This is of paramount importance to guarantee high-energy quality, especially in the electric grids (2), (3).

The battery versatility is also being exploited in the transport field, where in order to make e-mobility globally practiced, solid investments are required. Large driving autonomy, fast recharge and widespread diffusion of recharge stations are key factors that alleviate the anxiety of the users and can thus finally promote the e-mobility penetration into the market (4) (5).

Among the different battery technologies, LIBs are the system of choice in portable devices and electric vehicles (EVs).

The higher cell voltage and lower weight of LIBs with respect to other systems like lead-acid and nickel–metal hydride (Ni-MH) batteries brings about the highest commercially available specific energy of 248 Wh kg^{-1} in the Tesla "Model S" EV (6).

This EV exhibits a driving autonomy of 540 km at the limited velocity of 50 km h^{-1}. However, this performance, combined to the high cost, does not satisfy the needs of the global community (7).

Thus, the increasing demand of low-cost stored energy, with the purpose of effectively changing the human habits, has collected research efforts towards the development of new battery chemistries. These are the high-energy systems often called "superbatteries" (8).

Figure 1.1.1a compares the theoretical and practical specific energy of LIBs to those of Li/O_2 and Li/S, which are systems that have Li metal as anode, and S or gaseous O_2, respectively, as cathodic active species (9).

Figure 1.1.1b reports instead the practical specific energy (Wh kg^{-1}) and energy density (Wh L^{-1}) of the above cited chemistries, compared to gasoline ones (10).

Li/S and Li/O_2 batteries have a theoretical specific energy of 2600 Wh kg^{-1} and 3500 Wh kg^{-1}, respectively (9). However, these two systems suffer from poor cyclability that has hinder their commercialization although they are being studied since decades.

Li/S battery is limited by dissolution of the lithium polysulphides, i.e. the discharge products, and their shuttle across the electrolyte, with related energy losses.

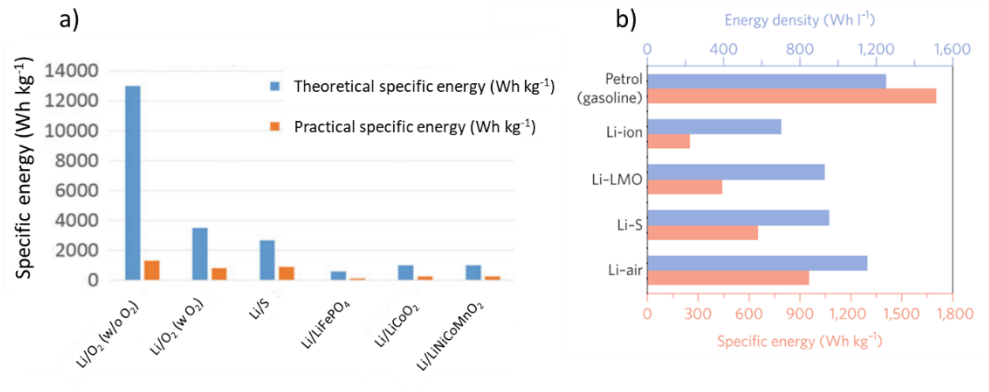

Figure 1.1.1. a) Theoretical (blue) and practical (orange) specific energy (Wh kg^{-1}) of LIBs, Li/S, Li/O_2; b) Practical specific energy (orange) and energy density (blue) of gasoline and state-of-the-art Li-ion, Li /$LiMn_2O_4$ (LMO), Li/S and Li/ O_2 batteries. Reprinted and adapted from ref. (9) and (10), with permission from Springer, Copyright 2017.

On the other hand, Li/O_2 battery suffers from cathode passivation by discharge product, i.e. lithium peroxide (Li_2O_2), and by chemical instability

of electrolyte and positive electrode towards lithium superoxide (LiO_2), which is the intermediate species.

Li/S, which has been firstly planned by Mallory P. R. & Co in 1968 (11) and demonstrated by Rauh et al. in 1979 (12), has recently reached impressive results and seems to be closed to commercialization.

Some companies like PolyPlus and Sion Power Corporation are indeed interested in the system (13). In addition, OXIS Energy is developing a Li/S with 500 Wh kg^{-1} (14), while Sony Corp. is aiming to commercialize Li/S battery in the near future.

Although being firstly introduced in 1976 and then proposed again by Abraham et al. in 1996 (15), Li/O_2 system is still considered in its infancy. However, it is studied by companies like PolyPlus, which aim to protect Li electrodes with a conductive glass-based membrane (16). Interestingly, the protection makes the Li stable in both organic and aqueous electrolytes.

1.2 Lithium metal batteries

Because both Li/S and Li/O_2 systems have Li metal as anode material, a general introduction on the Li battery can better address the topic.

The great advantage of the use of Li derives from the molar weight of 6.941 g mol^{-1} and the density of 0.535 g cm^{-3}. The specific capacity of 3860 mAh g^{-1}, combined to the standard redox potential of the Li/Li^+ couple of -3.04 V vs. SHE, renders the Li electrode a surpassing candidate for high energy batteries.

G.N. Lewis first studied Li batteries in 1912, but only in 1958 it was found that the Li could be successfully electroplated in aprotic solvents (17), (18), (19).

From this achievement, starting from the 1960s, the use of Li anode bought about a novel class of electrochemical energy storage systems in the market with incomparable characteristics. These were primary batteries, i.e. not rechargeable, working up to 3 V, a voltage much higher than that of the conventional system based on aqueous electrolyte with the intrinsic limit of 1.23 V. However, production of rechargeable batteries based on Li, is much more problematic and some concerns need to be considered.

As all the alkali metals, Li forms a passivation layer on its surface conventionally called solid electrolyte interphase (SEI) as it comes in contact with the electrolyte (Figure 1.2.1) (20) (21).

This interphase acts like a solid electrolyte, i.e. being both electron insulating and ion conducting and, if not stable, usually is destroyed each time that the battery completes one single cycle of discharge and charge.

The SEI presence is considered to be fundamental for safe battery operation because without any passivation layer the metal quickly dissolves or becomes corroded, affecting the battery performance (21), (22).

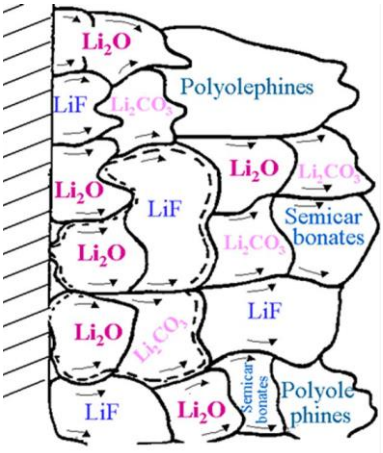

Figure 1.2.1. Scheme of the chemical composition of the SEI on Li, according the mosaic model. Reprinted and adapted from ref. (21), with permission from Electrochemical Society. Copyright 2017.

Furthermore, apart from being affected by the imposed kinetics conditions, i.e. the applied current to the battery, the SEI features depend on the structure, morphology and chemical composition of the anode and on the electrolyte (23).

Another issue is that Li metal suffers from dendrite formation during its plating, i.e. an uneven deposition occurs during the electrochemical Li reduction, as reported in Figure 1.2.2 (10).

As described in the figure, the Li plating causes the volume expansion, which destroys the SEI interphase. A further plating causes then the dendrites to growth through the cracks, at an extent that depends on the set currents.

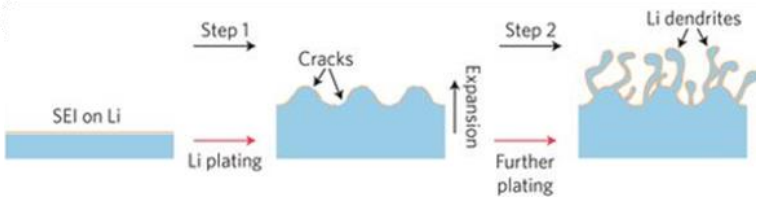

Figure 1.2.2. Schematic representation of the Li dendrite nucleation during the Li plating. Reprinted and adapted from ref. (10), with permission from Springer.

The dendrites then grow towards the cathode side, increasing the surface area of the anode, and short-circuit the cell, i.e. the negative and positive electrodes are in direct contact with negligible resistance. The short-circuit can be so catastrophic to overheat the system if it cannot dissipate the generated heat, and catch a fire or explosion (24)

Several efforts have been spent to understand the reason of a bad deposition of Li during the charge of a Li battery and to find some strategies to obtain homogeneous deposition at the working currents (25), (26).

Electrolyte additives able to create a selective inorganic/organic protective layer on Li, or the use of novel electrolytes, like ionic liquids (IL) and superconcentrated solutions, have been proposed to stabilize the surface with a tailored SEI. Solvent-in-salt solutions, i.e. solution with equal molar amount of salt and solvent, have positive impact on the cathode in Li/S and Li/O_2 batteries and seem to act in a synergic way also on the SEI formation by preventing dendrites even at very high current density (27), (28). Furthermore, the novel class of Poly-Ionic-Liquids (PILs) are being studied as innovative solid polymer electrolyte and can be a strategy for a safe working operation of the Li batteries (29), (30), (31), (32), (33).

1.3 Li/O_2 Battery

The metal/air battery discharge lies on the electrochemical reduction of O_2, which comes from the atmosphere or is stored in a separated reservoir, at a high surface area cathode. Meanwhile, the metallic anode is oxidized. The opposite process occurs during the charge of the metal/air battery.

Figure 1.3.1 compares the theoretical specific energy (mWh g^{-1}), i.e. the product of the cell capacity (mAh g^{-1}) and voltage (V), of different metal/air chemistries. In order to avoid any contamination by water vapor and CO_2, the tests in lab-scale are often performed using O_2 and not direct air. In this case, it is better to define the chemistry as Li/O_2 (34).

As already reported in 1.2, among the different metals, Li has the highest gravimetric specific capacity and the lowest density. These features, coupled to the lowest first ionization energy of 520 kJ mol^{-1} (amount of energy required to remove the external valence electron and generate Li^+) renders the Li/O_2 chemistry very attracting.

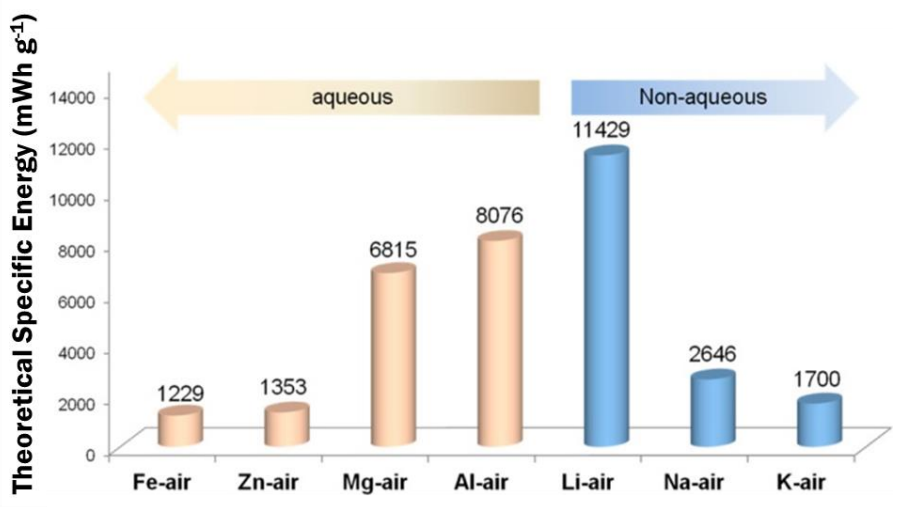

Figure 1.3.1. Theoretical specific energy of different metal/air batteries; (weight of the gas is not considered). Reprinted and adapted from ref. (34), with permission from American Chemical Society, Copyright 2017.

The first Li/O_2 battery has been proposed in the second half of seventies (35). This type of battery worked with an aqueous electrolyte but, because of safety issues regarding the high reactivity of Li with water, the project was quickly abandoned.

As already above reported, a renewed interest in the Li/O_2 topic came in 1996 from Abraham and coworkers (15). They proposed the first rechargeable battery with a non-aqueous electrolyte based on a gel polymer membrane, reaching a specific energy of ca. 250-300 Wh kg^{-1}. Then, in 2006, Bruce et al. studied a carbonate-based Li/O_2 battery with manganese dioxide, which operated as electrocatalyst in the cathode electrode. The cycling performance were improved and the Li_2O_2 decomposition to O_2 was interestingly proven during the charge operation (36).

Different kind of Li/O_2 battery have been reported in several papers and are classified in four types, which are aprotic, aqueous, hybrid and solid Li/O_2 battery.

The use of aqueous alkaline solutions electrolytes not only decrease the operating battery voltage to 1.23 V, but it forces the use of solid membrane separators or protective layers in order to prevent any safety issues. On the other hand, these additional layers usually do not ensure a fast battery response, thus dramatically decreasing the power output.

Among the different type, the aprotic Li/O_2 is considered to be the most feasible because, as already indicated, Li anode is stable in organic, while additional layers on the Li interface may affect the battery rate response.

Figure 1.3.2 reports the aprotic Li/O_2 battery operation, which includes a porous cathode electrode, a non-aqueous electrolyte and Li as anode (37).

The positive electrode material should feature low density, high electric conductivity, have porous structure and high surface area. In order to store the largest amount of discharge products and to favor a fast O_2 diffusion, these characteristics are indeed crucial.

In aprotic Li/O_2 batteries, the discharge species is the lithium peroxide (Li_2O_2) that is deposited on the carbon surface and during the battery charge is oxidized to get O_2 again, with the Li reduction.

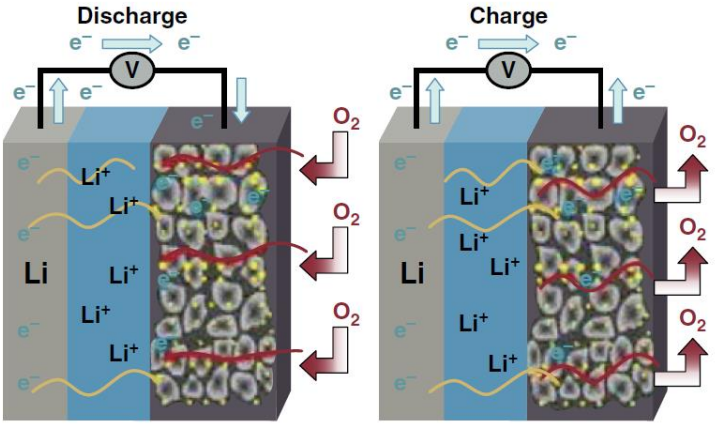

Figure 1.3.2. Scheme of the aprotic Li/O_2 battery configuration. Reprinted from ref. (37), with permission from John Wiley and Sons, Copyright 2013.

Electrolyte features affect the performance of the Li/O_2 battery. The first investigated aprotic electrolyte was based on carbonates, but then some papers demonstrated the instability against the ORR products during the battery operation (36), (38). Recently, many common solvents like acetonitrile (ACN), dimethylsulfoxide (DMSO), glymes, polymer-based electrolyte, as poly(ethylene) oxide (PEO), and ionic liquids (ILs) are being investigated showing better stability than carbonates (39).

1.4 ORR in aprotic Li/O_2 battery

Equation 1 can generally describe the oxygen redox reaction (ORR) in non-aqueous Li/O_2 battery:

$$2Li + O_2 \rightarrow Li_2O_2 \quad (1)$$

The process was firstly explained by Abraham et al. that demonstrated the O_2 reduction to lithium peroxide (Li_2O_2), according a bi-electronic process that occurs by several steps (15).

The first reduction affects the O_2 species to get superoxide ion ($O_2^{\bullet-}$), according to Equation 2:

$$O_2 + e^- \rightarrow O_2^{\bullet-} \quad (2)$$

In presence of Li^+ cations, lithium superoxide (LiO_2) is formed and then evolves in lithium peroxide (Li_2O_2) via both chemical disproportion and/or electrochemical process, according to Equations 3, 4 and 5.

$$O_2 + Li^+ + e^- \rightarrow LiO_2 \qquad (E_0 = 3.0 \text{ V vs. } Li^+/Li) \quad (3)$$

$$2LiO_2 \rightarrow Li_2O_2 + O_2 \qquad \text{(chemical disproportion)} \quad (4)$$

$$LiO_2 + Li^+ + e^- \rightarrow Li_2O_2 \ (E_0 = 2.96 \text{ V vs. } Li^+/Li) \quad (5)$$

Superoxide species are highly reactive and cause electrolyte, carbon and binder degradation of the cathode, while insoluble Li_2O_2 clogs the cathode surface during battery discharge, limiting the capacity and bringing about high recharge overpotentials (> 1 V). These are the main drawbacks of the system, which have hindered the commercialization and still need to be fully addressed (40), (41), (42), (43).

Specifically, the electrolyte in Li/O_2 batteries must be resistant to $O_2^{\bullet-}$ that can nucleophilically attack the solvent molecules, must display good oxidative resistance, combined to a high O_2 solubility and mass transport.

ORR reversibility depends on the electrolyte choice and on the kind of ions in the solution. In 2010 Laoire et al. applied the Hard Soft Acid Base (HSAB) theory to interpret the ORR in Li/O_2 battery (44). The HSAB theory was first proposed by Pearson to explain the stability of compounds and the reaction mechanisms. Chemical species, including ions, having Lewis acidity or Lewis basicity properties are classified as hard or soft. Hard characteristics are short atomic/ionic radius, high charge density, and high polarizability while soft ones are long atomic/ionic radius, low charge density and low polarizability (45).

The HSAB theory states that soft acids react faster and form stronger bonds with soft bases, whereas hard acids react faster and form stronger bonds with hard bases. On this theory, the typical behavior of Li^+ cation, an hard Lewis acid, that has an better affinity with the hard Lewis base O_2^{-2} (peroxide ion) with $O_2^{\bullet-}$ (superoxide ion), which is a soft Lewis base can be explained.

LiO_2 is thus not stable enough and tends to make disproportion to Li_2O_2 and O_2 in electrolyte containing Li^+, according Equation 4. This process causes the passivation of the positive electrode because of the insulating nature of Li_2O_2 and renders the battery charge (electrochemical oxidation of Li_2O_2 discharge product) only feasible at higher potentials, where the electrolyte and carbon cathode are not usually stable. This determines the electrochemical irreversibility of the process.

It has also been proposed that the solvation action that the organic solvent practices on Li^+ cations plays a key role in the ORR process mechanism.

Laoire et al. found that a good solvating agent for Li^+ might have a high donor number (DN), which is the measure of the solvent basicity, in other words the ability to use a free electron pair to solvate, as firstly proposed by Gutmann. Thus, to soften the acidity of Li^+, organic solvents with hard base properties are used (46).

McCloskey et al. also underlined the influence of the chosen salt and solvent in the electrolyte. The electrolyte should be carefully selected in order to promote the Li_2O_2 formation in solution rather than on the electrode (solution formation mechanism vs. the surface growth (Figure 1.4.1) (47).

Indeed, the formation in solution of Li_2O_2 discharge product and then its precipitation as large clusters on the cathode surface allows part of the electrode to be free from passivation. This enables high discharge capacities. On the contrary, when the surface growth mechanism occurs the passivating film on the electrode surface only accelerates the cell death.

Consequently, the stability in solution of the intermediate ORR species LiO_2 depends on the Li^+ Lewis acidity that affects the mechanisms of Li_2O_2 formation and thus, the cycling performance.

High-DN solvents and soft Lewis acid cations promote the solution mechanism stabilizing the $O_2^{\bullet-}$ (soft Lewis base). Low-DN solvents and hard Lewis acid cations, like free Li^+ ions, facilitate the surface mechanism and LiO_2 disproportionation to Li_2O_2 (hard Lewis base).

The interpretation of the insulating Li_2O_2 production is fundamental. While the mechanism of the oxidation of solid Li_2O_2 on conductive carbon electrode is still under investigation, it has been found that nature and morphology of Li_2O_2 affect the overpotential of the recharge step in a Li/O_2 battery (48).

While large crystalline toroids lead a higher recharge overpotential than a slightly amorphous layer, the latter causes lower efficiency of the battery cycling (49), (50).

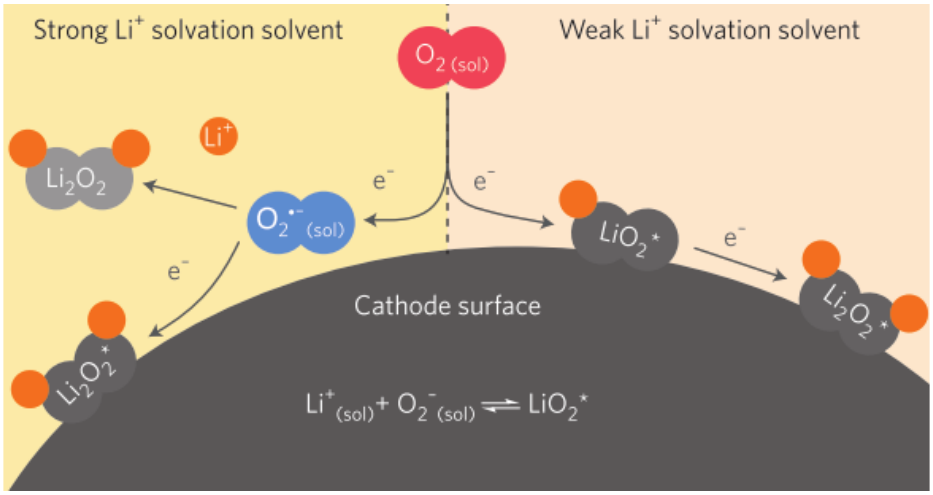

Figure 1.4.1. Li_2O_2 formation mechanism, depending on the solvation of Li^+ cation. Reprinted from ref. (47), with permission from Springer.

1.5 Unconventional electrolytes in Li/O_2 battery

Solvent-in-salt (SIS) solutions with molecular salt/solvent ratio higher than 1 have been proposed as key electrolytes for Li batteries, including the Li/O_2 system (51).

Generally, the chosen organic solvent for SIS belongs to the category of glymes, i.e. ethers with oxygen atom alternated to the ethylene group in the repeat unit. There are different kind of glyme with specific features, depending on the ether chain length.

The common characteristic is the coordination of Li^+ cation by the lone pair of the oxygen atoms, which is similar to that occurring in ion-conducting polymer like PEO.

As already reported in Paragraph 1.4, $O_2^{\bullet-}$ can act as a very strong Lewis base and consequently induce an autoxidation of the organic solvent, according to the Equation 6:

$$O_2^{\cdot-} + H - A \leftrightarrows H - O_2^{\cdot} + A^- \qquad (6)$$

Thus, the Lewis acidity of aliphatic C-H bond in HA, expressed by the acid dissociation constant Ka, is a very important feature that dramatically affects the solvent stability towards the H-extraction by $O_2^{\bullet-}$ (53). Specifically, a low pKa value of the solvent reflects the acidity of the H in C-H, thus determining the instability to the strong base $O_2^{\bullet-}$. Furthermore, in 2013, Khetan et al. suggested also that the highest occupied molecular orbital (HOMO) level of the solvent could be an indicator for the oxidative stability in Li/O_2 battery. They concluded that more the HOMO energy level is low, more the solvent is stable and that the ideal solvent of the electrolyte must thus have a high pKa, combined to a low HOMO (52).

Although generally featuring low DN values, glymes have a low HOMO and high pKa compared to DMSO and carbonate and are thus good candidates for Li/O_2 batteries.

The main feature of SIS based on glymes and lithium bis(trifluoromethanesulfonyl)imide (LiTFSI) is the IL-like structure with free $[Li(glyme)_1]^+$ big cation complexes and $TFSI^-$ anions. Each molecule of

solvent, in fact, coordinates one Li^+ cation in SIS based on LiTFSI and (tetraethylene glycol dimethyl ether) TEGDME.

However, SIS features are affected also by the counter anion. In SIS based on lithium nitrate ($LiNO_3$) and TEGDME, NO_3^- ion coordinates Li^+ more strongly because its higher basicity than the glyme molecule, leaving a remarkable amount of TEGDME molecule totally free. For this reason, the authors classified the SIS based on TEGDME and salts like $LiNO_3$ as poor solvate ILs (54).

It has been found that SIS based on LiTFSI and diglyme, even though featuring higher viscosity than electrolytes with conventional salt concentration, can improve the interface of the cathode in Li-ion batteries (lithium cobalt dioxide, $LiCoO_2$) and can lead to a longer cycling stability (55).

Concerning the Li/O_2 battery application, for the first time Li and co-workers showed that Li/O_2 cycling performance in tetra and triglyme-LiTFSI based electrolytes depends on the salt concentration (56). Furthermore, Kwon et al. have recently demonstrated that the SIS based on equimolar solution of triglyme and LiTFSI, namely $[Li(triglyme)_1]TFSI$, has a larger anodic stability in linear scan voltammetry, compared to $[Li(triglyme)_4]TFSI$, with a solvent-to-salt ratio of 4. The different amount of Li salt affects also the morphology of Li_2O_2, depending on the stability of $O_2^{\bullet-}$, as already mentioned. The use of SIS implies a relative lack of side reactions and this can be attributed to the decreasing of the glyme HOMO level by the complexation with Li^+ cation that reflects on the better stability towards the $O_2^{\bullet-}$ attack (57).

Additionally, increasing the concentration of electrolytes is a multi-effective strategy for high energy batteries that employ Li metal as anode. SIS in fact are also being attracting in Li metal batteries because they can stabilize the Li/electrolyte interface, as already introduced in Paragraph 1.2. Superconcentrated electrolytes with a low anion transference number (fraction of the total current carried by the only anions), which indicates its hindered transport, can minimize the polarization and the electric field, delaying the dendrite formation at the metal surface.

The Li^+ transference number (t_{Li+}) is the fraction of the total current carried by the only Li^+ cations in the selected electrolyte. The value of t_{Li+} can be very high in SIS, as suggested by Prof. Armand and Chen in 2013, which developed a LiTFSI in 1,3-dioxolane/1,2-dimethoxyethane (DOL/DME) electrolyte with a t_{Li+} of 0.73 (28). The amount of free and mobile anions is thus greatly reduced due to the coordination with Li^+ and the molecules of solvent to form the large $Li^+\cdots$glyme$\cdots$anion complex. During the deposition of Li^+ on the Li metal, the free space created by the anion depletion is minimized, inhibiting the irregular dendrite nucleation (10), (25).

The decreased number of free molecules of solvent in SIS suppresses also the incessant parasitic reaction between the electrolyte and the anode, with a positive effect on the SEI stability.

A novel class of solid electrolyte for Li batteries is that of Poly-Ionic-Liquids..

Their repeating unit could be cations, like imidazolium or pyrrolidonium and anions, like (bis(fluorosulfonyl)imide or bis(trifluoromethanesulfonyl)imide) of ILs. They preserve some properties of ILs, for instance the ionic

conductivity, the electrochemical, chemical and thermal stability, but also feature the good mechanical properties of a polymer. Besides being proposed as electrolyte, another interesting application of PILs has been their use in LIBs as binder for electrodes like $LiFePO_4$ and $Li_4Ti_5O_{12}$ (58), (59), (60), (61). Furthermore, another possible application of PILs could be in Li/O_2 batteries, even if no related papers have been published yet.

1.6 Scanning electrochemical microscopy as a powerful tool in battery field

Scanning electrochemical microscopy (SECM) is a scanning probe microscopy technique (SPM). It involves measurements of current obtained from a ultramicroelectrode (UME) used as working electrode (WE), which has an active diameter between few nanometers up to 25 μm. The currents are obtained when the UME is held in a solution close to a substrate. From the variation in the electrochemical response of the tip (UME), one can obtain information about the properties and nature of the substrate.

SECM is being considered a powerful analytical technique since it also provides spatially and resolved information on the substrate (62). Indeed, it was used to address several issues of LIB, semi-solid flow and Li/O_2 battery field, and when coupled to a surface morphology characterization, like optical and atomic force microscopy, it can reveal important feature that are difficult to get.

Gunasekara et al. demonstrated in 2014 that the UME can be used to select and optimize the properties of electrolytes in non-aqueous $Li\text{-}O_2$ batteries (63). Wittstock et al. have studied the O_2 permeation through gas diffusion

electrode (GDE) of different thickness and its flux from the working substrate electrode to the 1M $LiClO_4$ in DMSO electrolyte (64). An oxidation pulsed procedure was also interestingly proposed to clean up the Pt working electrode (WE) probe from Li_2O_2. The $O_2^{\bullet-}$ intermediate species was then detected by fluorescence microscopy and by local detection at defined distances from the GDE working substrate electrode.

1.7 Redox flow batteries

Redox flow batteries (RFBs), like vanadium-flow batteries, with dissolved electro-active species, are attracting much attention for stationary plants where limited battery encumbrance is not mandatory.

RFB lies on two liquid electrolytes with soluble redox couples, called anolyte and catholyte that flow through separate compartments where the redox process occurs, as shown in Figure 1.7.1 (65).

Redox-flow batteries (RFB) are being considered attractive due to their main feature that is the decoupling of energy and power.

Energy depends on electroactive species quantity/concentration and on the volume of the tank. However, the energy of vanadium RFB, which are among the most used RFB, suffers of the low solubility of the electroactive species in the electrolyte, limiting the concentration to be less than 8M (66). Power depends instead on the electrode areas of the electrode plates and on the flow rate.

Being characterized by a low cell voltage (1.27 V for the vanadium RFB) and low specific energy (ca. 25 Wh kg^{-1} for the vanadium RFB), RFBs are

excluded from the application in the electric vehicle and portable device fields.

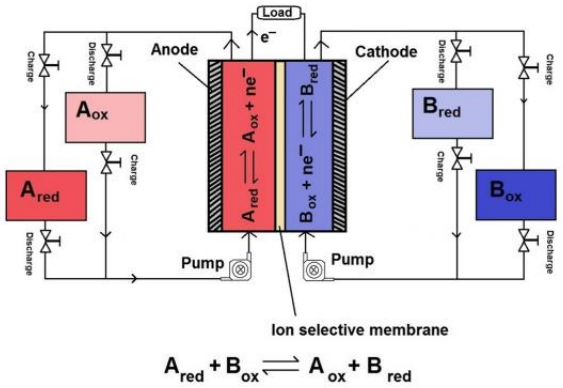

Figure 1.7.1. Scheme of redox-flow battery (RFB). Reprinted from ref. (65), with permission from Springer.

Much research efforts have been devoted to increase energy and power of RFBs. The main strategies have been the use of a) light metals as anode, b) organic electrolyte to broaden the electrolyte electrochemical window and thus the energy of RFBs, c) O_2, which is fed in the electrolyte, acting as cathode active material, and d) semi-solid anolyte and/or catholyte to increase the electrode surface and thus the energy (67), (68), (69), (70), (71), (72), (73), (74), (75), (76).

1.8 Li-redox flow air battery

The strategy to use a metal anode, like Zn or Li, has been actively proposed in RFBs field. While Zn in RFBs is already used and the Zn-bromide flow

batteries are commercially available, the use of Li, instead of a flowing anolyte, is a relatively new approach. Goodenough and Zhou used first this light metal in flow batteries, opening the research towards the integration of Li batteries and RFBs. This approach brought to a novel configuration of Li/O_2 battery, i.e. the Li Redox Flow Air (O_2) Battery (LRFAB) (77), (78), (79).

The use of O_2-catholyte in LRFBs is a valuable strategy to develop batteries that outperform both RFBs and conventional (not-flowing) Li/O_2 batteries.

The use of a catholyte, which is saturated by O_2, makes the cell capacity less affected by its volume. The energy indeed depends directly only on the O_2 (being the active species) solubility that is related to the chosen media.

The same O_2 concentration can be obtained in an electrolyte that helps the O_2 dissolution and features a lower volume, which brings about a positive effect on the dimension and weight reduction of the battery (80).

An organic LRFAB was reported with an IL electrolyte. The discharge capacity was 600 mAh g^{-1}, by considering the carbon electrode weight. The cell was cycled with a current density of 0.2 mA cm^{-2} and recharged, giving an efficiency of 92%. The cell design of this LRFAB is reported in Figure 1.8.1 (77). Carbon ZL was deposited on the carbon paper (CP) to increase the performance.

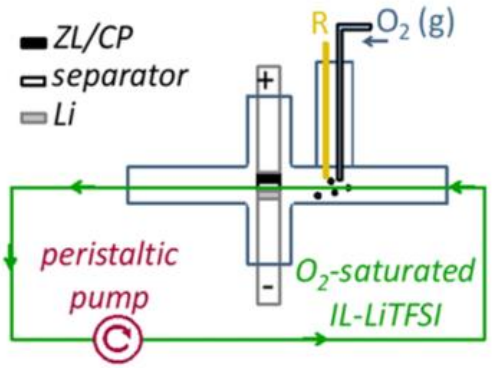

Figure 1.8.1. Scheme of the Li Redox Flow Air (O_2) Battery (LRFAB) based on IL. Reprinted from ref. (77), with permission from American Chemical Society. Copyright 2013.

The LRFAB concept was also exploited by adding soluble redox mediators to the electrolyte (ethyl viologen and iodide), which can catalyse the O_2 reduction and evolution, as already proposed by Prof. Owen and coworkers (81).

The cell comprised a Li anode, which was separated from a carbon felt cathode by a membrane, and by a separated gas diffusion tank connected to the cathodic compartment by a pump, as reported in Figure 1.8.2 (79).

The electrolyte was LiTFSI–TEGDME with the redox catalysts dissolved. During the O_2 reduction, the Li_2O_2 discharge product was deposited on the porous matrix located in the tank, preventing the cathode passivation.

The highest discharge capacity featured by this system was 11 mAh cm^{-2} (respect the carbon felt surface) at 0.125 mA cm^{-2}.

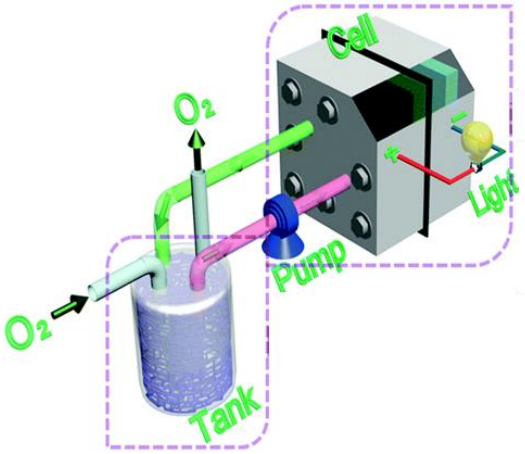

Figure 1.8.2. Scheme of the Li Redox Flow Air (O_2) Battery (LRFAB) based on LiTFSI in TEGDME and ethyl viologen and iodide as redox catalysts. Reprinted with permission from the Royal Society of Chemistry from ref. (79).

1.9 Semi-solid flow battery

The need to decrease the inactive components in a battery and to decouple energy from power has focused notable efforts to the development of semi-solid liquid electrodes. Solid and electroactive particles are dispersed in the electrolyte, maximizing the available space for the redox reaction. However, the development of semi-solid RFBs implies an efficient management of these viscous slurries.

The first semi-solid anolyte based on Zn particles and circulated in the Zn/air battery was proposed by the Compagnie Générale d'Electricité in the 70s' (82). Furthermore, semi-solid slurries based on LIB conventional materials, like $LiFePO_4$, $LiCoO_2$, Si and $Li_4Ti_5O_{12}$, were investigated, demonstrating how the use of semi-solid electrodes is strategic to dramatically increase

both the power and energy of LIBs (83), (84), (85), (86), (87), (88), (89), (90). The projected specific energy and energy density of $Li/LiCoO_2$ semi-solid batteries were calculated to be 130-250 Wh kg^{-1} and 40–500 Wh L^{-1}, respectively (83).

Not only the LIB materials were studied. Further papers reported the possibility to use semi-solid, fluidic electrodes even in Li/polysulfides and Na-ion batteries, as well as in electrochemical double-layer supercapacitors (91), (92), (93), (94), (95), (96).

LIB-based semi-solid electrodes are considered very attracting because of the enhanced surface and they are recently being exploiting by the 24M startup from Massachusetts Institute of Technology with the aim to commercialize a battery with a capacity 5 times higher than that one of the standard LIBs (97), (98).

Lastly, the semi-solid flow battery technology can solve some issues of e-mobility, considering that a fast charged battery can be obtained by substituting the completely discharged battery catholyte with a fresh one, as suggested by Prof. Y-M. Chiang, chief scientist and co-founder of 24M.

1.10 Aim of the thesis

The aim of this PhD thesis is the development of a novel concept and cell design of the aprotic Li/O_2 system in order to increase the battery performance. Specifically, a new designed electrolyte (solvent-in-salt SIS solutions), and an innovative concept of flow Li/O_2 battery have been proposed. Furthermore, the explorative use of Poly-Ionic-Liquid as binder of Li/O_2 cathode and as protective layer on Li has been explored.

A voltammetric test and a scanning electrochemical microscope analysis have been performed to study the lithium peroxide (Li_2O_2) formation mechanism and how it changes from a surface to a solution process moving from conventional low-concentrated electrolyte to LiTFSI-TEGDME-based SIS solutions.

For the first time a semi-solid Li redox flow O_2 battery (SLRFAB), based on semi-solid carbon catholyte, has been also proposed.

The concept has been demonstrated with low cost, metal-free materials, first in an electrochemical glass cell, where the catholyte was stirred to mimic the flowing condition, and then in a flow semi-solid Li/O_2 cell. Additionally, some projections on the SLRFAB energy and power values have been simulated, with increased carbon content in the catholyte. A study on different catholyte formulations, based on a couple of carbon and different quantity have been also performed. In order to identify the proper catholyte composition suitable for the SLRFAB, the electrochemical results, obtained in an electrochemical glass cell with the stirred catholytes, have been then related to the conductive, morphological and rheological properties of the different catholytes.

Part of the research was also carried out in the frame of the MIUR-DAAD Joint Mobility Programme at the Technology Center Energy (TZE) of Ruhstorf ad Rott and at the Hochschule Landshut (D), under the supervision of Prof. Karl Heinz Pettinger, at the Polytechnic of Montréal (CA), under the supervision of Prof. Fabio Cicoira, supported by "Le Fonds de recherche du Québec – Nature et technologies (FRQNT)" and at the Helmholtz Institute Ulm (HIU) (DE), supported by the Karlsruhe Institute of Technology (KIT) under the supervision of Prof. Stefano Passerini and Dr. Dominic Bresser.

Chapter 2. Experimental Section

Chapter 2 addresses materials and methods used for the study of electrolytes and electrodes for Li/O_2 cell, Li batteries and carbon-based semi-solid catholytes for semi-solid flow Li/O_2 cell.

2.1 Electrolyte, catholyte and electrode preparation

Electrolytes for Li/O_2 cell based the organic solvent tetraethylene glycol dimethyl ether (TEGDME, 99%, Aldrich, 20 ppm of H_2O) and lithium bis(trifluoromethanesulfonyl)imide (LiTFSI, ≥99%, Aldrich) (Figure 2.1.1) have been investigated. Solutions with 5 different molality (m) were prepared with LiTFSI dried under continuous vacuum with the B585 Buchi oven at 120 °C for 24 hours, and stored in dry box (MBraun, O_2 and H_2O < 1 ppm). Table 2.1.1 reports the electrolytes studied with the different molar ratio of both solvent and lithium salt.

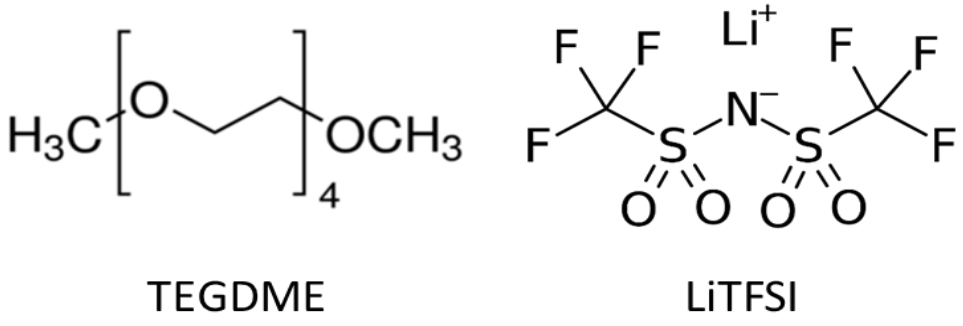

Figure 2.1.1. Structures of tetraethylene glycol dimethyl ether (TEGDME) and lithium bis(trifluoromethanesulfonyl)imide (LiTFSI).

Table 2.1.1. Molality and molar ratios of the investigated solutions.

Electrolyte	0.1m	0.5m	2m	4m	5m
Molality ($mol_{salt}/kg_{solvent}$)	0.1	0.5	2.0	4.0	5.0
Molar ratios (salt to solvent)	1:51	1:9.1	1:2.3	1:1.1	1:0.9

At HIU, the IL N-N-diethyl-N-methyl-N-(2-methoxyethyl)ammonium bis(trifluoromethanesulfonyl)imide (DEMETFSI) (Figure 2.1.2) was synthesised by Dr. Sansik Jeong.

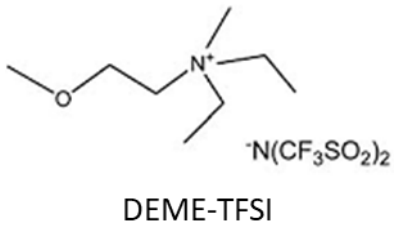

DEME-TFSI

Figure 2.1.2. Structure of the IL N,N-diethyl-N-(2-methoxyethyl)-N-methylammonium bis(trifluoromethanesulfonyl)imide (DEMETFSI).

Then, the high concentrated electrolyte DEMETFSI-based solution was prepared in glove box by mixing LiTFSI with N,N-diethyl-N-(2-methoxyethyl)-N-methylammonium bis(trifluoromethanesulfonyl)imide (DEMETFSI) in a molar ratio 0.5:1.

The not-crosslinked copolymer of 1-ethyl-3-vinylimidazolium-1-decyl-3-vinylimidazolium C_2VImTFSI-C_{10}VImTFSI (1:1 wt.) was provided by Dr. Dominic Bresser and tested in Li/Li and Li/O_2 cells.

The crosslinked imidazolium-based Poly-Ionic-Liquids (PIL) were synthetized in the IL lab available at HIU. The monomers 1-Ethyl-3-vinylimidazolium bis(trifluoromethane)-sulfonimide (C_2Vim-TFSI) (Solvionic) and 1-Ethyl-3-vinylimidazolium bis(fluorosulfonyl)imide (C_2Vim-FSI) (Solvionic) were crosslinked to 1,4-Butanediyl-3,3'-bis-1-vinylimidazolium Di-bis(fluorosulfonyl)imide (C_4(VIm-FSI)$_2$ or Divinylbenzene (DVB) (Merck). The initiators were 2,2′-azobis(iso-butyronitrile) (AIBN) (Fluka) or Benzoyl peroxide (BP) (Fluka). The chemical structures of the monomer C_2Vim-TFSI, the crosslinkers C_4(VIm-FSI)$_2$ and DVB are reported in Figure 2.1.3.

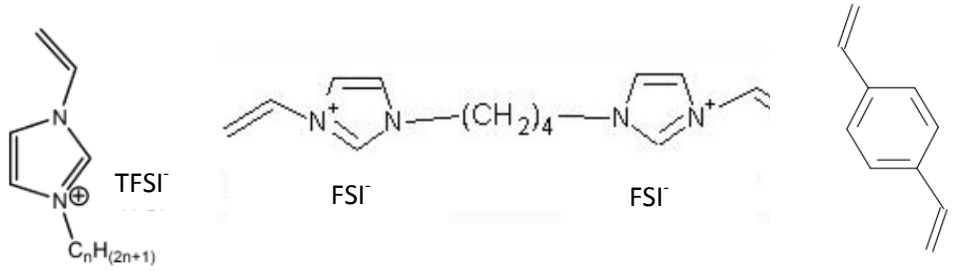

Figure 2.1.3. Structure of the IL 1-Ethyl-3-vinylimidazolium bis(trifluoromethane)-sulfonimide (C_2VIm-TFSI) on the left, the 1,4-Butanediyl-3,3'-bis-1-vinylimidazolium Di-bis(fluorosulfonyl)imide C_4(VIm-FSI)$_2$ in the middle and of the divinylbenzene DVB on the right.

The monomer (C_2VIm-TFSI or C_2VIm-FSI), the crosslinker (C_4(VIm-FSI)$_2$ or DVB, 5 or 10 wt. % of the monomer) and the initiator (AIBN or BP, 3 mol % of the amount of vinyl groups) were dissolved in tetrahydrofuran (THF) in a flask under continuous Ar flow.

The solutions were stirred at room temperature and then kept for 4 h at 70 °C and 2 h at 80 °C. LiTFSI was eventually added to the initial mixture (monomer/LiTFSI = 3:1 mol/mol). All the obtained solids were then stored in dry room.

The crosslinked PILs based on C_2VIm-TFSI or C_2VIm-FSI and the crosslinker C_4(VIm-FSI)$_2$ (5 and 10 wt. % of the monomer) (AIBN initiator) with eventually the adding at the beginning of LiTFSI were not electrochemically tested in cells because they dissolved in the chosen high concentrated electrolyte LiTFSI:DEMETFSI 0.5:1.

The cathode electrodes were prepared by doctor-blade technique (Figure 2.1.4), with 160 μm as thickness, casting a slurry composed by Super-P and PVDF (6020 Solef, Solvay) or the copolymer C_2VImTFSI-C_{10}VImTFSI in 95:5 % weight ratio, dispersed in NMP on a gas diffusion layer (GDL, SGL-35BC carbon paper, SGL). After drying at 120 °C overnight, the GDL were punched in disk having 16 mm as diameter. The electrodes were dried again in order to remove any remaining solvent under high vacuum at 120 °C overnight.

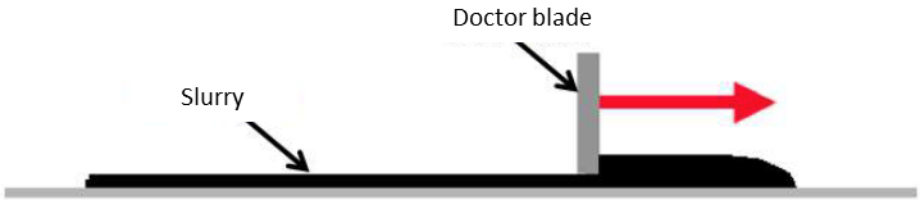

Figure 2.1.4. Schematic representation of the doctor blade technique to prepare the cathode from the slurries.

The Li electrodes with protective layer were prepared in dry room and obtained by casting on the metal 50 µl cm^{-2} of a dispersion of graphene oxide (GO) and the copolymer C_2VImTFSI-C_{10}VimTFSI and the crosslinked PILs based on C_2VIm-TFSI or C_2VIm-FSI and 10% wt. of DVB (BP as initiator) + LiTFSI in N-methyl-2-pyrrolidinone (NMP, Aldrich 99.9 %).

Different compositions have been electrochemically tested and were obtained by dissolving 0.2 mg ml^{-1} of GO and 1 or 2 mg ml^{-1} of copolymer C_2VImTFSI-C_{10}VimTFSI. LiTFSI was eventually added directly to these dispersions ($[Im^+]$:$[Li^+]$ = 1:3 molar ratio).

The other dispersions involved 0.2 mg ml^{-1} of GO and 2 mg ml^{-1} of crosslinked C_2VIm-TFSI or C_2VIm-FSI and 10% wt. of DVB + LiTFSI.

The Li electrodes were dried under vacuum at 60 °C overnight and then transferred in the glove box.

At UNIBO, the catholytes were prepared by adding to the 0.5m electrolyte two different carbon blacks, namely Super-P® (SP, Erachem Comilog N.V., BET 65.5 m^2 g^{-1}) or Pureblack® 315 (PB, Superior Graphite, 64 m^2 g^{-1}). The carbon powders were previously dried overnight at 120 °C under continuous vacuum with the B585 Buchi oven.

The catholytes have been called SP2 and SP5, featuring 2wt.% and 5wt.% of SP, and PB2 and PB10 with 2 and 10wt.% of PB.

Both electrolyte and catholyte were saturated with $O_{2(g)}$ (>99.999%, SIAD).

The current collectors used as working electrode (WE) were carbon paper Spectracarb 2050 (CP, Spectracorp. USA), with thickness 40 mils and reticulated vitreous carbon (RVC, 100 PPI foam ERG Aerospace Corporation, USA), with 3% nominal density and 0.5 cm^{-1} thick. They both were dried at 120 °C overnight under vacuum before use. The CP or RVC current collectors were coated with SP carbon by drop casting. The composition of the SP-based ink was 95% SP – 5% polyvinylidene fluoride (PVDF, Kynar HSV900) in N-methyl pyrrolidone ink (28 mg of SP per mL). After the deposition, the current collectors were heated at 60 C° overnight and labelled CPSP or RVCSP, indicating the carbon deposition on CP or RVC. For CV measurement in the different electrolytes, a glassy carbon (GC, Tokai Carbon Ltd., Japan) was used as working electrode (GC) with 3 mm diameter and 0.07 cm^2 area.

2.2 Equipment for chemical-physical characterizations

The thermogravimetric characterization of the LiTFSI-TEGDME electrolytes was performed with a TA Instruments Q50 TGA, where the samples were heated in Ar from room temperature up to 500°C, with a scan rate of 10 °C min^{-1}.

The density was calculated from the weight of three volumetric flasks with 5 mL of each electrolyte. The temperature was 22°C ± 1°C and the pressure 0.1 ± 0.01 MPa.

The viscosity of the electrolytes was measured by using a ViscoClock unit with a Micro-Ubbelohde viscometer at the temperature of 22°C ± 1°C and the atmospheric pressure (0.1 ± 0.01 MPa). In order to study the viscosity of the electrolytes, two different diameters of the capillary have been used: 0.53 mm for solutions with molality from 0.5m to 2m (0.5m-1m-2m) and 0.96 mm from 3m to 5m.

The rheological properties of catholytes were evaluated with the rheometer HAAKE RS50, which was thermostated at 30° C, with the cone plate geometry (DC60 2°). The shear rate was firstly kept constant at 100 s^{-1} and then varied from 0 s^{-1} to 200 s^{-1} and return with a sweep rate of 0.2 s^{-1}.

The rheology of 5SP catholyte, because of the higher viscosity than that of the samples without carbon particles, was evaluated by a Couette flow in a concentric cylinder (Anton Paar Physica MCR301 rotational viscometer, method MCR301-SN827409), which was used under the same shear conditions.

Ionic conductivity of the investigated electrolyte TEGDME-based solutions was measured from -20°C as lower limit and up to 80°C as upper limit by CDM 210 Conductivity Meter (Radiometer Analytica) and an Amel standard cell with platinum electrodes. During the measurements, a Haake K40 thermocryostat (accuracy of 0.1°C) varied the temperature of the solutions that were kept at constant temperature for 1h before every single test.

The electrolyte conductivity of LiTFSI:DEMETFSI 0.5:1 was performed at HIU and obtained by the electrochemical impedance spectroscopy (EIS, Mmates-Biologic) using a sealed Pt-black/Pt-black cells (Mmates) with a k (cell constant) value of 1 cm^{-1} in a Julabo FP50 refrigerated/heating circulator. The k was evaluated using the standard 0.1 M KCl water solution

(Fluka). The conductivity values were collected in the range of 0-150 °C, waiting 5h per point.

Catholytes conductivity measurements were performed by the EIS from 200 kHz-100 mHz as frequency range, with 5 mV AC as perturbation. A homemade cell, with two stainless steel plates with area 0.44 cm^2 and spaced 0.6 cm, has been used. The distance/area ratio called cell constant k was 1.37 cm^{-1}.

These conductivities σ were calculated by the following Equation 7:

$$\sigma = \frac{1}{\rho} = \frac{k}{R} \quad (7)$$

where ρ (Ω cm) is the resistivity and R (Ω) is the intercept on the real impedance axis of the Nyquist plot at high frequencies (ca.100 kHz).

R was fit accordingly to the equivalent circuit RQ, where Q is a constant phase element (CPE).

The σ values include two terms that are the ionic conductivity of the ions in the electrolyte media (σ_{El}) and the electronic conductivity of the percolating network given by the carbon particles added to the electrolyte (σ_{PN}). Therefore, σ_{PN} values were thus obtained by the following subtraction:

$$\sigma_{PN} = \sigma - \sigma_{El} \quad (8)$$

where the σ is the total catholyte conductivity.

Scanning electron microscope (SEM) images of CP electrodes were obtained by a MERLIN Compact from ZEISS, equipped with an energy dispersive X-

ray analyser. Computed tomography (CT) of the CP was also performed by the instrument Phoenix nanotom M (Gemeasurement).

The SEM and CT images were collected during the joint mobility MIUR-DAAD programme that involved the research groups of Prof. Karl Heinz Pettinger from Hochschule Landshut (D) and the LEME. SEM images of the RVCSP were obtained by a Zeiss EVO 50.

The catholytes were investigated by transmission electron microscopy (TEM) technique with a Philips CM100 (accelerating voltage 80 kV) apparatus. TEGDME was selected as dispersing agent during the preparation of the samples.

To find out the morphologies of the carbon agglomerates in the catholyte, an Olympus XI71 microscope was also used. Furthermore, for a better investigation, the compound [9-(2-carboxyphenyl)-6-diethylamino-3-xanthenylidene]-diethylammonium chloride, known as rhodamine B, that dissolves in the electrolyte and gives fluorescence as a dye, was selected.

X-ray diffraction measurements (XRD) were performed by a PANalytical X'Pert PRO powder diffractometer equipped with a X'Celerator detector (CuKα radiation, $\lambda = 1.5406$ Å, 40 mA, 40 kV), radiation source and Ni filter by continuous scanning mode (0.04° 2θ s-1 scan rate, 0.05° 2θ step size). Micro Raman measurements of the catholytes were performed by an HORIBA-XploRA™PLUS with a $\lambda = 532$ nm laser.

FTIR analyses of the catholytes were obtained by a Bruker Optics Tensor 27 apparatus (2 cm^{-1} resolution).

2.3 Cells configuration and electrochemical characterization

The O_2 redox reaction (ORR) was investigated by galvanostatic and potentiostatic measurements in a thermostated glass electrochemical cell with 5 mL of electrolyte or catholyte and with CP or RVCSP as working electrodes. Li metal counter electrode (CE) was used in large excess and separated from the O_2-saturated electrolyte or catholyte by a porous frit to hinder the O_2 crossover and to avoid the parasitic reaction of the O_2 to the Li surface to form Li_2O. As reference electrode (RE), a silver wire in 6 10^{-2} M AgTFSI-PYR_{14}TFSI was used. The potential of the reference electrode was checked before use (ca. 3.3 V vs Li^+/Li). The electrode potentials in the Figures are always referred to the Li^+/Li couple. The electrolytes and catholytes were put in the cell and were mechanically stirred by a magnetic bar to promote the O_2 mass transport and to simulate flow condition. The cell temperature was 30° and was set by a HAAKE K40 thermocryostat. The scheme of the thermostated glass cell is reported in Figure 2.3.1a.

In a semi-flow cell configuration, for an easy and fast flow of the catholyte through the current collector (CC), the RVCSP (A = 0.385 cm^2) was preferred as working electrode, and the Li the CE. The RE was the same used in the electrochemical glass cell. The semi-flow cell scheme is reported in Figure 2.3.1.b (99).

A cross-shaped Teflon cell (BOLA) with 4 stacked lithium disks (0.534 g cm^3, 0.64 cm^2 0.300 mm each disk) and 2 dried and degassed fiber glass separators (Whatman GF/F) was assembled in the dry-box. The RVCSP-2GF/F-4Li bundle was sandwiched together and put between two stainless steel cylinders (A = 0.64 cm^2). In order to hinder the direct contact and thus,

prevent the reaction of O_2 with Li, only the RVCSP intercepted the O_2-saturated catholyte. Circulation of the catholyte through the semi-flow cell was obtained by a Watson-Marlow 120S/DV peristaltic pump, with a silicon tube (4.8 mm diameter). The SLRFAB was performed in absence of flow and at different flow rates of 35 mL min^{-1}, 71 mL min^{-1}, 108 mL min^{-1}, and 145 mL min^{-1} that were obtained by setting the peristaltic pump rotation at 50 rpm, 100 rpm, 150 rpm and 200 rpm, respectively.

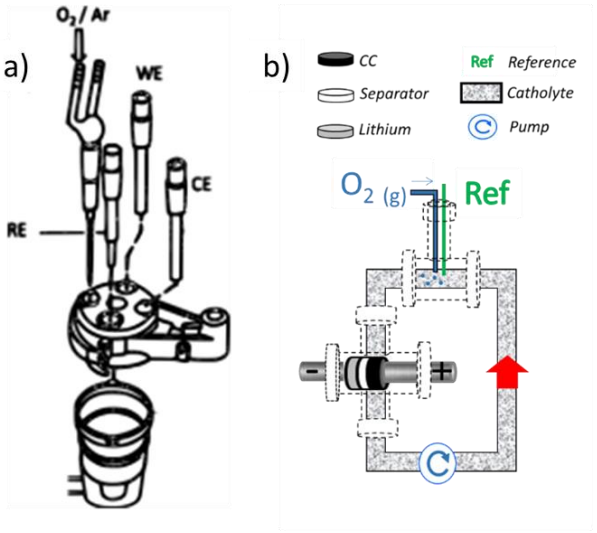

Figure 2.3.1. a) Scheme of the conventional electrochemical glass cell (5 ml) and b) of the flow cell. Reprinted from ref. (99), with permission from Elsevier.

The electrochemical tests were performed by a Bio-Logic VSP multichannel potentiostat/galvanostat with electrochemical impedance spectroscopy (EIS) module or by a Bio-Logic VMP multichannel potentiostat/galvanostat.
EIS was performed in the 1 kHz-100 mHz frequency range with 5 mV AC perturbation and by taking 10 points/decade.

At HIU, in order to study how different depositions can stop the dendrite formation upon cycling in a Li battery, symmetric cells (Li/Li) were assembled using both stainless steel 2032 coin cells (Figure 2.3.2) and T-cell Swagelok-type cells (Figure 2.3.3), having Li electrodes with 14 and 12 mm as diameter in the former and the latter, respectively.

A sheet of Whatman glass fiber GF/A soaked by the electrolyte (160-180 μl) was used as separator with 14 mm and 13 mm as diameter for the coin cells and the Swagelok-type, respectively. The cells were assembled in glove box.

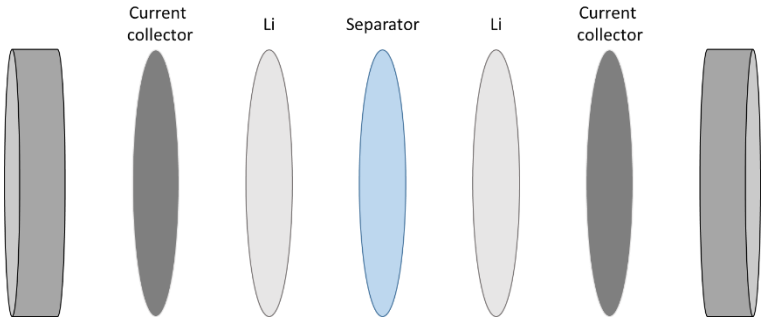

Figure 2.3.2. Schematic representation of Li/Li symmetric cell in stainless steel 2032 coin cell.

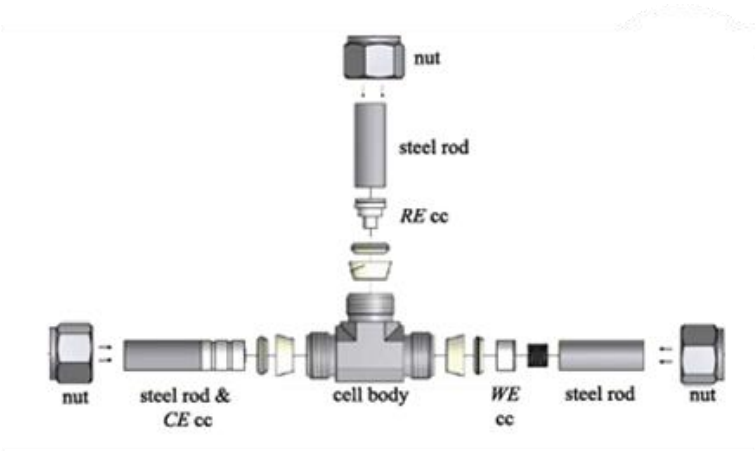

Figure 2.3.3. Schematic representation of T-Swagelok cell.

Cycling stability of Li and of Li with the protective layer in the LiTFSI:DEMETFSI electrolyte was evaluated at 40 °C by 2h-stripping/deposition cycle tests on symmetrical cells using different current densities ranging from 0.013 mA cm^{-2} up to 0.13 mA cm^{-2}.

The electrochemical characterization of Li/O_2 cells was performed at 40 °C using a top-meshed 2032 coin-cell with Li as anode (14 mm as diameter), a sheet of GF/A soaked by the electrolyte as separator (16 mm as diameter), and Super-P-coated GDL as cathode (16 mm as diameter), according to the scheme reported in Figure 2.3.4.

Each cell was then put in a static O_2 atmosphere using an air-tight glass tube flushed (Figure 2.3.5) for 15min with ultrapure O_2 (ALPHAGAZ™ 2, 99.9995%, Air liquid). The tube was then closed in order to limit any contamination.

The galvanostatic cycling tests were performed using a Maccor 4000 Battery Test System.

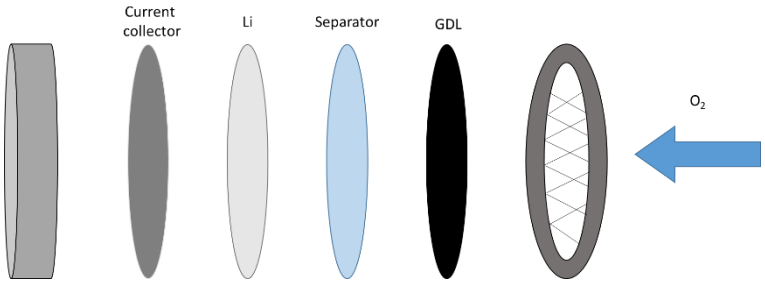

Figure 2.3.4. Scheme of top-meshed 2032 coin-cell.

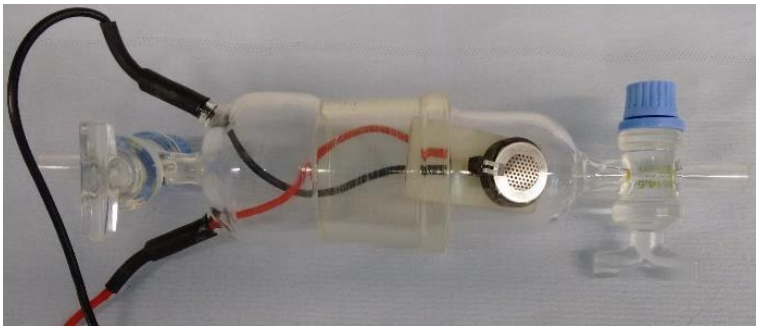

Figure 2.3.5. Pic of the top-meshed 2032 coin-cell in the air-tight glass tube.

Lastly, even though being dissolved in the electrolyte LiTFSI:DEMETFSI, the crosslinked PILs based on C_2VIm-FSI and 5-10% wt. C_4(VIm-FSI)$_2$ were tested by voltammetry in a glass electrochemical cell with GC (3 mm) as WE, Ni (6 mm) as CE and silver wire in 6 10^{-2} M AgTFSI-PYR_{14}TFSI as RE in the dry room.

They were dissolved in a 1:2 (vol:vol) ratio in acetonitrile (ACN) and saturated with O_2 for 20 min. The ORR was then investigated in order to study the stability of the superoxide in the Li^+-free PILs.

2.4 Scanning electrochemical microscope technique

ORR in different non-aqueous electrolytes for Li/O_2 battery has been studied by scanning electrochemical microscope (SECM) technique.

The measurements were carried out coupling a 910B SECM (CH Instruments) to an Eclipse Ti (Nikon) inverted microscope.

A bipotentiostat (range ± 10 V), coupled to the SECM and microscope, checked the potential applied to the tip and/or at the substrate vs. the reference electrode and measured the currents. The SECM probe (CH Instruments) was UME of Pt with a diameter of 10 μm, sealed in a glass capillary under vacuum. The tip was cleaned before use with diamond paper and put under sonicator bath for few seconds.

The cell scheme is shown in Figure 2.4.1. It includes a carbon paper (CP, Spectracorp USA, thickness 40 mils) coated by a high surface area activated carbon (AC) and used as counter electrode (CE). The composition of the ink used for AC deposition was 95% AC – 5% PVDF (Kynar HSV900) in NMP ink (28 mg of AC per mL). After the deposition, the current collectors were heated at 60 C° overnight to remove the NMP solvent.

The substrate was glassy carbon (GC) with a diameter of 5 mm (Tokai Carbon Ltd., Japan), which was cleaned with Al_2O_3. The potentials of the electrodes were checked by the use of a RE, a silver wire in 6 10^{-2} M AgTFSI-PYR_{14}TFSI and always referred vs. Li^+/Li couple. Lastly, the electrolytes were continuously fed with O_2 during the measurements for saturation. SECM operation lied in the feedback mode, which is the most common, and substrate generation/tip collection (SG/TC) mode. In the feedback mode, only the current of the tip is detected and is affected by the

substrate reactivity once the tip moves closer to the surface. If the substrate has a conductive surface, the tip current enhances, vice versa decreases. It is thus possible to determine if a surface is electrically conductive or becomes insulating during some electrochemical test.

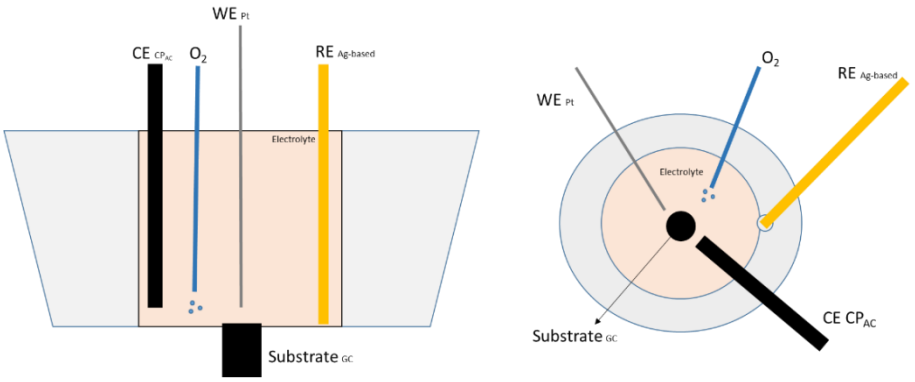

Figure 2.4.1. Scheme of the cell used in SECM.

In the SG/TC mode, the species generated from the substrate can be collected at the tip and the current is related to the presence and the amount of these species.

In Figure 2.4.2, the basic principles of feedback mode are shown (100). The steady state current, $i_{T,\infty}$ is measured at the tip when it is far from the substrate, like in the centre of the Figure 2.4.2. In this condition, the current is detected from the hemispherical diffusion of the species from the bulk of the electrolyte that reach the tip. When the tip instead approaches the surface of a conductive material, i.e. low L, the current at the tip is enhanced, $i_{T,} > i_{T,\infty}$, like the right of Figure 2.4.2. On the contrary, when the tip is close to an insulating substrate (i.e. low L), the diffusion i_T approaches zero, like the left

part of Figure 2.4.2. The curves $i_T/i_{T,\infty}$ vs. L are also called "approach curves" (101).

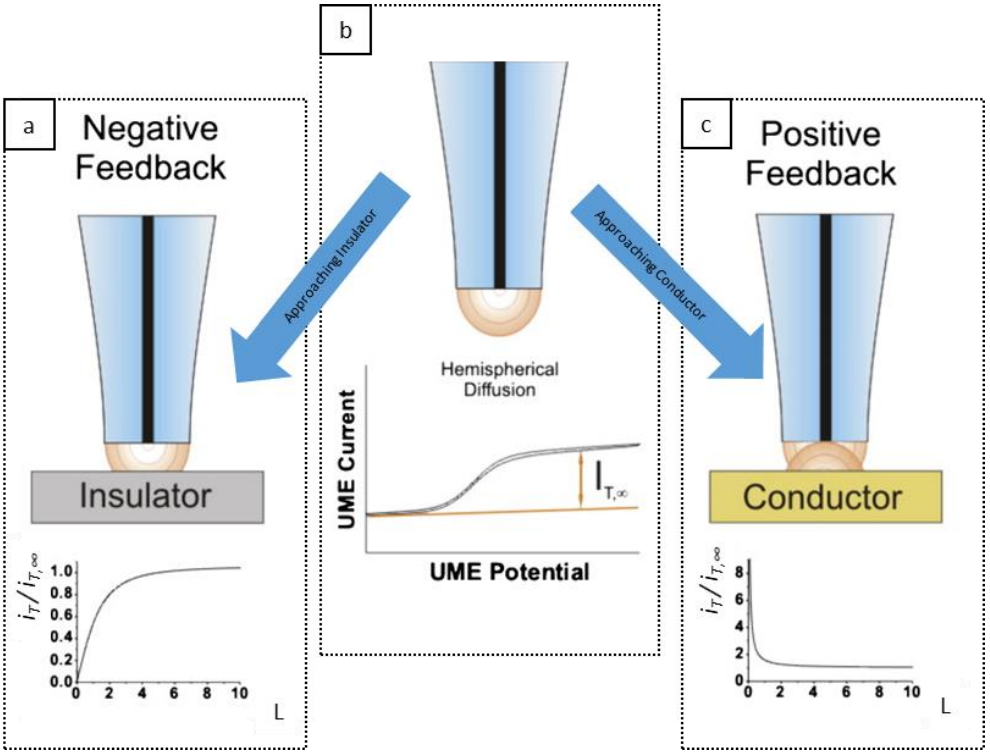

Figure 2.4.2. Basic principles of SECM feedback mode: a) near a conductive substrate b) far from the substrate c) near an insulating substrate. Reprinted from ref. (100), with permission from Elsevier.

In the SG/TC mode a current is measured at the tip due to the product of the reaction occurring at the substrate. During the scan, perpendicular to the substrate, the UME is brought next to the substrate so that it gets through the diffusion layer, generated by the substrate, and measures the concentration profile (Figure 2.4.3).

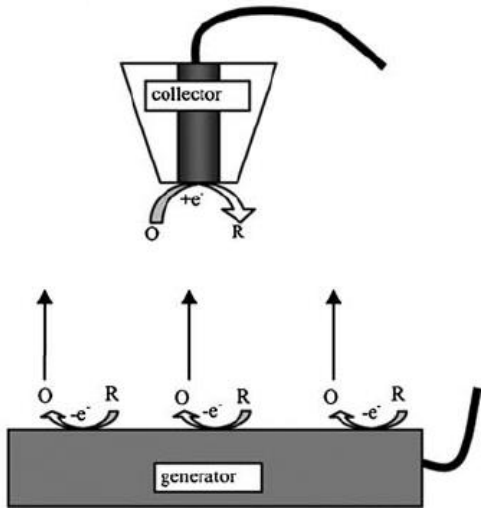

Figure 2.4.3. Basic principles of SECM substrate generation/tip collection (SG/TC) mode. Reprinted from ref. (101), with permission from the Royal Society of Chemistry.

2.5 Electrolyte gated transistor

The aim of the internship at the Polytechnic of Montréal (CA) was the investigation of the Li_2O_2 properties in different electrolytes using a electrolyte gated transistor (EGT). A scheme of a EGT is reported in Figure 2.5.1.

An EGT without any conducting material as channel, with gold as source/drain and activated carbon on carbon paper as gate electrode was first used.

The gate electrode was prepared using carbon paper (Spectracorp 2050) coated with a suspension containing activated carbon (PICACTIF SUPERCAP BP10, Pica, 28 mg ml^{-1}) and PVDF (KYNAR HSV900, 1.4 mg ml^{-1}) in NMP (Fluka, >99.0%). A thermal treatment at 60°C for 5 hours to

remove solvent and water traces in ambient atmosphere followed the coating step.

The electrolyte was 0.5 m LiTFSI in TEGDME, which was first saturated with O_2 for 20 minutes under stirring.

Gold source and drain electrodes were deposited on Si/SiO_2 with a source and drain distance of 10 μm. The gate electrode was activated carbon BP10 on carbon paper and due to its high surface area, was also the reference electrode. A PVDF membrane wetted by O_2-saturated electrolyte was placed between the gate electrode and the channel.

EGTs with titanium dioxide (TiO_2) and poly(3,4-ethylenedioxythiophene) (PEDOT) conducting materials as channel, with gold as source/drain and activated carbon on carbon paper as gate electrode were also used as tool for the Li_2O_2 formation.

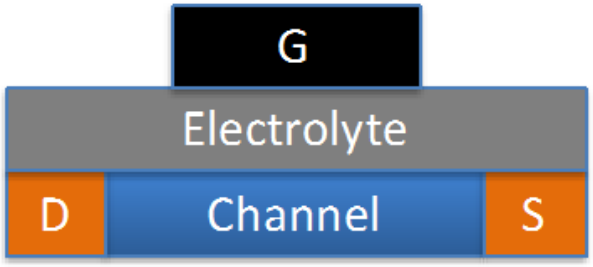

Figure 2.5.1. Scheme of the electrolyte gated transistor (EGT). G, D and S stand for gate, drain and source.

Chapter 3 Conventional and solvent-in-salt electrolyte based on LiTFSI and TEGDME in Li/O_2 battery

As previously discussed in Chapter 1, the electrolyte choice in the Li/O_2 battery performance has a noticeable role. Solvent-in-salt solutions can be used as designed electrolyte in Li/O_2 system. Chapter 3 deals with the investigation of the effect of the increasing of the Li salt concentration in the electrolyte based on tetraethylene glycol dimethyl ether (TEGDME) and lithium bis(trifluoromethanesulfonyl)imide (LiTFSI) in the chemical physical properties (Paragraph 3.1) and, more interestingly, in the ORR of aprotic Li/O_2 batteries (Paragraph 3.2). The results of the above cited section (Paragraph 3.1 and Paragraph 3.2) have been obtained during the master thesis of the student Francesca Messaggi and have been also reported in a paper (102), (103).

The O_2-saturated SIS electrolytes have been used to test the Li/O_2 battery during a galvanostatic discharge and the results compared to the conventional 0.5m LiTFSI-TEGDME. Once having assumed a higher amount of the discharge product deposited on the carbon paper (CP) cathode using the O_2-saturated 0.5m LiTFSI-TEGDME electrolyte, its surface was characterized by SEM, EDX and CT (Paragraph 3.3).

3.1 Physical chemical properties of LiTFSI–TEGDME solutions

The typical ionic concentration of electrolytes used in Li batteries has a value of about 1 mol L^{-1}, which features a low viscosity with a high ionic conductivity that are essential for high rate batteries.

On the other hand, some advantages can be exploited in more concentrated electrolytes, especially based on LiTFSI and TEGDME. The investigated solutions that have been studied cover the range from 0.5 m to 5 mol kg^{-1} (m), exploring both the salt-in-solvent and the solvent-in-salt regimes (Figure 3.1.1).

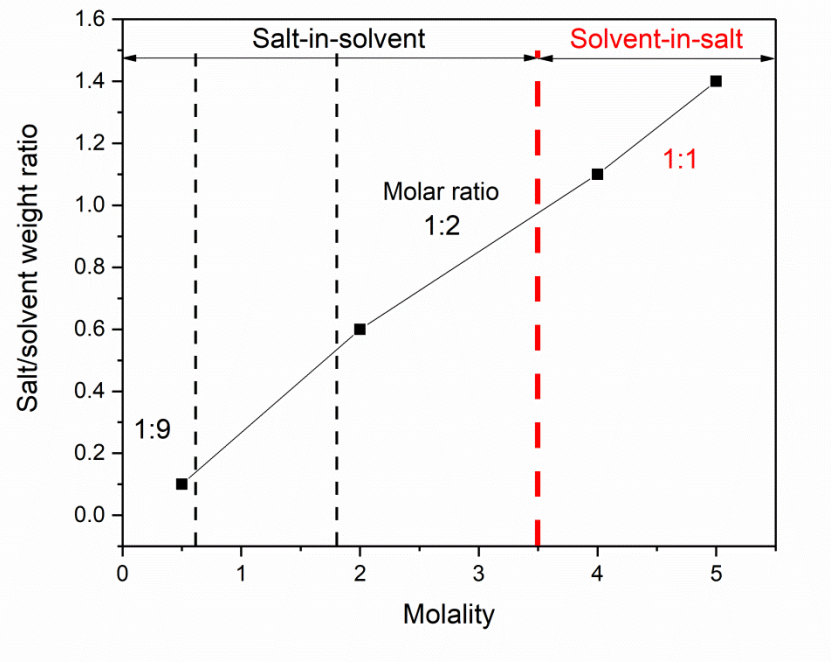

Figure 3.1.1. Classification of the studied solutions, according to the salt-in-solvent and solvent-in-salt range, depending on the molarity (m).

3.1.1 Thermal stability of the LiTFSI-TEGDME electrolytes

In order to study the thermal stability of the electrolytes, thermogravimetric analyses were performed. The obtained thermograms are shown in Figure 3.1.1.1 (103), where it is evident that the increasing of the salt content leads to an improved thermal stability. This is related to the resistance to thermal degradation and to the colligative properties of the superconcentrated electrolytes.

The first mass loss above about 100 °C is related to the TEGDME solvent evaporation, as it is confirmed by the thermogram of the pure TEGDME (black line). LiTFSI decomposition in the electrolytes begins at about 400°C and it is greater as the concentration of LiTFSI increases.

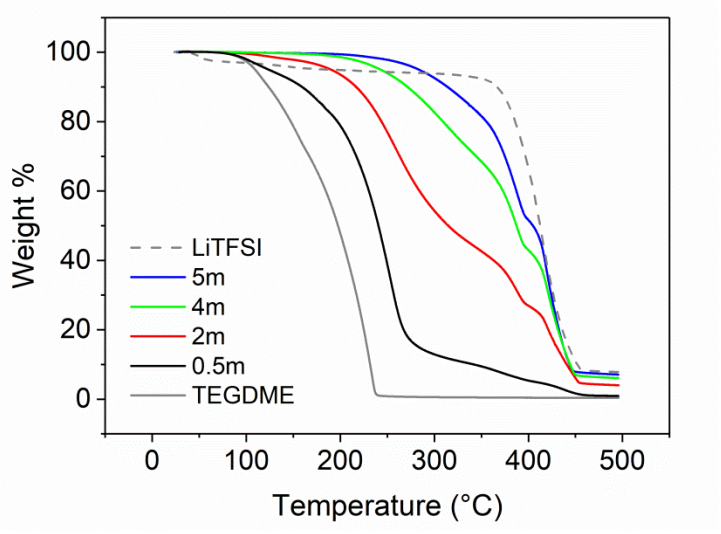

Figure 3.1.1.1. TGA curves of LiTFSI-TEGDME electrolytes in Ar. LiTFSI and TEGDME curves are reported as comparison. Reprinted and adapted from ref. (103), with permission from Elsevier.

These findings well fit with what has already been reported in literature and can be justified considering the reduced solvent volatility with the Li salt increase (104). Between TEGDME (grey line) and 0.5m (black line), only small changes are detected, while they rapidly increase with the more concentrated solutions, especially with 4m (green line) and 5m (blue line).
These results suggest that in electrolyte where the equimolar solution is approached, the TEGDME solvent molecules strongly coordinate the Li^+ cations to form the $[Li(glyme)]^+$ cation complex. The complexation effect can clarify why the highly concentrated mixtures with glymes are thermally more stable than low concentrated solutions, with an analogous stability of ILs (105).
This property is considered a great advantage for all the safety issues that Li batteries suffer.

3.1.2 Density, viscosity and ionic conductivity

The dynamic viscosity of a fluid is defined as its resistance to the shear flow and is a feature that must be considered for solutions that act as electrolytes or catholytes in batteries. It is also considered a key transport property that affects both the electrical conductivity and the ion diffusivity. Its value can also be calculated by multiplying the kinematic viscosity (ν) to the density of the solution (d) (Equation 9).

$$\eta = \nu \cdot d \tag{9}$$

The density values of the LiTFSI-TEGDME electrolytes at 21±1 °C was determined and the related dynamic viscosity was calculated.

Ionic conductivity (σ) (mS cm^{-1}) of a solution is the inverse of its resistivity, according to Equation 10:

$$\sigma = \frac{1}{R} \cdot \frac{d}{A} \quad (10)$$

where R is the resistance of the electrolyte, d is distance between the electrodes and A is the surface of the electrodes.

It represents the ability of the solution to conduct electricity and is strongly related to the motion of ions. The main factors that influence ionic specific conductivity are the temperature, the electrolyte viscosity, the ion concentration, the ion charge and mobility, and the ions tendency to form ionic couples.

Table 3.1.2.1 reports the salt-to-solvent molar ratio of the investigated electrolytes, (0.5, 2, 4 and 5 m), corresponding to 1:9, 1:2, 1:1.1 and 1:0.9 molar ratios, along with the corresponding viscosity, density, and conductivity. The values have been obtained at 20° C.

The LiTFSI:TEGDME molar ratio of the 4m is 1:1.1, therefore there is a 10% excess of solvent with respect to Li^+ cations, while in 5 m, the molar ratio is 1:0.9, which means that there is a 10% excess of LiTFSI.

The differences in the molar ratios in the electrolytes dramatically affect the viscosity values, while the ionic conductivity has still good values.

Table 3.1.2.1. Concentrations, dynamic viscosity, density, conductivity of the TEGDME-LiTFSI investigated solutions at 20°C as temperature.

Electrolyte	0.5m	2m	4m	5m
Dynamic viscosity (cP)	7.1	31	91	550
Density (g ml^{-1})	1.07	1.24	1.38	1.43
Conductivity (mS cm^{-1})	1.76	1.92	1.43	0.73

The 5m viscosity value dramatically increases to 550 cP, which is about six times that one of 4 m (91 cP). This marks a clear discontinuity of the trend and can be an indication of some structure change of the electrolyte, once increasing the salt concentration.

In 4m there is only one free molecule of TEGDME every ten that are engaged with the Li^+ complexation, while in 5m solution there are no free TEGDME molecules at all.

This strongly affects the rheological properties of the solutions, too: the presence of 10% of free TEGDME helps the flow, maintaining the viscosity in a value similar to low-concentrated solutions.

Interestingly, the conductivity value of 5m is similar to the 4m electrolyte, despite the much higher viscosity. Specifically, with a change of viscosity from 90 cP to 550 cP, for 4m and 5m respectively, the σ changes from 1.4 mS cm^{-1} to 0.7 mS cm^{-1}. This suggests that the IL-like structure of SIS solutions must have unique features that lead a different conduction mechanism with respect to the classical electrolytes.

3.2 Voltammetric study of ORR in different solutions: from salt-in-solvent to SIS

Cyclic voltammetry is a powerful technique to investigate the ORR process that takes place in Li/O_2 battery and it was carried out using a glassy carbon electrode (GC) in the O_2-saturated solutions.

Figure 3.2.1 (a, b) reports, as examples, the CVs at different scan rates (5, 10, 20, 50, 100 and 200 mV s^{-1}) of the GC in the O_2-saturated solutions of 0.5m and 4m LiTFSI-TEGDME. The CVs of the GC in the O_2-saturated solutions at 20 mV s^{-1} at the concentrations of 0.1m, 0.5m, 2m, 4m and 5m LiTFSI-TEGDME are compared in Figure 3.2.1c and the CVs at 20 mV s^{-1} of GC in PYR_{14}TFSI IL with and without the Li salt LiTFSI are reported in Figure 3.2.1.d (103).

Furthermore, Table 3.2.1 reports the key parameters of the CVs at 20 mV s^{-1} and summarizes the reduction and oxidation potentials, currents and charge in the investigated electrolyte.

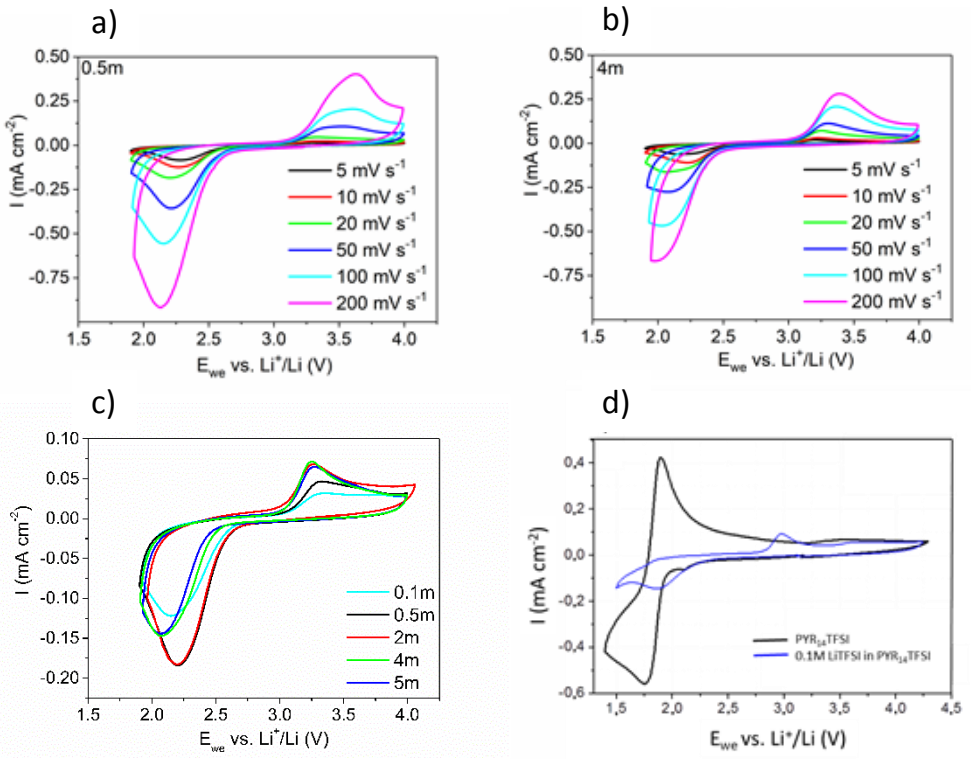

Figure 3.2.1. CVs of a glassy carbon electrode (GC) in O_2-saturated LiTFSI-TEGDME solutions: a) 0.5m, b) 4m, c) at 20 mV s^{-1}. d) CVs of a glassy carbon electrode (GC) in O_2-saturated $PYR_{14}TFSI$ IL with and without LiTFSI at 20 mV s^{-1}. Reprinted and adapted from ref. (103), with permission from Elsevier.

Table 3.2.1. Reduction and oxidation peak potentials (E_{red}, E_{ox}), peak currents ($I_{p,red}$, $I_{p,ox}$), reduction charge (Q_{red}) and efficiency (Q_{red}/Q_{ox}) of the CVs at 20 mV s^{-1} for the LiTFSI-TEGDME electrolytes.

Electrolyte	0.1m	0.5m	2m	4m	5m
E_{red} (V vs. Li^+/Li)	2.15	2.20	2.19	2.07	2.07
E_{ox} (V vs. Li^+/Li)	3.35	3.32	3.26	3.25	3.27
$I_{p\ red}$ (μA)	2.2	3.3	4.8	5.0	4.6
$I_{p\ ox}$ (μA)	2.2	3.3	4.8	5.0	4.6
Q_{red} (mC)	-0.247	-0.349	-0.321	-0.30	-0.276
Q_{ox}/Q_{red} (%)	43%	38%	65%	53%	57%

The CVs reported in Figure 3.2.1(a,b) are similar in shape, with a peak in reduction around 2.00 V vs. Li^+/Li and a broader peak in oxidation around 3.50 V vs. Li^+/Li.

The reduction peak around 2.00 V vs. Li^+/Li is related to O_2 reduction to superoxide (Equation 3), which in turn gives Li_2O_2 by chemical dismutation (or disproportion) (Equation 4) and/or electrochemical reduction (Equation 5).

The broad anodic peak around 3.50 V vs. Li^+/Li is attributed to the Li_2O_2 reoxidation to give back O_2 (Equation 12) (106):

$$Li_2O_2 \rightarrow O_2 + 2\,Li^+ + 2\,e^- \qquad (12)$$

The process is electrochemically irreversible and this is mainly related to the presence of Li^+ ions, as already discussed in Chapter 1 (106), (107).

The fact that during the ORR in Li/O_2 battery two different processes occur (dismutation vs. second electrochemical reduction) makes the understanding of the reaction mechanism extremely difficult.

Figure 3.2.1c shows a shift in the potential value in the peak of reduction (E_{red}) towards more positive potential values, accompanying by an increase of the peak current of reduction ($I_{p,red}$), passing from 0.1m to 2m. Furthermore, during the oxidation, there is a shift to negative values of the potential and there is an increasing of the peak current in oxidation ($I_{p,ox}$). These trends, specifically the change in E_{red}, can be ascribed to the increase of Li^+ concentration and can be justified considering the hard Li^+ Lewis acidity.

As already discussed in Chapter 1, and referring to the HSAB theory, soft Lewis acid cations stabilise the soft Lewis base $O_2^{\bullet-}$ anion, while hard Lewis acid cations, like Li^+, have a better affinity with hard Lewis bases like O_2^{-2}, promoting the chemical dismutation of Equation 4.

ORR is considered to be a quasi-reversible mono-electronic process that involves the O_2/ $O_2^{\bullet-}$ redox couple in Li^+ free electrolytes and with soft Lewis acid cations. This occurs in media like the IL $PYR_{14}TFSI$, as reported in Figure 3.2.1d. O_2 reduction forms a stable $O_2^{\bullet-}$ at 1.75 V vs. Li^+/Li with the relative oxidation at 1.9 V vs. Li^+/Li without LiTFSI (black curve). In the presence of Li^+, the LiO_2 causes the dismutation to peroxide and O_2, bringing about the formation of the passivation layer on the electrode (blue curve).

The result is that ORR becomes electrochemically irreversible: the E_{red} CV is shifted to more positive values (according the chemical reactions following the electrochemical reaction), the $I_{p,red}$ and $I_{p,ox}$ peak currents decrease, and the reversible $O_2^{\bullet-}$ oxidation peak is replaced by a broader peak at much higher potentials that is related to the Li_2O_2 oxidation (108).

Therefore, the anticipation of the E_{red} moving from 0.1 m to 0.5 m LiTFSI in TEGDME is due to the increase of Li^+ concentration, which favours the chemical dismutation (Figure 3.2.1c).

This brings about to an higher $I_{p,red}$ because the higher O_2 concentration at the electrode/electrolyte interface with respect to the bulk and to an higher $I_{p,ox}$ currents because more Li_2O_2 is formed during the dismutation (Equation 4 and Equation 12).

However, the values of E_{red} and $I_{p,red}$ in 2m do not differ from those in the 0.5m solution. In superconcentrated solutions (4m and 5m), unpredicted results are instead obtained. In 4m and 5m, the E_{red} moves towards left, i.e. to more negative values, and $I_{p,red}$ decreases with respect to the 2m and 0.5m cases: the Li^+ ion complexation acted by glyme molecules starts to be thus effective in these solutions. Even though the Li^+ cations amount is higher respect to the 0.5m, their Lewis acidity is softened by the coordination of the TEGDME molecules.

The $[Li\ (glyme)_1]^+$ complex thus stabilizes the $O_2^{\bullet-}$, rendering the chemical dismutation less effective. As a result, the amounts of both O_2 and Li_2O_2 produced during the chemical dismutation are lower (Equation 4).

As reported in Figure 3.2.1c, because of the lower amount of O_2 at the electrode surface, the values $I_{p,red}$ are low too in 4m and 5m.

The $I_{p,ox}$ is related to the Li_2O_2 deposited or adsorbed at the electrode surface that depends on the stability of the intermediate species and on the electrolyte viscosity.

The increase of viscosity moving from 0.5m to 2m (7 cP and 31 cP, according to Table 3.1.2.1) causes the Li_2O_2 confinement near the GC surface, increasing of the $I_{p,ox}$ values (Figure 3.2.1c).

In 4m and 5m the $I_{p,ox}$ does not change because the effect of the lower amount of Li_2O_2, produced at the electrode surface, is balanced by the higher viscosity of the solution that hinders any Li_2O_2 diffusion in the bulk.

The higher stability of $O_2^{\bullet-}$ in SISs and the lower amount of solid and passivating Li_2O_2 at the electrode surface are expected effects that can beneficially suppress the Li_2O_2 film growth on the electrode surface and favour its solution formation mechanism.

The adsorption and interaction strength of the reduction product Li_2O_2 on the electrode surface can be also an indication of the different mechanism in the media.

A strong adsorption of the oxidation reactant results in a shift towards higher E_{ox} in the anodic scan (108). The fact that the E_{ox} values in 2m, 4m and 5m (3.26, 3.25, 3.27 V vs. Li^+/Li) are lower than that of the 0.5m (3.32 V vs. Li^+/Li) suggests that the adsorption of Li_2O_2 on the electrode surface is weaker at the highest salt concentrations.

A further indication that the Li_2O_2 formation mechanism changes from conventional low-concentrated electrolytes to the superconcentrated solutions is given by the analysis of the peak currents (I_p) with the scan rate (v_{scan}).

Like for a surface reaction, the peak currents linearly increase with v_{scan} in the case of strongly adsorbed reactants.

For processes involving species in solutions that are moreover controlled by the mass transport instead, the peak currents linearly increase with the square root of v_{scan} (108).

The trends of Log I_p with Log v_{scan} of the CVs at different scan rates are shown in Figure 3.2.2 (103), with the currents given in mA and the scan rate in mV s^{-1}. Table 3.2.2 summarizes the slope for both the reduction and oxidation reaction ($slope_{red}$ and $slope_{ox}$).

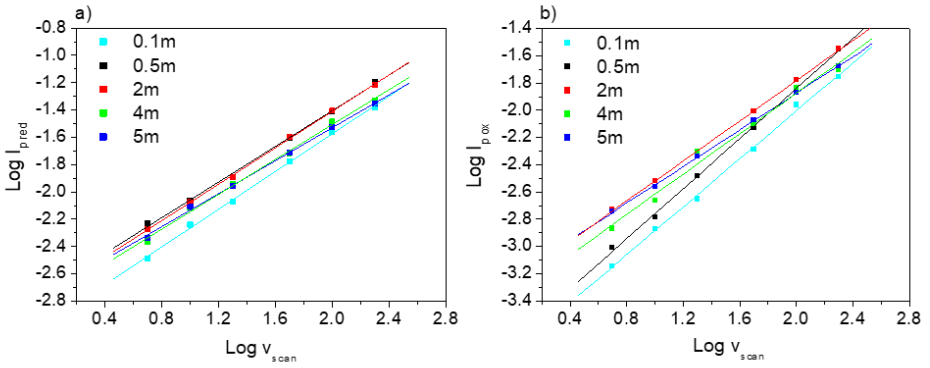

Figure 3.2.2. a) Logarithm plots of the reduction peak currents ($LogI_{p,red}$) with the scan rate (v_{scan}) and b) logarithm plots of the oxidation peak currents ($LogI_{p,ox}$) with the scan rate (v_{scan}) of the GC in the O_2-saturated LiTFSI-TEGDME solutions. Reprinted from ref. (103), with permission from Elsevier.

Table 3.2.2. Slope of $LogI_{p,red}$ and $LogI_{p,ox}$ with the Log v_{scan} of the CVs.

Electrolyte	0.1m	0.5m	2m	4m	5m
$Slope_{red}$	0.69	0.65	0.67	0.64	0.60
$Slope_{ox}$	0.88	0.91	0.73	0.74	0.67

During the O_2 reduction, the values of the slope are ca. 0.6-0.7 for the electrolytes with different salt concentrations, confirming that the process is limited by the diffusion of the reactant, which is O_2, in the solutions (108). Furthermore, $slope_{ox}$ values at the lowest concentrations (0.1m and 0.5m) are ca. 0.9, indicating that the anodic process is a surface reaction and that the Li_2O_2 oxidation previously formed during the reduction is a solid product that is strongly absorbed at the electrode surface (108).

Instead, for the highest concentrations, the $I_{p,ox}$ tends to be proportional to the square root of the scan rate, i.e. the $slope_{ox}$ is 0.73, 0.74 and 0.67 for 2m, 4m and 5m, respectively. This can suggest that in concentrated electrolytes, the oxidation process loses the surface reaction feature, becoming more similar to a process controlled by Li_2O_2 mass transport in solution.

Oxidation reaction in SISs thus involves Li_2O_2 that are weakly adsorbed on the GC, supporting the theory that, depending on the electrolyte, the nature and morphology of Li_2O_2 changes.

Figure 3.2.3 shows the trend of the O_2 reduction charge (Q_{red}) over repeated CV cycles at 20 mV s^{-1} obtained without cleaning the GC working electrode during the scanning. The charge retention Figure 3.2.3 is higher for 4m and 5m solutions than for 0.5m and 2m (103). These results suggest that the

superconcentrated solutions can improve the Li/O_2 cycling performance allowing a better capacity retention during the cycling repetition.

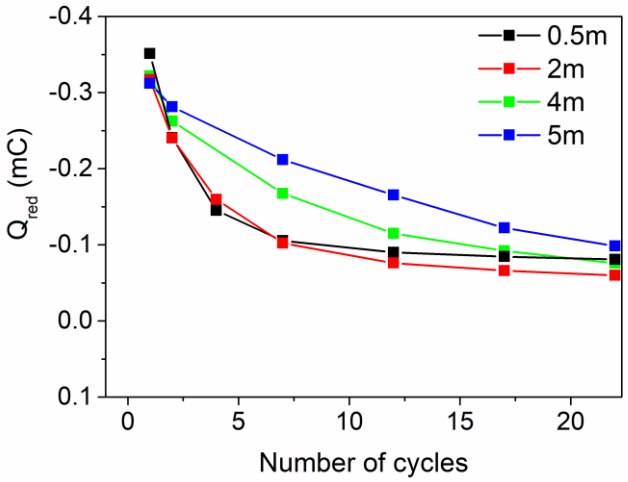

Figure 3.2.3. a) Logarithm plots of the reduction peak currents ($LogI_{p,red}$) with the scan rate (v_{scan}) and b) logarithm plots of the oxidation peak currents ($LogI_{p,ox}$) with the scan rate (v_{scan}) of the GC in the O_2-saturated LiTFSI-TEGDME solutions. Reprinted and adapted from ref. (103), with permission from Elsevier.

Moreover, the high viscosity values of 4m and 5m solutions, being 91 cP and 550 cP respectively, do not limit the ORR kinetic rates. Indeed, ORR peak currents are similar to those of the low-concentrated electrolytes, as shown in Figure 3.2.1c. The peak currents depend on the diffusion coefficient (D) and on the concentration (C) of O_2 (108). Thus, because a decrease of D with the electrolyte viscosity with increasing of the salt is expected, a corresponding rising of the C values, which balances the mass transport delay, occurs in the superconcentrated electrolytes that have been studied.

This can be explained taking into account the higher amount of LiTFSI salt, corresponding to a higher content of fluorine, which is already well known to raise the O_2 solubility (107), (109), (110).

3.3 Galvanostatic test of Li/O_2 battery in different electrolytes

As already reported in Paragraph 3.2, the ORR kinetics in SIS could be high enough for Li/O_2 battery.

With the Li as CE and the Ag-based RE (Paragraph 2.3), the CP has been used as WE (A=0.45 cm^2) in glass electrochemical cell, where the electrolytes were saturated with O_2 and stirred to hinder the O_2-mass transport limit that affects the capacity in Li/O_2 battery (77).

Figure 3.3.1 reports the galvanostatic profile of the CP potential during 5h of discharge at a current density of 0.05 mA cm^{-2} (0.25 mAh cm^{-2} as areal capacity), in a Li/O_2 cell with the O_2-saturated solutions as electrolytes (0.5m, 2m, 4m and 5m) (103).

The CP was not coated by any porous carbon like SP in order to render the system as simple as possible and to focus the study only on the electrolyte effect. As result, the CP potentials improves of 200 mV, moving from 0.5m to 5m, i.e. from 2.52 to 2.72 V vs. Li^+/Li, respectively. This can be related to the high concentration of the fluorinated $TFSI^-$ anion in the SISs (Paragraph 3.2), which improves the O_2 solubility and contribute to decreases the overpotential by increasing O_2 concentration.

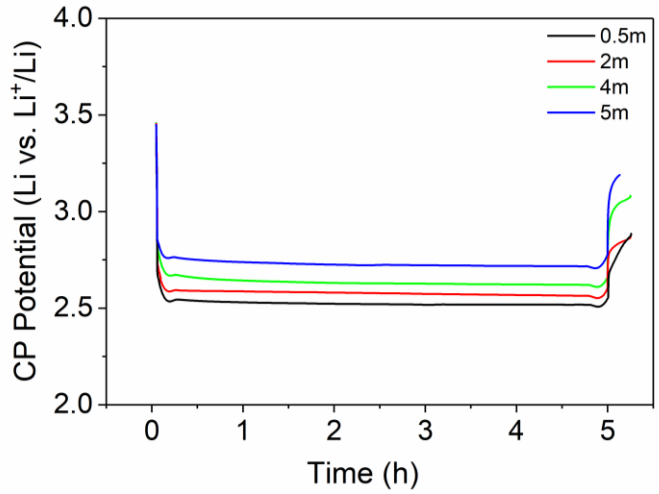

Figure 3.3.1. CP (0.45 cm^2) potential during galvanostatic discharges at 0.05 mA cm^{-2} in Li/O_2 glass electrochemical cell with stirred and O_2-saturated 0.5m, 2m, 4m and 5m electrolytes. Reprinted and adapted from ref. (103), with permission from Elsevier.

In the frame of the MIUR-DAAD Joint Mobility Programme, some CP coated with SP (CPSP) have been characterized by SEM and CT techniques. SP has been coated con the CP current collector to increase the capacity performance in the Li/O_2 battery.

The 0.5m (0.5m LiTFSI-TEGDME) electrolyte has been selected to maximize the Li_2O_2 growth and to characterize the deposited layer on CP by SEM and CT. The galvanostatic test lay in 24h of discharge at 0.25 mA cm^{-2}, corresponding to 6 mAh cm^{-2}, with the CP (WE) limit of 2.00 V vs. Li^+/Li and eventually the recharge at the same current density with the WE upper limit of 3.90 V vs. Li^+/Li. The positive cut-off has been selected to limit the electrolyte and carbon degradation. Figure 3.3.2 reports the CPSP potential profile during the electrochemical test. The mass loading was 2.4 and 2.0 mg cm^{-2}, respectively.

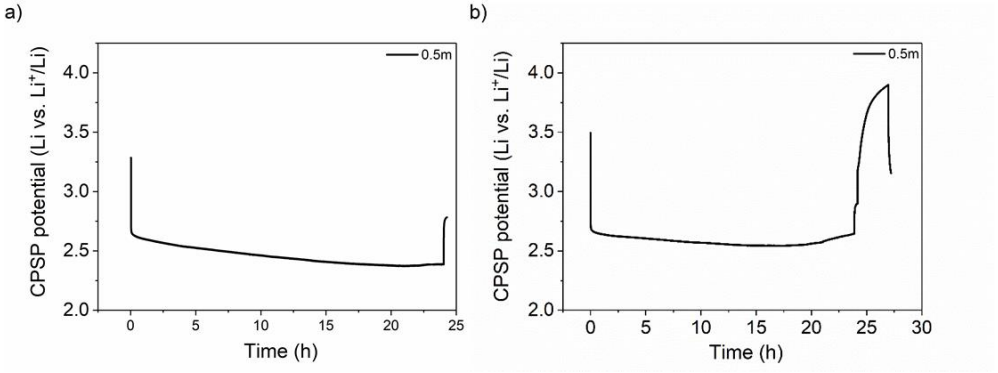

Figure 3.3.2. CPSP (A=0.5 cm^2) electrode potential during a) galvanostatic discharge of 24h b) galvanostatic discharge of 24h and recharge in Li/O_2 glass electrochemical cell with stirred and O_2-saturated 0.5m electrolyte. Current density was 0.25 mA cm^{-2}.

During the discharge of 24h, the CPSP potential was about 2.50-2.60 V vs. Li^+/Li, while the recharge step took place only 3h, as reported in Figure 3.3.2b.

The working electrode CPSP used to get the results reported in Figure 3.3.2b was then characterized by SEM technique and the images (Figure 3.3.3d-f) are compared to the pristine CPSP (Figure 3.3.3a-c).

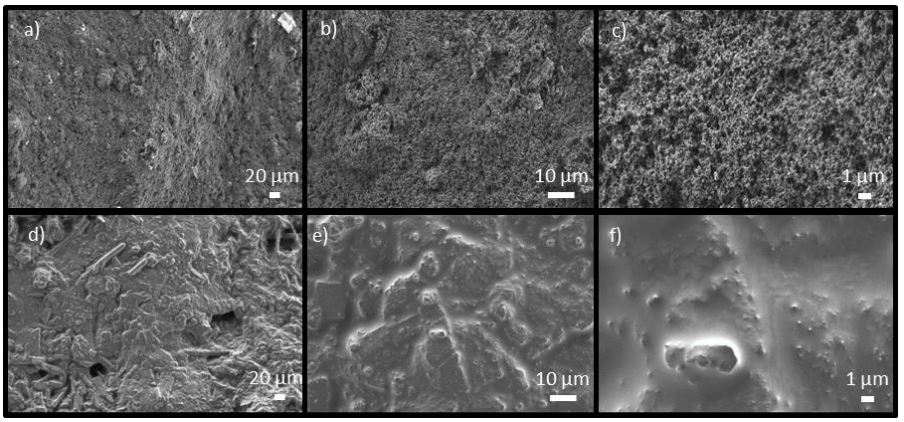

Figure 3.3.3. SEM images of pristine CPSP electrode (a-c) and after galvanostatic discharge of 24h and recharge at 0.25 mA cm^{-2} in Li/O_2 battery reported in Figure 3.3.2b (d-f).

According to the profile of Figure 3.3.2b and the SEM images reported in Figure 3.3.3(d-f), during the discharge, a passivation layer, probably due to the deposition of insulating Li_2O_2 is detected. This deposition causes the clogging of the pores of the CPSP, respect to the pristine one. During the recharge, the amount is not totally converted to O_2 again and remains to the electrode surface, being easily detectable.

Furthermore, the energy-dispersive X-ray spectroscopy (EDX) was performed to the pristine (Figure 3.3.4) and to the used CPSP in the discharge/recharge test of Figure 3.1.2b (Figure 3.3.5).

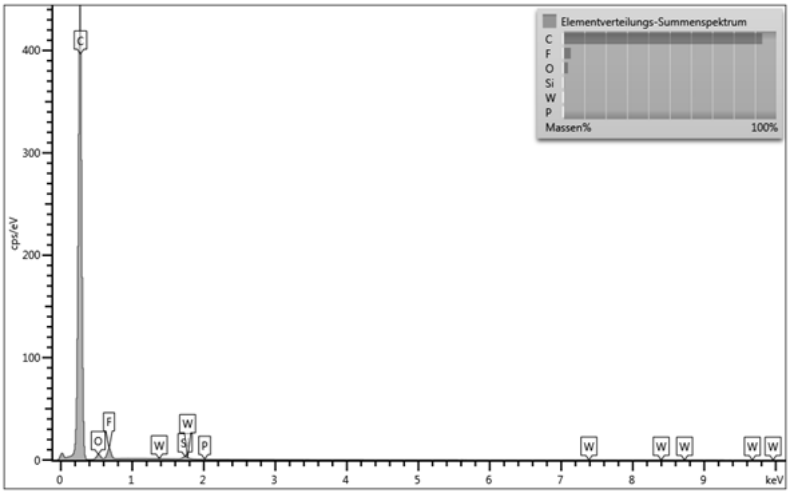

Figure 3.3.4. EDX analysis of pristine CPSP electrode.

In the pristine CPSP, as expected, there is a high content of C and F atom, the former due to the carbon presence of SP and the latter probably to the PVDF used as binder to deposit the SP.

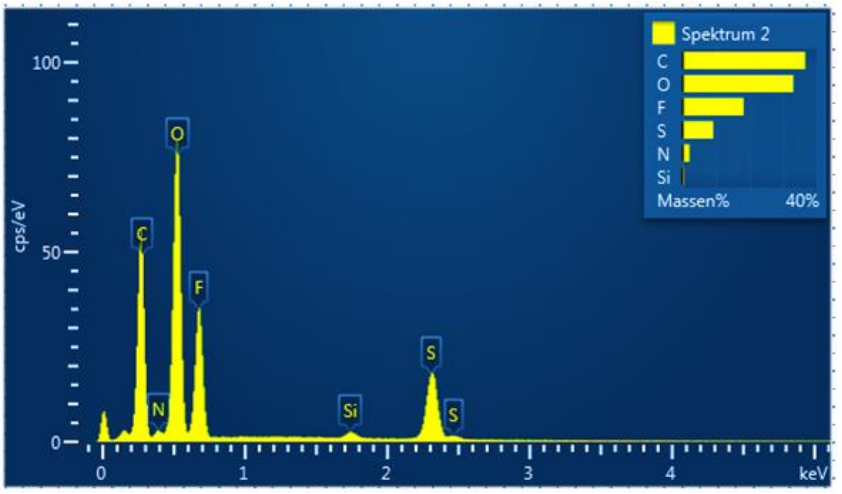

Figure 3.3.5. EDX analysis of CPSP electrode after galvanostatic discharge of 24h and recharge at 0.25 mA cm^{-2} in Li/O_2 battery reported in Figure 3.3.2b and Figure 3.3.3.d-f.

On the other hand, as reported in Figure 3.3.5, the EDX of the CPSP used in the discharge/recharge test reveals that the higher content of O atom, and the lower amount of C atom. This is probably due to the passivation by Li_2O_2 product on the carbon-based surface.

Table 3.3.1 reports the atom amount in percentage of the element collected by EDX on the CPSP electrode used during the electrochemical test reported in Figure 3.3.2b.

By EDX was possible to reveal also other elements, i.e. F, N and S, due to the presence of the $TFSI^-$ anion which degrades on the CPSP surface during the battery operation as already reported (111).

Table 3.3.1. Table containing the atom % collected by EDX on the CPSP sample used during the electrochemical test reported in Figure 3.3.2b.

Element	Atom %
S	4.40
Si	0.30
F	14.75
O	31.65
N	2.30
C	46.60
Tot.	100

The CPSP electrode discharged for 24h (Figure 3.3.2a) was characterized by CT and one image of the cross section is reported in Figure 3.3.6.
As indicated in the image, two different layers on the CP are present that can be related to the deposition of SP carbon and to the Li_2O_2 deposition, the latter being the outermost.

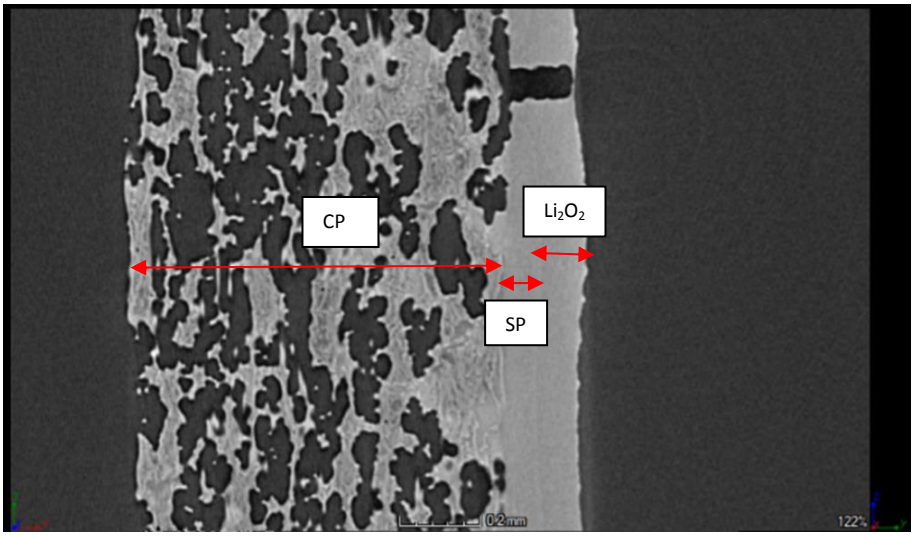

Figure 3.3.6. CT of the CPSP electrode after galvanostatic discharge of 24h at 0.25 mA cm^{-2} in Li/O_2 battery reported in Figure 3.3.2a.

3.4 Conclusions

Chapter 3 deals the use of LiTFSI-TEGDME based electrolyte in Li/O_2 battery, featuring different Li concentration. The investigated electrolyte has been 0.5 m, 2 m, 4 m and 5 m LiTFSI in TEGDME (0.5m, 2m, 4m and 5m). The electrolyte 0.1 m LiTFSI in TEGDME (0.1m) has been used in part of

the study. The physical chemical characterization suggests that superconcentrated solvent-in-salt solutions (SIS), i.e. 4m and 5m, have peculiar features, like better thermal stability than the conventional ionic concentrated electrolyte (Paragraph 3.1.1) and reasonable ionic conductivity considering their high viscosity (Paragraph 3.1.2). This is related to the ionic liquid (IL)-like structure of the SISs where the Li^+ cation is coordinated by a single TEGDME molecule to form a big complex.

The voltammetric study reported in Paragraph 3.2, clearly demonstrates that Li concentration in the electrolyte dramatically affects the ORR in Li/O_2 battery. The Li_2O_2 formation process shifts from a surface growth to a solution production mechanism, moving from salt-in-solvent, i.e. conventional low-concentrated to SIS solutions. Consequently, cycling stability of Li/O_2 batteries with SIS is improved (Figure 3.2.3). Fast ORR kinetics in SIS are also feasible due to the high O_2 concentration that mitigates the overpotential during the discharge, as demonstrate in the galvanostatic test reported in Figure 3.3.1. The surface characterization by SEM and CT of the cathode CPSP used in Li/O_2 cell with the 0.5m (0.5m LiTFSI-TEGDME) highlights the feature of the thick passivation layer formed during the discharge, deriving from the Li_2O_2 surface growth (Paragraph 3.3).

Chapter 4

Scanning electrochemical microscope and electrolyte-gated transistor as probes to define ORR in electrolytes for Li/O_2 battery

As reported in Paragraph 3.2, Li^+ concentration in the electrolytes based on tetraethylene glycol dimethyl ether (TEGDME) and lithium bis(trifluoromethanesulfonyl)imide (LiTFSI) dramatically affects the Li_2O_2 formation mechanism. The latter really depends on the Lewis acidity of the Li^+, which decreases by the coordination of a single molecule of TEGDME per cation. In Chapter 4, the scanning electrochemical microscopy (SECM), which works using an ultramicroelectrode as probe, has been used for the first time as analytical tool to further investigate the ORR mechanism in conventional TEGDME - 0.5m LiTFSI (0.5m) and SIS electrolyte TEGDME - 5m LiTFSI (5m). The results are also compared to those obtained with the ionic liquid (IL) 1-butyl-1-methylpyrrolidinium bis(trifluoromethanesulfonyl)imide ($PYR_{14}TFSI$), with or without LiTFSI salt (Paragraph 4.1. and Paragraph 4.2). The use of SECM was carried out in the laboratory of Prof. Stefania Rapino of the Department of Chemistry "Giacomo Ciamician" - Bologna University.

Furthermore, during the internship at the Polytechnic of Montréal under the supervision of Prof. Fabio Cicoira (April 1st, 2017 – July 31th, 2017), the use of electrolyte gated transistors as analytical tool to detect ORR products in several electrolyte is discussed in Paragraph 4.3.

4.1 ORR in $PYR_{14}TFSI$ w and w/o LiTFSI by SECM

In this PhD thesis, in order to study the ORR mechanism in different electrolytes for Li/O_2 battery by SECM, as mentioned in Paragraph 2.4, the substrate generation/tip collection (SG/TC) and the feedback modes have been used. During the SG/TC mode, a voltammetry at 20 mV s^{-1} of the GC used as substrate was performed in the O_2-saturated $PYR_{14}TFSI$ IL and $PYR_{14}TFSI$ – 0.1M LiTFSI electrolyte (Figure 4.1.1a). At the same time, the response by the Pt tip used as WE and placed 5 μm above the GC was collected with a voltammetry at 20 mV s^{-1} (Figure 4.1.1b).

As already mentioned in Paragraph 3.2 and reported in Figure 3.2.1.d, in Li^+ free $PYR_{14}TFSI$, with the PYR_{14}^+ cation having low Lewis acidity, the ORR of the GC substrate involves the O_2/ $O_2^{\bullet-}$ redox couple (black curve in Figure 4.1.1a). At the contrary, in the $PYR_{14}TFSI$ – 0.1M LiTFSI electrolyte, the superoxide is not stable and quickly gives chemical disproportion to O_2 and Li_2O_2 (blue curve in Figure 4.1.1a).

More interestingly and by the use of SECM, in the Li^+-free $PYR_{14}TFSI$, the voltammetry of the Pt probe reveals an anodic peak at around 2.50 V vs. Li^+/Li, referring to the oxidation of the $O_2^{\bullet-}$. This species is stable enough in the media to be collected at 5 μm from the substrate. On the contrary, the voltammetry of the Pt tip in the $PYR_{14}TFSI$ – 0.1M LiTFSI electrolyte, as expected, is very flat and does not reveal any peak, probably due to the passivation of both GC and Pt.

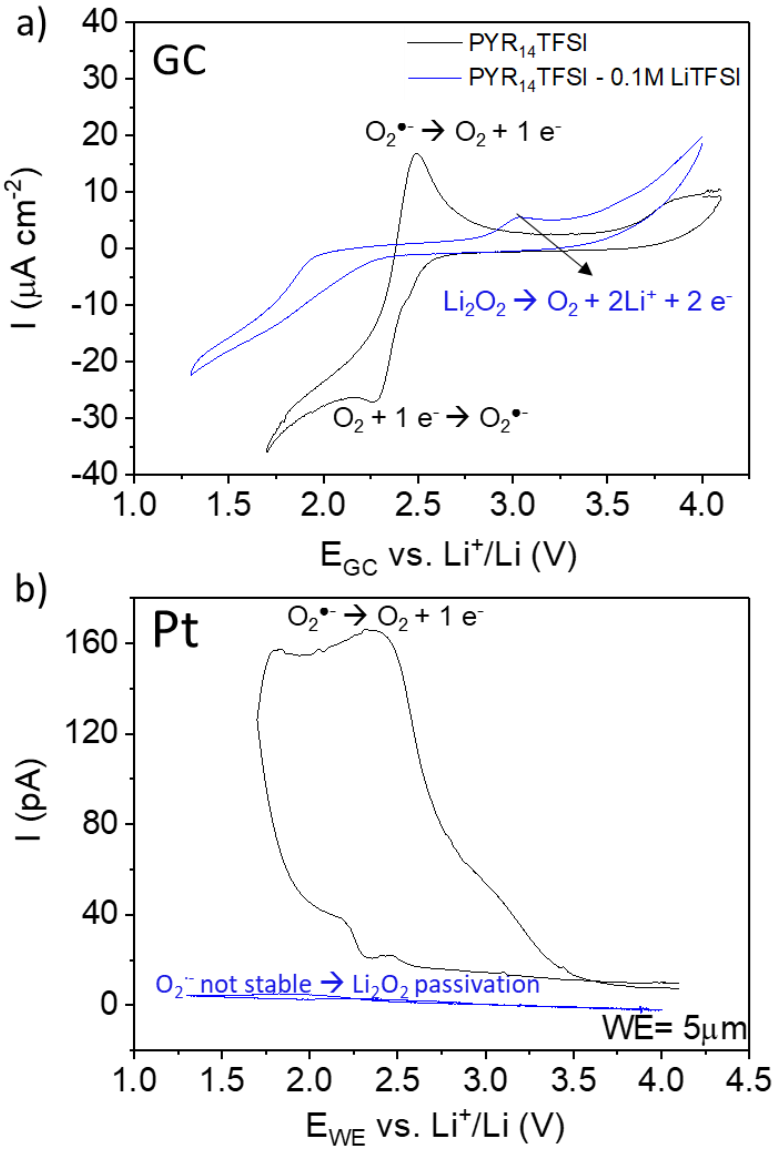

Figure 4.1.1. a) CVs in SG/TC mode at 20 mV s^{-1} of GC in O_2-saturated $PYR_{14}TFSI$ with and without LiTFSI in Teflon-SECM cell. b) CVs in SG/TC mode at 20 mV s^{-1} of Pt WE at 5 µm from in O_2-saturated $PYR_{14}TFSI$ with and without LiTFSI in Teflon-SECM cell. The curves have not been corrected by the uncompensated resistance (iR).

4.2 ORR in TEGDME - 0.5m and 5m LiTFSI by SECM

The ORR was investigated by SECM in glyme-based electrolyte, TEGDME - 0.5m LiTFSI (0.5m) and TEGDME - 5m LiTFSI (5m). Figure 4.2.1 shows the voltammetry of two cycles in SG/TC mode at 20 mV s^{-1} with 2.00 V and 4.00 V vs. Li^+/Li as cathodic and anodic cut-off, of the GC substrate and Pt probe in the O_2-saturated 0.5m and 5m electrolytes.

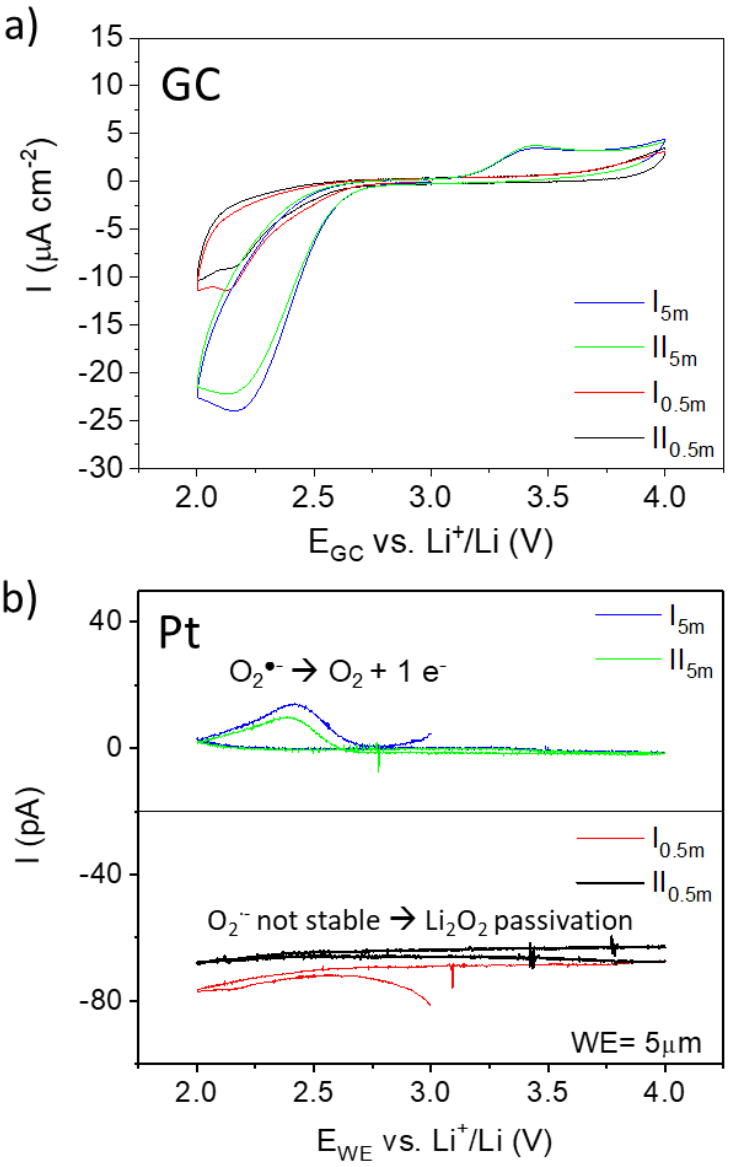

Figure 4.2.1 a) CVs in SG/TC mode at 20 mV s^{-1} of GC in O_2-saturated 0.5m and 5m in Teflon-SECM cell. b) CVs in SG/TC mode at 20 mV s^{-1} of Pt WE at 5 μm from in O_2-saturated 0.5m and 5m in Teflon-SECM cell. The curves have not been corrected by the uncompensated resistance (iR).

While in the 0.5m the Pt does not detect any species at 5 µm from the GC substrate, due to the Li_2O_2 passivation, in the SIS 5m electrolyte the $O_2^{\bullet-}$ species is stable enough to be detected by the probe and oxidized, as evinced by the anodic peak at about 2.40 V vs. Li^+/Li (blue and green curves in Figure 4.2.1b). In order to further study the $O_2^{\bullet-}$ stability and diffusion in the 5m electrolyte, the distances from the GC substrate of the Pt tip was changed up to 100 µm. Figure 4.2.2 shows that the $O_2^{\bullet-}$ species has been collected up 25 µm. The GC and the Pt were cleaned between the different steps, the latter by a quick cyclic voltammetry between 2.00 V and 4.00 V vs. Li^+/Li.

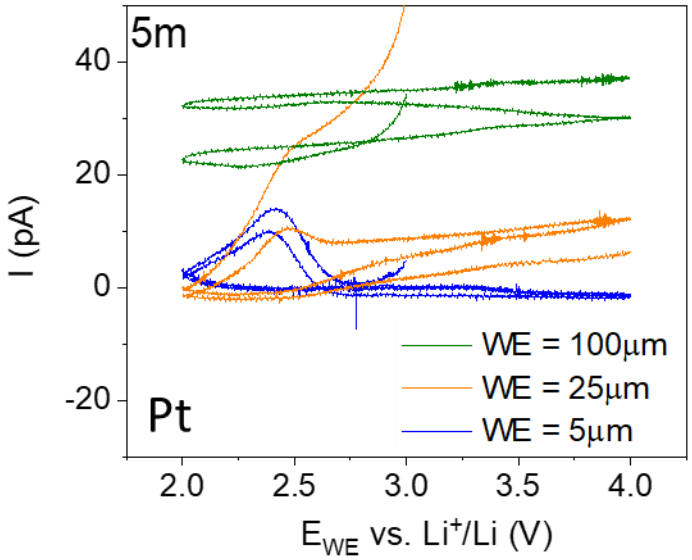

Figure 4.2.2. CVs in SG/TC mode at 20 mV s^{-1} of Pt WE at 5 µm, 25 µm and 100 µm from GC in O_2-saturated 5m electrolyte in Teflon-SECM cell. The curves have not been corrected by the uncompensated resistance (iR).

To get further insight into the ORR mechanism in the conventional salt-in-solvent 0.5m solution and in the solvent-in-salt 5m solution, a potential step (PS) in which the potential was kept constant at 2.0 V vs. Li^+/Li for 2h at was applied to the GC substrate in the Teflon-SECM cell.

Figure 4.2.3 shows the feedback curves of the Pt tip before (black curves) and after (blue curves) the O_2 reduction at constant GC potential in the two electrolytes. The two black curves collected before the electrochemical test reveal the conductive nature of the GC substrate, as reported in Paragraph 2.4, with the enhancing of the current at the tip for L close to 0.

Very interestingly, while GC becomes not-conducting after the PS in the 0.5m (Figure 4.2.3.a) and the current of the tip decreases close to the GC due to the insulator nature of Li_2O_2, in the 5m the GC keeps its conductive feature after the same test, demonstrating that the passivation is delayed because the $O_2^{\bullet-}$ is stable in the media and does not give disproportion.

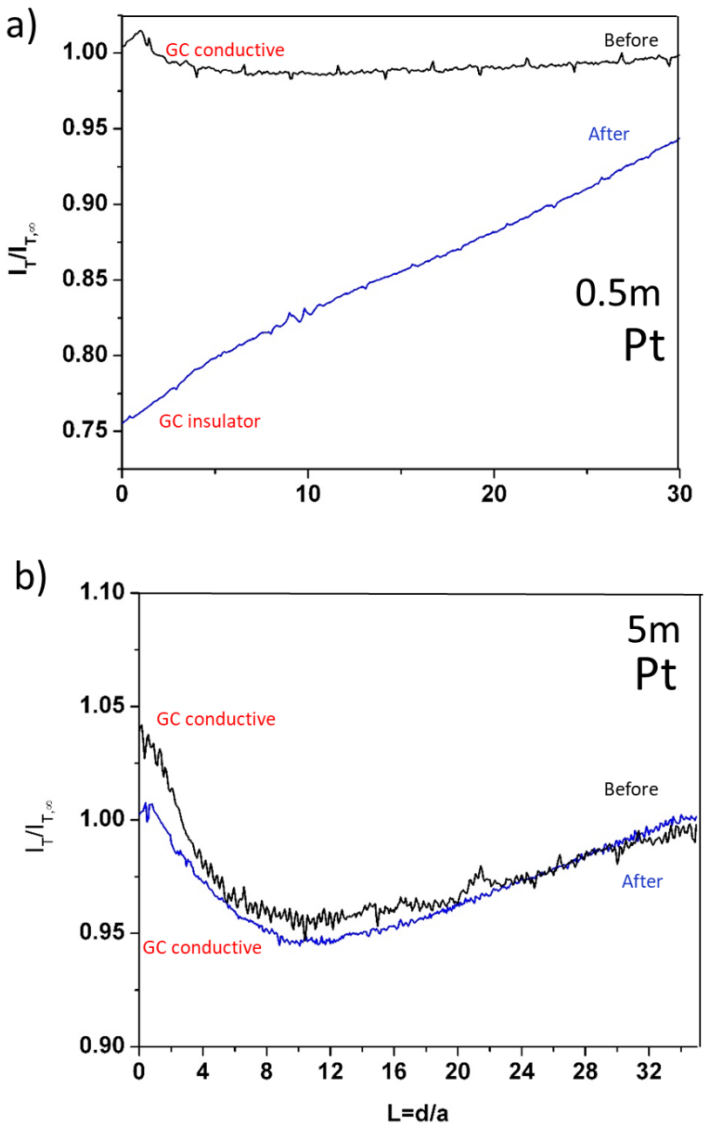

Figure 4.2.3. Approach curve in feedback mode of the Pt WE before (black line) and after (blue line) 2h-PS at 2.00 V vs. Li^+/Li constant potential applied at the GC in the O_2-saturated 0.5m (a) and 5m (b) in Teflon-SECM cell.

4.3 Electrolyte-gated transistor as probe for Li/O_2 battery

The aim of the visit in the Polytechnic of Montréal (CA) was the study of the Li_2O_2 formation and morphology in different O_2-saturated electrolyte, SIS included, by a electrolyte-gated transistor (EGT).

The reason is that any Li_2O_2 deposition on a channel of the EGT may affect the response of the current between the drain and source.

The electrolyte used was O_2-saturated 0.5m because, according to Chapter 3 and to Paragraph 4.1, is the electrolyte where the Li_2O_2 amount that deposits is expected to be the largest.

Unfortunately, with the selected electrolyte, the current between source and drain was very low since the beginning, even when the ORR was not occurring yet. This hindered any study of the current decay during the Li_2O_2 formation and was probably due to the not conducting channel.

Thus, ECTs with conducting TiO_2 or PEDOT as channel and O_2-saturated 0.5m electrolyte were also tested but no ORR was detected.

Despite the very interesting and totally novel approach of the use of a transistor to investigate the mechanism of Li/O_2 battery, the project was abandoned.

4.4 Conclusions

In Chapter 4, SECM has been used to study the Li_2O_2 formation mechanism in conventional TEGDME - 0.5m LiTFSI (0.5m) and SIS electrolyte TEGDME - 5m LiTFSI (5m).

The results obtained by the substrate generation/tip collection (SG/TC) mode demonstrate that $O_2^{\bullet-}$ quickly gives the chemical dismutation to Li_2O_2 in the 0.5m solution. On the contrary, in the 5m electrolyte the $O_2^{\bullet-}$ is stable enough and diffuses being detected in solution by the Pt-tip (WE) located up to 25 μm from the GC substrate (Figures 4.2.1-4.2.2). A similar result has been obtained with the Li^+-free IL $PYR_{14}TFSI$ (Figure 4.1.1). Furthermore, the approach curves obtained in the "feedback mode" before and after a potentiostatic step of 2h at 2.00 V vs. Li^+/Li reveals that the GC remains conductive in 5m, while it is passivated by Li_2O_2 in 0.5m electrolyte, suggesting that in SIS 5m the GC surface is free from Li_2O_2 passivation (Figure 4.2.3).

Even though the use of a electrolyte gated transistor (EGT) seems to be an innovative strategy to study the Li/O_2 battery mechanism, it did not give any interesting results for the systems on which this PhD thesis is focused on (Paragraph 4.3).

Chapter 5 The use of Poly-Ionic-Liquid in Li and Li/O_2 batteries

As previously discussed in Chapter 1, given that the intermediate species, i.e. the superoxide of the ORR, causes the degradation of electrolyte, carbon and binder in the Li/O_2 battery (47), while several approaches have been considered to hinder the dendrite growth in Li batteries.

Poly-Ionic-Liquids (PILs) are a novel class of material proposed as both binder and electrolyte in Li and LIBs (29), (59).

In Chapter 5, the use of Imidazolium-based PILs as binder for the Li/O_2 cathode (Paragraph 5.1) and as protective layer with graphene oxide (GO) on the Li surface to prevent the dendrite (Paragraph 5.2) is discussed.

The work was entirely carried out during the internship at the Helmholtz Institute Ulm (April 15th, 2018 – October 15th, 2018), under the supervisions of Prof. Stefano Passerini and Dr. Dominic Bresser.

All the results are preliminary, considering that several tests are still running.

5.1 Ionic conductivity of the LiTFSI-DEMETFSI electrolyte

As reported in Chapter 2, the electrolyte used during the internship at HIU was the concentrated LiTFSI:DEMETFSI (0.5:1). The high amount of Li salt added to the IL was selected to hinder any dissolution of the PILs in the electrolyte. Figure 5.1.1 reports the Arrhenius plot with the values of the ionic conductivity in the temperature range of 0 °C – 150 °C. The low values of about 0.10 and 0.45 mS cm^{-1} were obtain at 20 °C and 40 °C, respectively. Interestingly, no hysteresis during the heating and cooling test was observed.

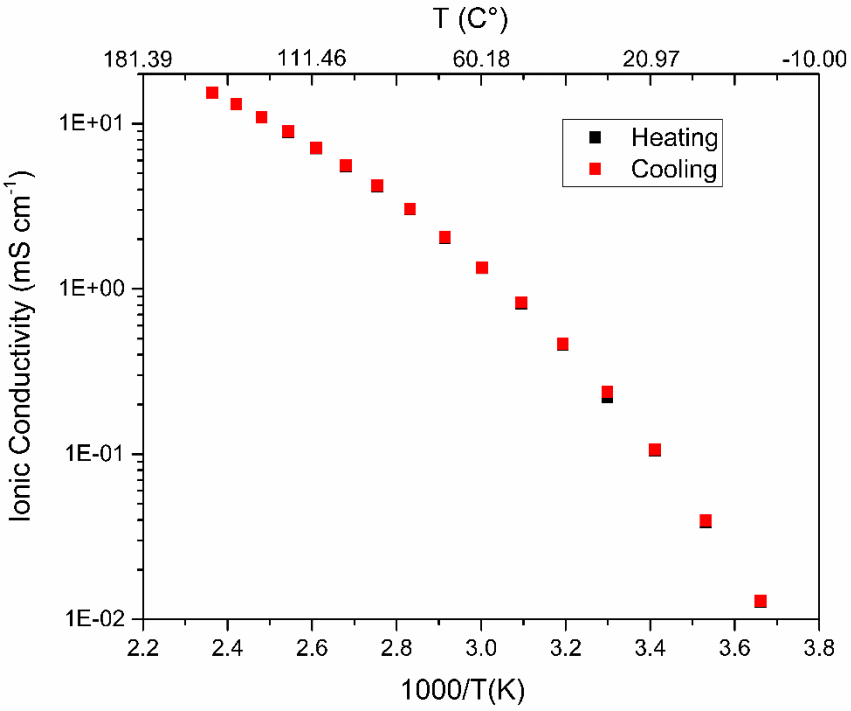

Figure 5.1.1. Arrhenius plot of the LiTFSI:DEMETFSI (0.5:1) electrolyte. The values of the ionic conductivity were obtained from 0 °C to 150 °C.

5.2 Imidazolium-based PIL as binder in Li/O_2 battery cathode

As reported in Paragraph 2.1, the copolymer C_2VImTFSI-C_{10}VImTFSI (1:1 wt.) was provided by Dr. Dominic Bresser and tested first as binder (5 % wt.) in the Super-P-based cathode. Figure 5.2.1 reports the galvanostatic cycles at 40°C of a top-meshed 2032 coin-cell Li/O_2 with the C_2VImTFSI-C_{10}VImTFSI as binder and LiTFSI:DEMETFSI electrolyte. The lower and upper voltage limit were 2.00 and 4.50 V, respectively. The battery was cycled limiting in time the discharge/charge semi-cycle (20 h, C/20) and in capacity (500 mAh g^{-1}), considering 1000 mAh g^{-1} as theoretical gravimetric capacity of the Super-P based cathode.

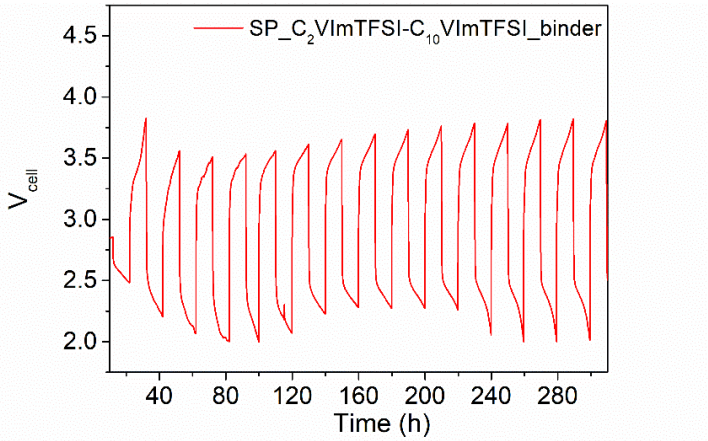

Figure 5.2.1. Cell voltage during galvanostatic discharge/charge at 40 °C and 0.024 mA cm^{-2} with 2.00 and 4.50 as voltage limit, 20 h as time limit, and 0.475 mAh cm^{-2} as capacity limit. The cathode electrode was made of Super-P (95 %wt.) and C_2VImTFSI-C_{10}VimTFSI binder (5 %wt.).

For a better understanding, considering the mass loading (Super-P) of the electrode of 0.95 mg cm^{-2}, the limited capacity was 0.475 mAh cm^{-2} and the current density was 0.024 mA cm^{-2}.

For comparison, a Li/O_2 battery with PVDF as binder is reported in Figure 5.2.2 and cycled at the same condition of Figure 5.2.1. The mass loading was 1.8 mg cm^{-2} and the areal capacity and the current density were 0.9 mAh cm^{-2} and 0.45 mA cm^{-2}, considering the specific capacity and time limit of 500 mAh g^{-1} and 20 h. According to the Figure 5.2.1, the use of C_2VImTFSI-C_{10}VimTFSI as binder in Li/O_2 cathode with the selected electrolyte allowed to cycle the battery for more than 10 times. On the contrary, the Li/O_2 battery with PVDF as binder featured high overvoltage since the beginning and the cell death occurred after only 2 cycles.

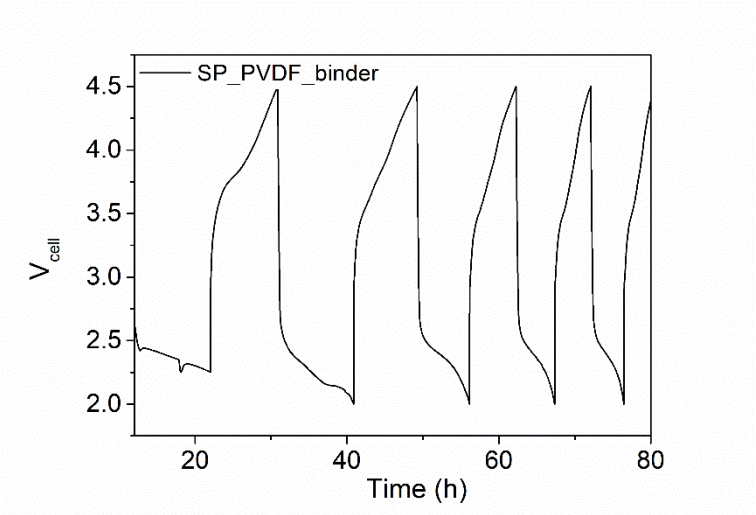

Figure 5.2.2. Cell voltage during galvanostatic discharge/charge at 40 °C and 0.45 mA cm^{-2} with 2.00 and 4.50 as voltage limit, 20 h as time limit, and 0.9 mAh cm^{-2} as capacity limit. The cathode electrode was made of Super-P (95 %wt.) and PVDF binder (5 %wt.).

As reported in Chapter 2, at HIU some crosslinked PILs where synthetized. The PILs C_2VImTFSI – (5 %wt. and 10 %wt) C_4(VIm-FSI)$_2$ w/ or w/o LiTFSI and C_2VImFSI – (5 %wt. and 10 %wt) C_4(VIm-FSI)$_2$ w/ or w/o LiTFSI unfortunately dissolved in LiTFSI:DEMETFSI (0.5:1), the chosen IL-based electrolyte.

The formation of $O_2^{\bullet-}$ and its oxidation are electrochemically reversible during the voltammetry of a GC electrode in an O_2-saturated IL like PYR_{14}TFSI that is stable to $O_2^{\bullet-}$, as already suggested in Figure 3.2.1d (103).

With the aim to investigate the stability to the superoxide $O_2^{\bullet-}$ during the ORR in a Li/O_2 battery, the solids C_2VImFSI – (5 %wt. and 10 %wt) C_4(VIm-FSI)$_2$ were dissolved in acetonitrile (ACN) 1:2 and the voltammetry at room temperature was performed. The results are reported in 5.2.3 and suggest that in both samples with 5 %wt. and 10 %wt. of C_4(VIm-FSI)$_2$ crosslinker, the $O_2^{\bullet-}$, once formed from the O_2 mono-electronic reduction (ca. 2.15 V vs. Li^+/Li), does not oxidize probably because it nucleophilically attacks the PILs, rendering the latter not suitable for the predicted application.

At the contrary, the voltammetry of the GC in ACN reveals a better stability, showing the reduction and the oxidation peaks.

The PIL C_2VImFSI – (5 %wt. and 10 %wt) C_4(VIm-FSI)$_2$ and probably also C_2VImTFSI – (5 %wt. and 10 %wt) C_4(VIm-FSI)$_2$ can be thus excluded as binder in Li/O_2 battery, considering the instability to the $O_2^{\bullet-}$.

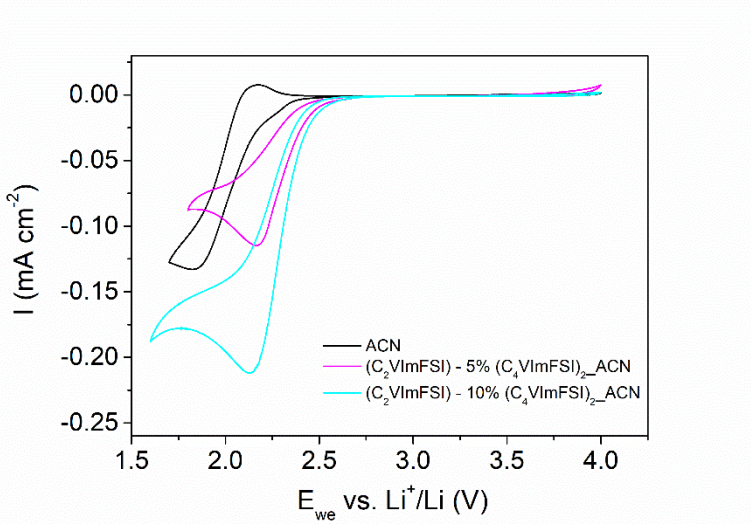

Figure 5.2.3. CVs at 10 mV sec^{-1} of a glassy carbon electrode (GC) in O_2-saturated solutions of ACN (black), and C_2VImFSI – (5 %wt. and 10 %wt) C_4(VIm-FSI)$_2$ (pink and cyan), dissolved 1:2 in ACN. The results were obtained at room temperature in dry room.

5.3 Protected layer on Li metal based on Imidazolium-PILs

As reported in Chapter 1, several strategies have been proposed in order to decrease the formation of the dendrite that dramatically affect the performance of the battery, limiting the safety of the system. In 2018 R. Dominko and coworkers published an interesting study on a protective layer on Li metal based on reduced graphene oxide, showing a free-dendrite formation during Li stripping/deposition with carbonate and ether-based electrolyte (112).

The Li electrodes with protective layer were obtained at HIU by casting an NMP-based dispersion of graphene oxide (GO) and 3 different PILs: a) C_2VImTFSI-C_{10}VimTFSI with LiTFSI added during the preparation of the

dispersion, b) C_2VIm-TFSI with 10% wt. of DVB and LiTFSI and c) C_2VIm-FSI with 10% wt. of DVB and LiTFSI.

The Li electrodes were casted by dispersions based on C_2VImTFSI-C_{10}VimTFSI and with LiTFSI featured 0.2 mg ml^{-1} of GO and 1 mg ml^{-1} (1GO_5C_2VImTFSI-C_{10}VImTFSI_LiTFSI) or 2 mg ml^{-1} (1GO_10C_2VImTFSI-C_{10}VImTFSI_LiTFSI) of copolymer.

C_2VIm-TFSI and C_2VIm-FSI with 10% wt. of DVB and LiTFSI featured 0.2 mg ml^{-1} of GO and 2 mg ml^{-1} of crosslinked (1GO_10C_2VImTFSI-DVB_LiTFSI and 1GO_10C_2VImFSI-DVB_LiTFSI).

Both symmetrical Li/Li coin cells and T-Swagelok were assembled to study the different Li interfaces at 40°C with the LiTFSI:DEMETFSI electrolyte and the beginning of the dendrite formation.

Figure 5.3.1 and Figure 5.3.2 show the overvoltage of the 2h-Li stripping/deposition at the constant 0.05 mA cm^{-2} current density of the symmetric cell with 1GO_5C_2VImTFSI-C_{10}VImTFSI_LiTFSI and 1GO_10C_2VImTFSI-C_{10}VImTFSI_LiTFSI.

Figure 5.3.3 and Figure 5.3.4 display the overvoltage with the 1GO_10C_2VImTFSI-DVB_LiTFSI and 1GO_10C_2VImFSI-DVB_LiTFSI, respectively. The experiments are still running.

Lastly, Figure 5.3.5 reports the same test with Li electrodes free from any protective layer, for comparison.

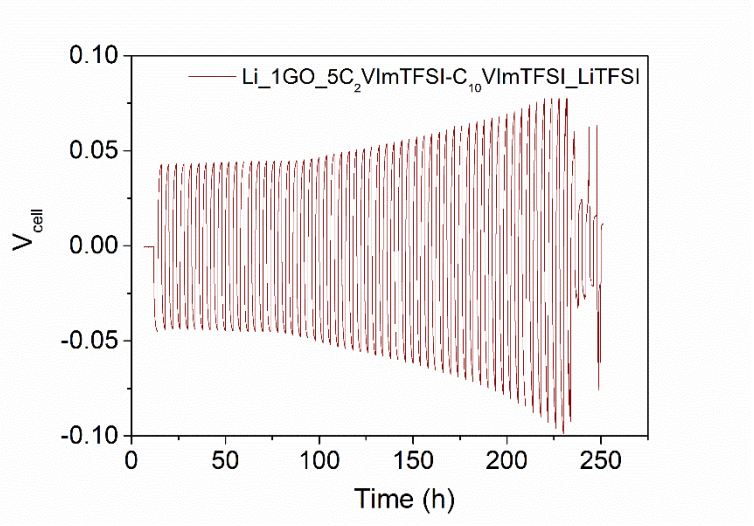

Figure 5.3.1. 2h-Li stripping/deposition at 40 °C and 0.05 mA cm^{-2} as current density of Li with 1GO_5C_2VImTFSI-C_{10}VImTFSI_LiTFSI as protective layer.

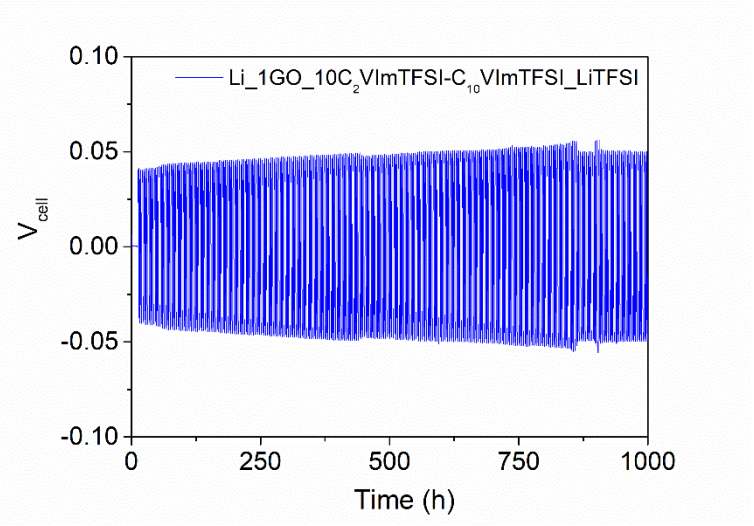

Figure 5.3.2. 2h-Li stripping/deposition at 40 °C and 0.05 mA cm^{-2} as current density of Li with 1GO_10C_2VImTFSI-C_{10}VImTFSI_LiTFSI as protective layer.

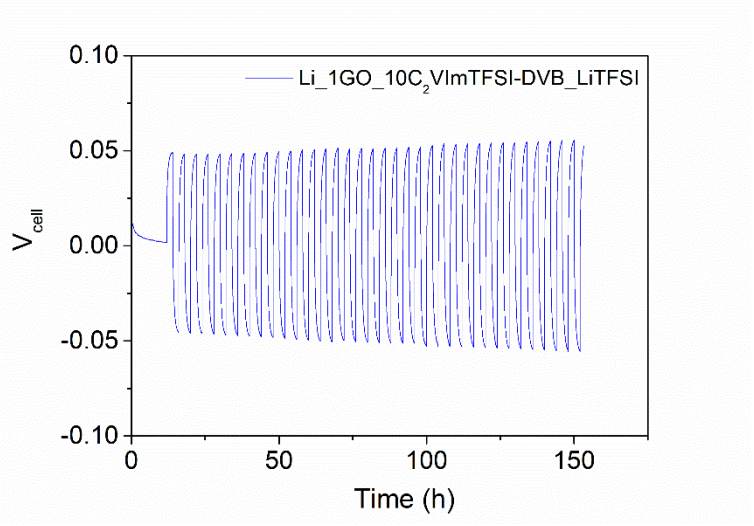

Figure 5.3.3. 2h-Li stripping/deposition at 40 °C and 0.05 mA cm^{-2} as current density of Li with 1GO_10C_2VImTFSI-DVB_LiTFSI as protective layer.

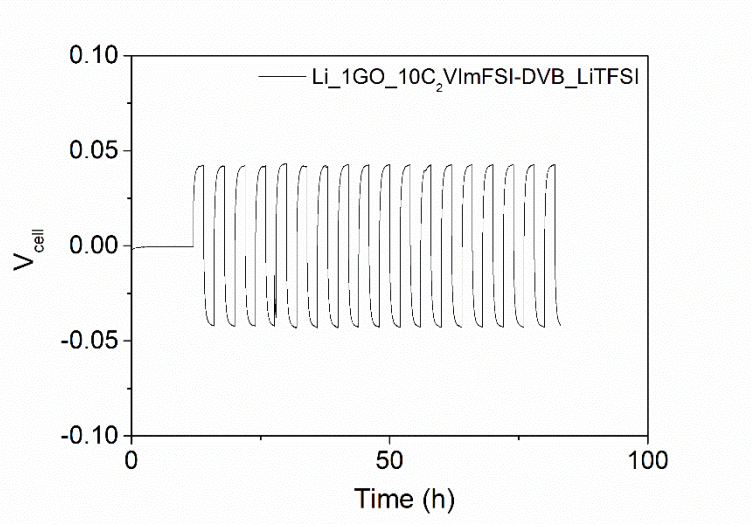

Figure 5.3.3. 2h-Li stripping/deposition at 40 °C and 0.05 mA cm^{-2} as current density of Li with 1GO_10C_2VImFSI-DVB_LiTFSI as protective layer.

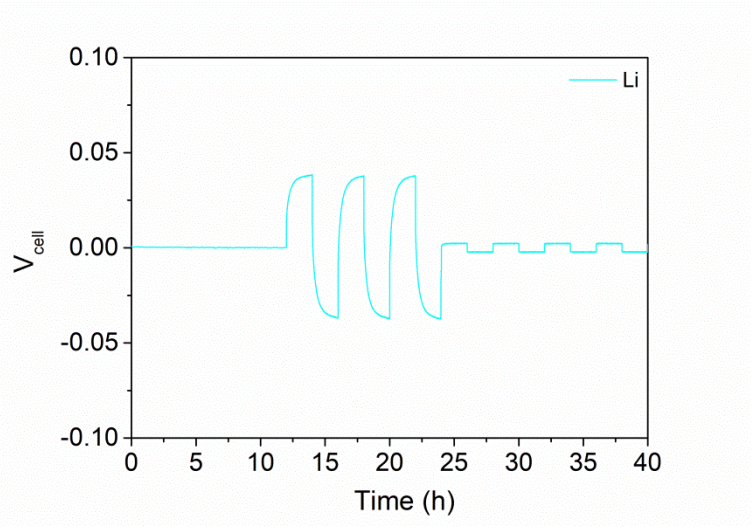

Figure 5.3.5. 2h-Li stripping/deposition at 40 °C and 0.05 mA cm^{-2} as current density of Li w/o any protective layer.

While in Figure 5.3.5, the dendrite formation starts after only few cycles, evidenced by the decreasing in the overvoltage due to the increased surface, the use of the protective layer based on PILs and GO may help to hinder the phenomena. Specifically, Figure 5.3.2 reports the 2h-Li stripping/deposition along 1000 h with a very stable interface, evidenced by a constant overvoltage, using 1GO_10C_2VImTFSI-C_{10}VImTFSI_LiTFSI as protective layer.

Furthermore, to better characterize the different Li interfaces and to study how the overvoltage is affected by the imposed current, another 2h-Li stripping deposition test at 40 °C was performed varying the current density from 0.013 mA cm^{-2} to 0.13 mA cm^{-2} (3 cycles per current). Figure 5.3.6 reports the results obtained with the Li pristine (cyan), compared to the Li with 1GO_10C_2VImTFSI-C_{10}VImTFSI_LiTFSI (blue),

1GO_10C_2VImTFSI-DVB_LiTFSI (green) and 1GO_10C_2VImFSI-DVB_LiTFSI (black).

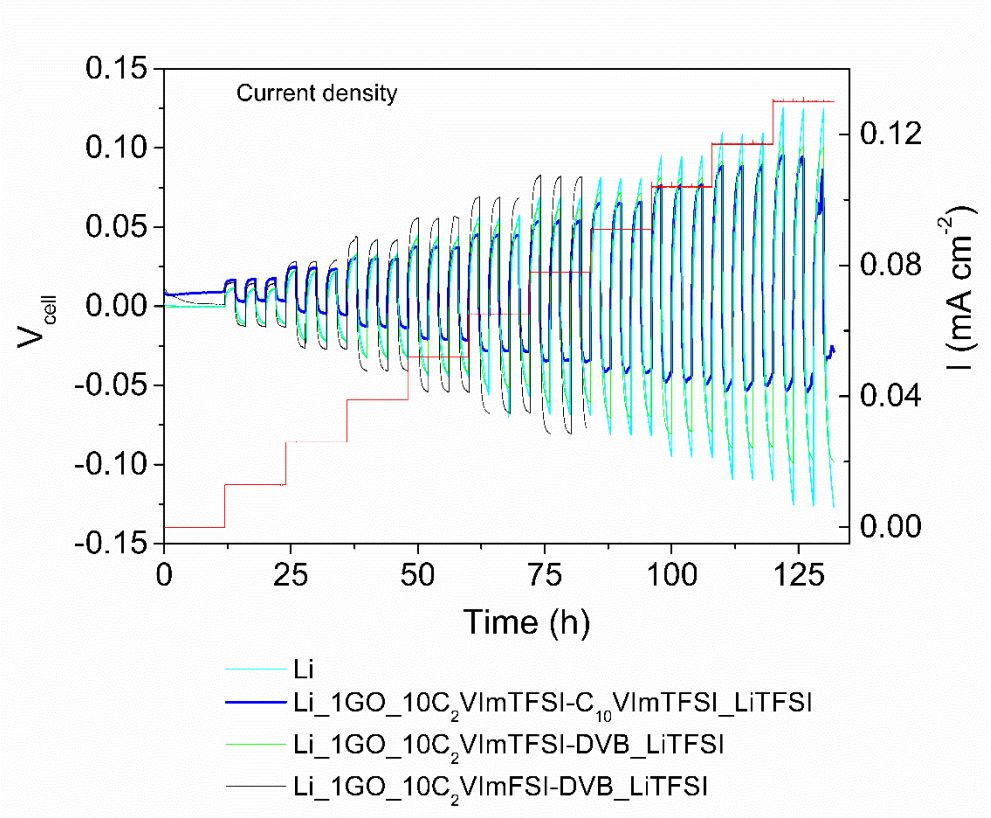

Figure 5.3.6. 2h-Li stripping/deposition at 40 °C and 0.05 mA cm^{-2} as current density of Li w/o any protective layer.

Interestingly, the overvoltages of the Li electrode protected by the 1GO_10C_2VImTFSI-C_{10}VImTFSI_LiTFSI (blue) and 1GO_10C_2VImTFSI-DVB_LiTFSI (green) have lower values than those related to the Li without any protective layer (cyan) at the highest currents (from 0.065 mA cm^{-2} to

0.13 mA cm^{-2}), while at lower currents the values are similar, except for the protection with 1GO_10C_2VImFSI-DVB_LiTFSI (black). Specifically, the V_{cell} in charge is 90 mV with 1GO_10C_2VImTFSI-C_{10}VImTFSI_LiTFSI, while it is 120 mV in the pristine Li at the highest current density of 0.13 mA cm^{-2} (30% increase). This suggests that the layer effectively protects the Li surface and probably a different mechanism of the Li reduction and oxidation with the protective layer at the highest currents occurs.

5.4 Conclusions

In Chapter 5, the use of imidazolium-based Poly-Ionic-Liquid (PIL) as binder for cathode in Li/O_2 battery and as a protective layer with the graphene oxide (GO) is presented. The results, obtained during the internship at the Helmholtz Institute of Ulm, even though are preliminary may suggest that while some of the investigated PILs like C_2VImFSI – (5 %wt. and 10 %wt) C_4(VIm-FSI)$_2$ are not suitable as binders because they probably suffer from the superoxide degradation (Figure 5.2.3), the C_2VImTFSI-C_{10}VimTFSI showed interesting cycling performance in Li/O_2 battery if used as binder (Figure 5.2.1).

Furthermore, the use of dispersions based on PILs and GO suggest that the overvoltage in symmetric Li/Li cells is lower with the use of protective layer and that the dendrite growth may be delayed with the PIL-GO layer. Anyway, further tests are required on PILs to get insight on these new and interesting materials.

Chapter 6 Semi-solid redox flow Li/O_2 battery

As previously discussed in Chapter 1, in order to increase the battery performance of both redox flow batteries (RFBs) and conventional Li/O_2 batteries (air-breathing, not flowing), the use of a flow Li/O_2 battery, where the electrolyte is fed with O_2 and acts as O_2-carrier to the cathode/electrolyte interface, has been proposed. Chapter 6 deals with the demonstration of a radically new battery concept: a semi-solid electrolyte, saturated with O_2 that can be a suitable catholyte for the flow Li/O_2 battery.

Elsevier is acknowledged for the permission to reprint some parts of the following publication:

- I Ruggeri, C Arbizzani, F Soavi, A novel concept of semi-solid, Li redox flow air (O_2) battery: a breakthrough towards high energy and power batteries, Electrochimica Acta 206(2016), 291-300. Copyright (2016).

The Electrochemical Society is acknowledged for the permission to reprint some parts of the following publication:

- F. Soavi, I. Ruggeri, C. Arbizzani, Design study of a novel, semi-solid Li/O_2 redox flow battery, ECS Transaction 72 (2016), 1-9. Copyright (2016).

6.1 A novel concept of Semi-solid, Li redox Flow Air (O_2) Battery

In this PhD thesis, for the first time, a non-aqueous, semi-solid lithium redox flow air (O_2) battery (SLRFAB), which is also the subject of an international patent (Europe, USA, Japan), has been proposed (113). The patent is being used in the spin-off called BETTERY S.R.L. (www.bettery.eu), which aim to exploit the technology.

This technology is able to combine the high energy density of Li/O_2 battery with the main features of RFBs, where the energy depends on the quantity of the electroactive species in the liquids. Furthermore, replacing solid electrodes with semi-solid slurries is demonstrated to be effective to improve battery rate response of the Li/O_2 system, maximizing the potential sites for the redox reaction.

The battery operates with a flowable O_2-saturated catholyte, based on conducting carbon particles dispersed in the non-aqueous electrolyte, which is pumped through the cell. It is a low cost catholyte, without any solubilized catalyst or redox mediator. Li metal is used as anode electrode.

The SLRFAB concept is demonstrated by low-cost commercially available materials that have been already employed in conventional Li/O_2 batteries.

ORR occurs on the solid phase of the catholyte (Figure 6.1.1) (99), limiting the electrode passivation, enhancing the Li/O_2 battery capacity and, in turn, the delivered energy.

SLRFAB thus can improve the battery performance by using a novel cell configuration. The catholyte consists of Super-P carbon black (SP) in TEGDME-LiTFSI electrolyte, saturated with O_2.

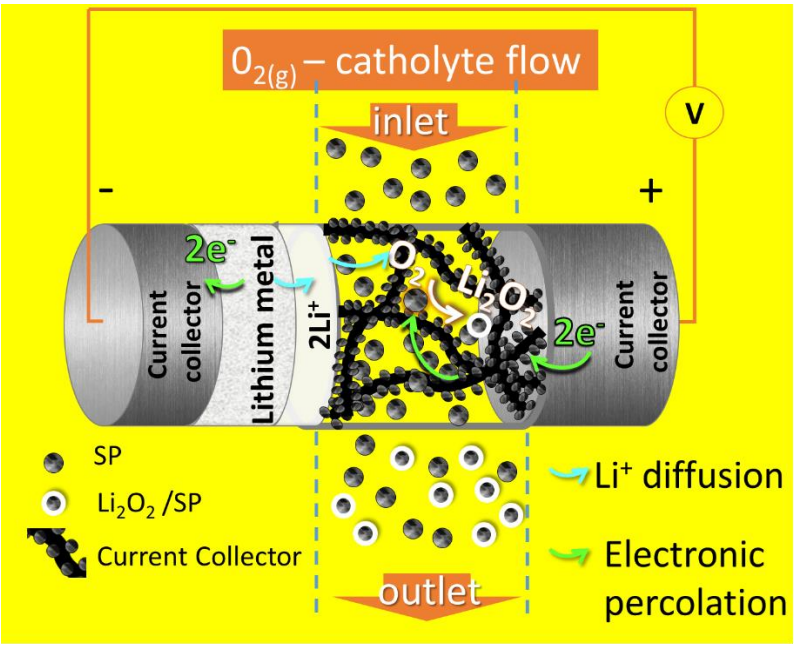

Figure 6.1.1. Scheme of the operation of SLRFAB. Reprinted and adapted from ref. (99), with permission from Elsevier.

6.1.1 Demonstration of the SLRFAB concept in the glass electrochemical cell

A first test was carried out with a 5 mL conventional electrochemical cell where the catholyte (0.5 m LiTFSI in TEGDME, 2% wt. SP, 2SP) or electrolyte (0.5 m LiTFSI in TEGDME, 0.5m) were saturated with O_2 by a continuous bubbling and mechanically stirred to simulate the flow. In order to provide/collect (depending if the discharge or the recharge is considered) the electrons to/from the liquid cathode during the battery operation, the use of a current collector is compulsory. The choice fallen on the light and low-cost carbon paper (CP), which consists of carbon fibers.

An Ag-based reference electrode was used to check the potentials of the two electrodes during battery operation.

As reported in Figure 6.1.1.1, the open circuit potential of the CP/0.5m and CP/2SP are similar, being 2.90±0.03 V vs. Li^+/Li. Once the current was applied, the CP/2SP potential was 2.70 V vs. Li^+/Li, corresponding to 300 mV higher than that of the CP/0.5m (99).

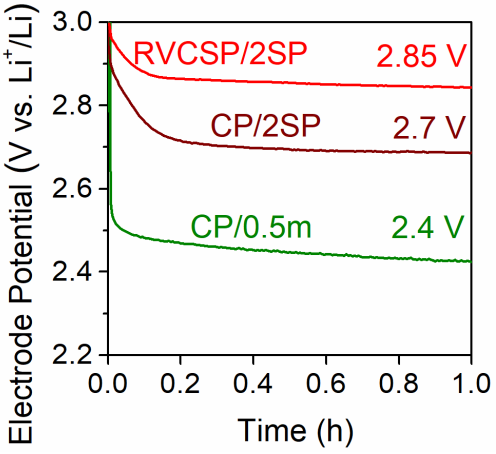

Figure 6.1.1.1. Electrode potential profiles during galvanostatic discharges at 0.25 mA cm^{-2} of CP (0.45 cm^2) in stirred, O_2-saturated 0.5m electrolyte (green line) and 2SP catholyte (wine line). The red line is the RVCSP (0.6 cm^2, 3 mg cm^{-2} of SP) potential in stirred, O_2-saturated 2SP catholyte. Reprinted from ref. (99), with permission from Elsevier.

This is probably due to the action of the percolating network in the catholyte, which enhances the reaction surface area and, thus, reduces the ohmic drops. The potential of RVCSP, which is a reticulated vitreous carbon foam (RVC) current collector which SP is deposited on, in the 2SP catholyte is also reported in Figure 6.1.1.1, featuring the lowest overpotential.

Figure 6.1.1.2 compares the potential of the CP current collector in the stirred O_2-saturated electrolyte (CP/0.5m) and catholyte (CP/2SP) under galvanostatic discharge at 0.25 mA cm^{-2} as current density.

Beside the rise of the cathode potential as already discussed and reported in Figure 6.1.1.1, the use of the 2SP semi-solid catholyte dramatically increases the discharge capacity of the Li/O_2 battery instead of the 0.5m electrolyte (i.e. without the adding of the SP carbon) (99).

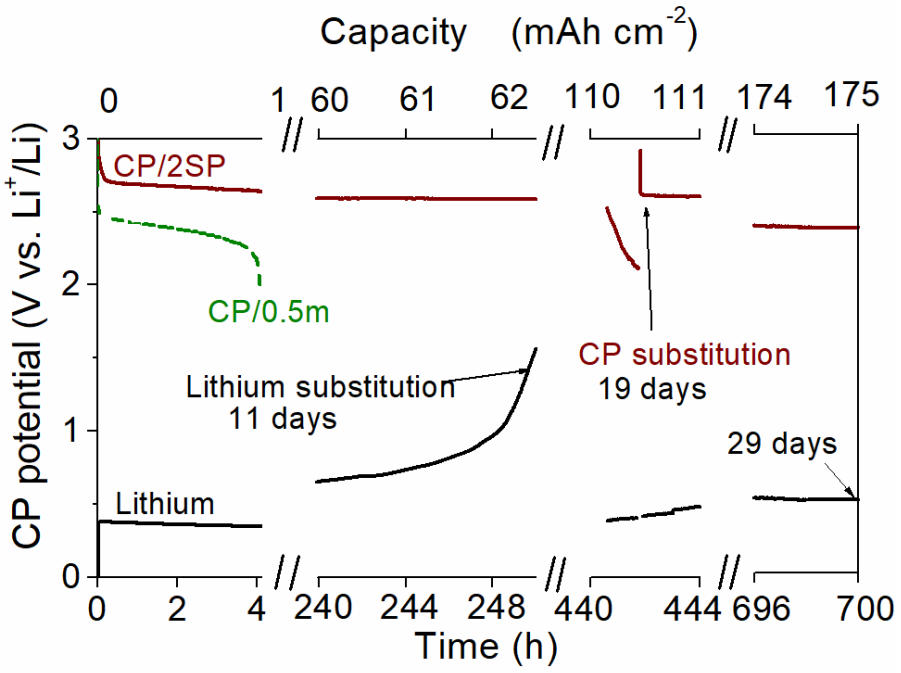

Figure 6.1.1.2. CP (0.45 cm^2) potential during galvanostatic discharge at 0.25 mA cm^{-2} of CP in conventional electrochemical cell with stirred, O_2-saturated 0.5m electrolyte (green line) or 2SP catholyte (brown line). Li potential over long term test in the cell with 2SP catholyte is also reported (black line). Reprinted from ref. (99), with permission from Elsevier.

The discharge indeed increased from 4 h (1 mAh cm^{-2}) to 11 days (66 mAh cm^{-2}), the latter being limited by the Li consumption, as shown in the Figure 6.1.1.2 by the quick rising of the Li potential (black line). Once the Li was replaced, the extending of the discharge of other 8 days was possible.

This corresponds to the unprecedented high value of the discharge capacity, being 110 mAh cm^{-2} and to the areal energy density value of 300 mWh cm^{-2}. Passivation by the Li_2O_2 discharge product on the CP occurred after 19 days because its potential reached the cut-off of 2.00 V vs. Li^+/Li.

Additional 10 days of discharge were obtained by change the used CP with a fresh one. The discharge was intentionally stopped afterwards and, in other words, the specific capacity of total SP dispersed in the catholyte (0.1 g) was limited to ca. 800 mAh g^{-1}.

The 29 days of discharge of the 2SP catholyte at 0.25 mA cm^{-2} corresponds to the outstanding value of 175 mAh cm^{-2} as areal capacity (areal energy of 490 mWh cm^{-2}).

In order to demonstrate that O_2 reduction during the discharge mainly involves the liquid electrode phase (catholyte), a CP/2SP was discharged for 45 h at 0.25 mA cm^{-2}.

The used CP was then recharged in a fresh electrolyte ($CP_{45h\text{-}d}$/0.5m) and the semi-solid 2SP catholyte was oxidized with a fresh CP current collector ($CP/2SP_{45h\text{-}d}$), as reported in Figure 6.1.1.3 (99). The recharge profile of the $CP/2SP_{45h\text{-}d}$ features a plateau at 3.50 V vs. Li^+/Li, which could be attributed to reoxidation of the discharge products previously formed in the catholyte.

The recharge lasted 25 h before to reach 3.90 V vs. Li^+/Li as positive cut-off of the CP, corresponding to 55 % of efficiency. In Figure 6.1.1.3, the charge potential of the fresh CP/2SP system (CP/2SP) is also reported.

The absence of the recharge plateau in the other two cases indicates that in the $CP/2SP_{45h\text{-}d}$, there is no CP or electrolyte anodic degradation and that the discharge primarily involves the semi-solid catholyte, where the Li_2O_2 is dispersed or dissolved.

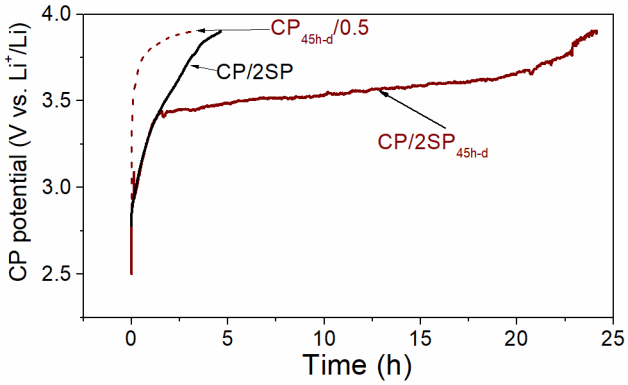

Figure 6.1.1.3. Charge profiles of fresh CP in 45 h-discharged 2SP catholyte (brown line, $CP/2SP_{45h\text{-}d}$), of the 45 h-discharged CP in fresh 0.5m electrolyte (brown dashed line, $CP_{45h\text{-}d}/0.5m$), and of a fresh CP in a fresh catholyte (black line, CP/2SP). Reprinted from ref. (99), with permission from Elsevier.

Cycling test at 0.25 mA cm^{-2} by limiting the time of the discharge to 24 h and the recharge cut-off to 4.00 V vs. Li^+/Li was also performed in the cell with CP current collector and 2SP catholyte. Figure 6.1.1.4 demonstrates that the use of a semi-solid catholyte can guarantee good Li/O_2 performance with the limited capacity of 6 mAh cm^{-2} (99).

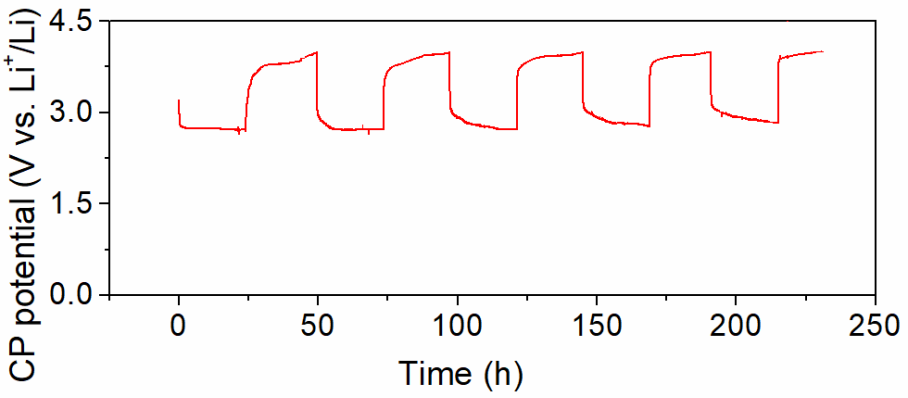

Figure 6.1.1.4. CP (0.5 cm^2) profile during galvanostatic discharge/charge at 0.25 mA cm^{-2}, with 24 h as time limit and 2.00 and 4.00 V vs Li^+/Li as cathodic and anodic cut-off in glass cell with stirred O_2-saturated 2SP catholyte. Reprinted and adapted from ref. (99), with permission from Elsevier.

Figure 6.1.1.5 reports the Nyquist plots of the CP after 19 days of discharge at 0.25 mA cm^{-2} and of the new CP in the same catholyte, the latter used for the 19-day discharge (Figure 6.1.1.2).

It is possible to notice that the impedance of the fresh CP is similar to that one of a capacitive electrode (line parallel to the imaginary axis), while the impedance of the CP used for 19 days of discharge is a Warburg type, with a typical diffusion-controlled process (108).

The impedance of the fresh CP is lower than that exhibited by the CP after discharge and the value of its capacitance, being inversely proportional to the Z_{im} at 100 mHz, is also higher than the latter (about 7 mF cm^{-2} vs. 3 mF cm^{-2}). This is due because in the CP used during 19 day of discharge, the

passivation and pore clogging by the ORR discharge products occurs, decreasing the capacitance value.

On the other hand, it is also interesting to note that the Z_{re} at the highest frequency increases only by 30 ohm cm^2 after 19 day of discharge. This reflects the good electronic contact of the carbonaceous particles dispersed in the semi-solid catholyte, the latter promoting the Li_2O_2 formation far from the current collector.

The value of the impedance of the fresh RVCSP current collector in 2SP catholyte, corresponding to the impedance before the electrochemical test reported in Figure 6.1.1.1, is also reported in the inset of Figure 6.1.1.5 (99). Here, both the Z_{re} and the Z_{im} at 100 mHz significantly reduce with respect to CP, thus indicating that electronic contact of the current collector/2SP interface can be improved using a SP-coated macroporous current collector.

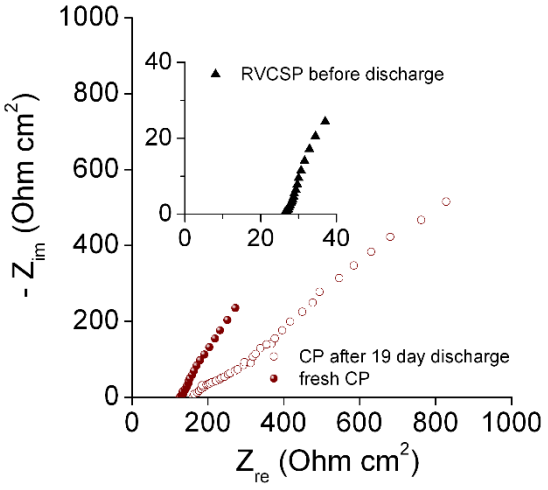

Figure 6.1.1.5. Nyquist plots of the CP current collector after 19 day of discharge at 0.25 mA cm^{-2} with 2SP catholyte (brown full dots) and of a fresh CP current collector in the same aged catholyte (brown empty dots). Nyquist plot of fresh RVCSP electrode in fresh 2SP catholyte is reported in the inset. Reprinted from ref. (99), with permission from Elsevier.

TEM of the 2SP catholyte was also collected and the relative images are shown in Figure 6.1.1.6 (99). Figure 6.1.1.6a shows the fresh 2SP catholyte, while Figure 6.1.1.6b the 2SP catholyte after 45 h of discharge and 25 h of recharge (2SP catholyte of Figure 6.1.1.3), and Figure 6.1.1.6c the 2SP catholyte after 29 days of discharge (2SP catholyte of Figure 6.1.1.2).

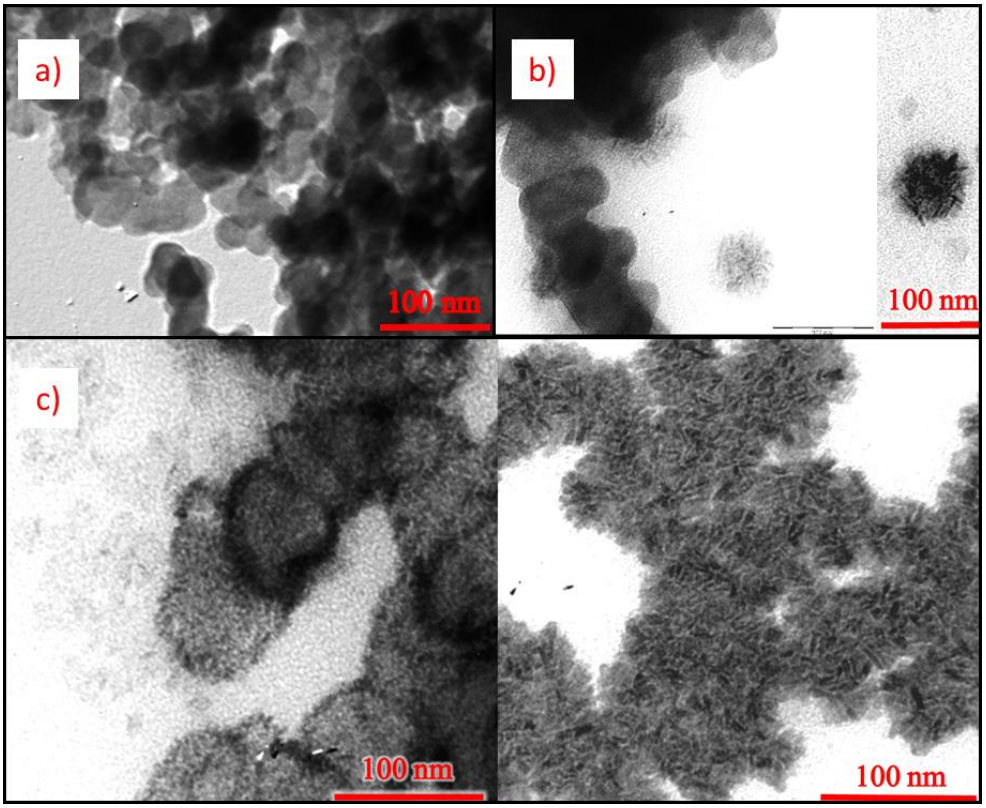

Figure 6.1.1.6. TEM images of a) the pristine 2SP catholyte b) the 2SP after 45 h discharge and 25 h charge (electrochemical results are reported in Figure 6.1.1.3) (c) 2SP after 700 h discharge (electrochemical results are reported in Figure 6.1.1.2). Reprinted and adapted from ref. (99), with permission from Elsevier.

According to Figure 6.1.1.6a, 2SP catholyte is made of SP particles with a diameter of ca. 45 nm that are well connected each other to form a percolating network that ensures the battery operation. Solid products of the discharge can be both deposited on the SP particles and dispersed in the liquid. Furthermore, the morphology of the discharge products is strongly affected by the depth of discharge. Indeed, in Figure 6.1.1.6b, related to 2SP after 45 h of discharge and 25 h of recharge, an amorphous film covers part

of the carbon network, along with small needles with 5 nm in length and 1 nm in thickness that cover the SP particles. Flake-shaped aggregates of carbon particles with some discharge products are also present and not connected to the carbon, as shown on the right side of the Figure 6.1.1.6b.

The amount of these flakes-shape aggregates increases in the catholyte used in the 29 days of discharge, as reported in Figure 6.1.1.6c, where the needles grow to give connected “sea urchin”-like structures.

The nature of the discharge products in the 2SP catholyte was investigated by several techniques, like FTIR, micro Raman, and XRD analyses.

Figure 6.1.1.7 compares the FTIR and micro Raman results of the fresh and after the discharge of 29 days 2SP catholyte (Figure 6.1.1.2) (99).

FTIR bands are similar before and after discharge, except for a small increase of the absorption band at 3500 cm^{-1} and 1600 cm^{-1} in the cycled 2SP that may be related to alcoholic moieties for the electrolyte degradation (Figure 6.1.1.7a). Interestingly, Raman analysis reveals a wide band at 800-900 cm^{-1} in the cycled 2SP that is related to the peroxy O-O vibration.

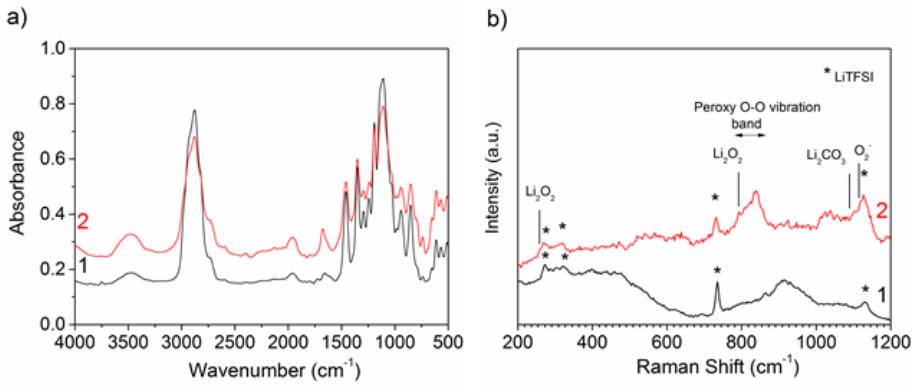

Figure 6.1.1.7. a) FTIR and b) Raman spectra of the 2SP catholyte before (black line) and after (red line) 700 h discharge at 0.25 mA cm^{-2} (Figure 6.1.1.2). Reprinted from ref. (99), with permission from Elsevier.

XRD analysis did not evince different crystalline phases in the cycled catholyte (red line) respect to that of the fresh one (black line) (Figure 6.1.1.8a).

Figure 6.1.1.8b reports the XRD patterns of the pristine CP (black line), after 19 day discharge (red line) (used in Figure 6.1.1.2) and after 45h discharge and 3.5h recharge (blue line) (used in Figure 6.1.1.3) (99). As evinced, there is a formation of a Li_2O_2 passivation layer on CP current collector only after 19 day discharge in the Li/O_2 cell with the semi-solid catholyte. Some traces of LiOH are also detected, possibly formed by reaction with the moisture (the cell is not completely hermetically sealed) after prolonged cycling (red line).

However, it is generally accepted that the product of the ORR at carbon electrodes, like SP, in TEGDME-based electrolytes, is mainly Li_2O_2.

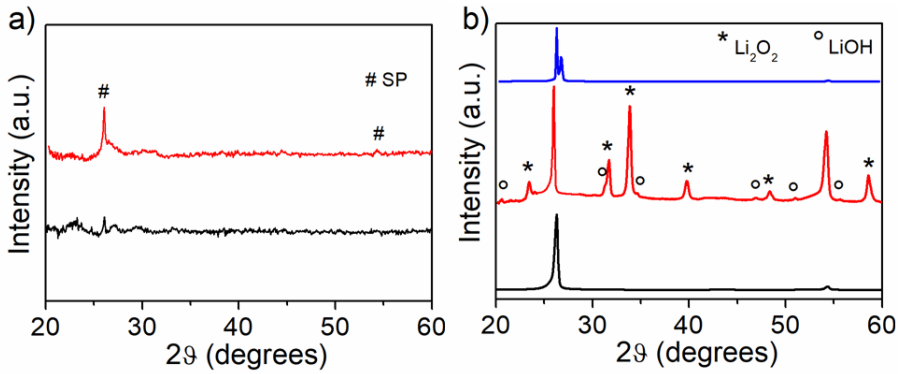

Figure 6.1.1.8. XRD spectra of a) the 2SP catholyte before (black line) and after (red line) 700 h-discharge at 0.25 mA cm^{-2} (Figure 6.1.1.2); b) the CP current collector before (black line), after 19 day discharge at 0.25 mA cm^{-2} and after 45h-discharge in the 2SP catholyte and 3.5h-richarge in 0.5m electrolyte at 0.25 mA cm^{-2}. Reprinted from ref (99), with permission from Elsevier.

The needles shown by the TEM are here assumed to be Li_2O_2 crystals (Figure 6.1.1.6b-6.1.1.6c). It is worth noting that the morphology of these particles is different from the large toroidal crystals observed in conventional Li/O_2 batteries based on the same components (114), (115).

The not-stationary condition, considering that the catholyte was stirred, and the very large surface area drives the occurrence of the Li_2O_2 nucleation, rather than the growth.

The above results suggest that ORR occurs on the surface of the solid phase in the catholyte. The CP current collector passivation cannot be entirely suppressed, but can be dramatically delayed with the use of the semi-solid catholyte. The percolating network ensures the electric contact to oxidize the Li_2O_2 dissolved/dispersed in the catholyte.

SLRFAB would feature a discharge capacity determined by the passivation of the carbon dispersed in the catholyte. Indeed, the limit of the diffusion of the O_2 through the interface, which restrains the current density in the conventional air-breathing Li/O_2 batteries, here is surpassed by the direct O_2 bubbling in the liquid.

6.1.2 Demonstration of the SLRFAB concept in flow cell

In this PhD thesis, the SLRFAB concept with the flowing catholyte was also demonstrated with a completely different cell configuration.

A macroporous current collector was chosen for the fast flow of the catholyte, which is essential when high discharge rates and viscous catholyte are taken in consideration. RVC (reticulated vitreous carbon foam, Chapter 2) was thus used as current collector and coated with SP to increase the electronic contact with the same carbon particles dispersed in the catholyte (labelled RVCSP). SEM images of RVCSP are reported in Figure 6.1.2.1 (99).

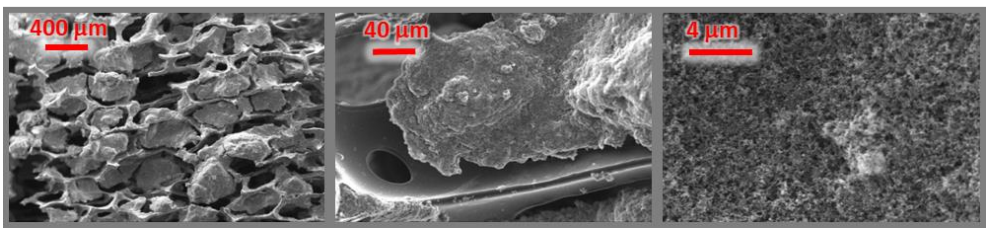

Figure 6.1.2.1. SEM images of the RVCSP current collector for the SLRFAB flow prototype. Reprinted and adapted from ref. (99), with permission from Elsevier.

Thanks to the increasing of the specific surface area obtained with the carbon coating, the ohmic losses were decreased in the cell with the 2SP catholyte and RVCSP as current collector.

Indeed, this increased the discharge RVSP potential, being 2.85 V vs. Li^+/Li at 0.25 mA cm^{-2} as already reported in Figure 6.1.1.1 and improved the impedance respect to CP, as already reported in Figure 6.1.1.5.

RVCSP was thus used to assemble the SLRFAB cell, which is drafted in Figure 6.1.2.2 (99). The cell core is made up of Li anode, a separator and the RVCSP cathode current collector. The catholyte is fed with O_2 (g) and flow in the cell thanks to a peristaltic pump. For basic studies, the reference electrode that crossed the catholyte flow was also used in order to get insight the electrodes value.

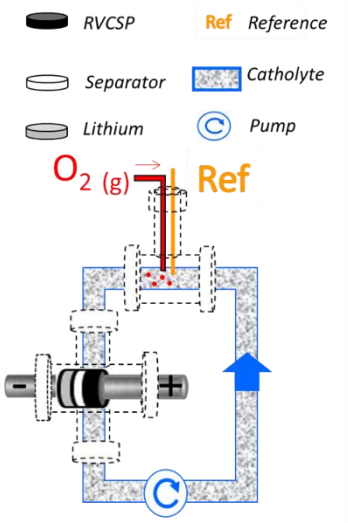

Figure 6.1.2.2. Scheme of the SLRFAB where the catholyte is flowed thanks to the peristaltic pump. Reprinted and adapted from ref. (99), with permission from Elsevier.

As already reported by Monaco et al., that studied an IL-based O_2-saturated electrolyte in a flow Li/O_2 battery, when the electrolyte was flowing in the cell the delivered energy and the applied current were higher than those obtained in the static condition, i.e. without any electrolyte flow. This result was justified because the O_2 mass transport was optimized by the electrolyte flow using a novel flow-cell concept (77).

Likewise, in order to understand how the flow rate affects the SLRFAB performance, a first electrochemical test was performed under different flow rates. Figure 6.1.2.3 reports the SLRFAB with 2SP as O_2-saturated catholyte both cell voltage and electrode potentials over discharges under different flow rates of the catholyte (expressed in pump rate) (116).

Galvanostatic discharge was carried out with a capacity cut-off of 2.6 mAh cm^{-2} and cathode potential cut-off of 2.00 V vs. Li^+/Li. Each discharge step was followed by 1h-recharge at 0.5 mA cm^{-2}. The Figure shows that at 0.5 mA cm^{-2} and without any catholyte flow, the V_{cell} has not a plateau and the cell areal capacity (Q_{cell}) was only 0.2 mAh cm^{-2} (black line). V_{cell} and Q_{cell} increased with the flow rate, reaching the Q_{cell} limit at 200 rpm as pump rate (red line) (corresponding to a catholyte flow of ca. 170 mL min^{-1}), demonstrating that the overpotentials related to O_2 mass transport are optimized under dynamic conditions.

The SLRFAB lab-scale prototype was thus employed with the 2SP catholyte for further investigations, once have determined the best kinetics ORR condition at 200 rpm as pump rate.

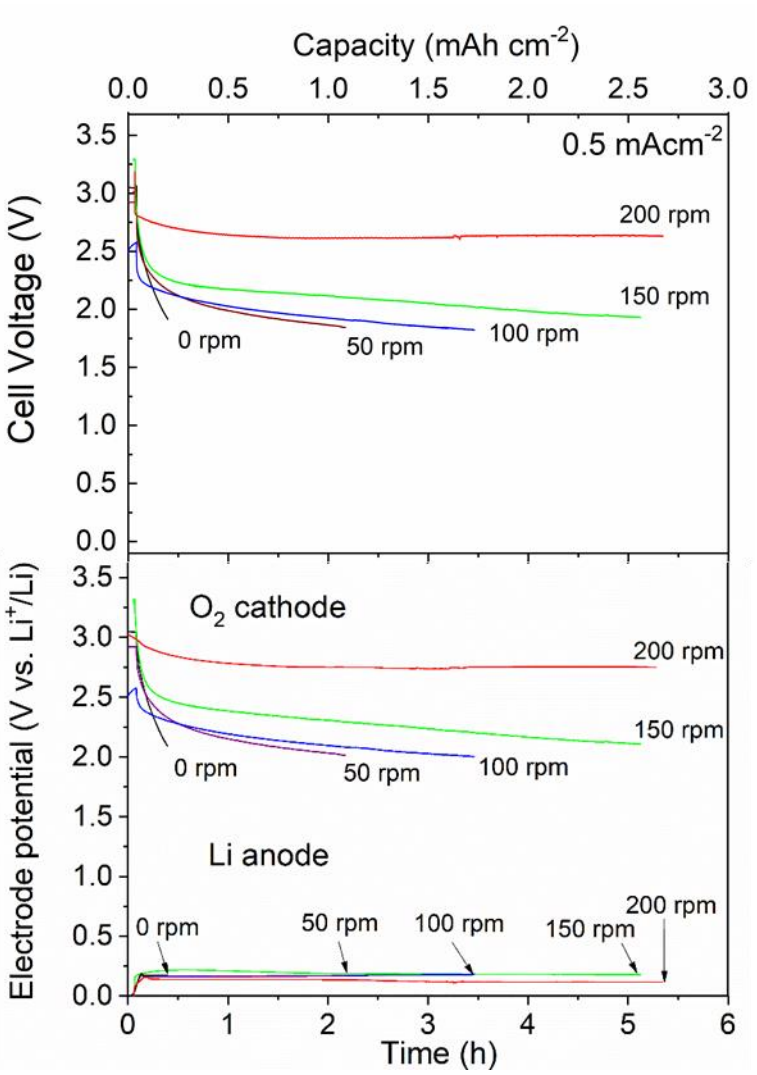

Figure 6.1.2.3. SLRFAB cell voltage and electrode potential during galvanostatic discharge at 0.5 mA cm^{-2} and at different peristaltic pump rotation (0-200 rpm). Capacity and RVCSP cathodic cut-off were 2.6 mAh cm^{-2} and 2.00 V vs Li^+/Li, respectively. Reprinted and adapted from ref. (116), with permission from The Electrochemical Society. Copyright 2016.

The high discharge capacity of the SLRFAB with the use of a semi-solid catholyte enabled long polarization tests.

A repetition of 1h-discharge steps at current densities ranging from 0.05 mA cm^{-2} to 2.75 mA cm^{-2}, with 0.05 mA cm^{-2} as step, was thus performed in the SLRFAB with 2SP O_2-saturated catholyte. The cathodic RVCSP potential cut-off was 2.00 V vs. Li^+/Li and the pump rate was fixed to 200 rpm.

Figure 6.1.2.4a shows the electrode potentials of RVCSP and Li (V_{cath} and V_{an}) and cell voltage (V_{cell}) during the consecutive 1h-discharge steps (99).

Notably, the RVCSP cathode featured a high potential of 2.90 V vs. Li^+/Li at 0.05 mA cm^{-2}, which decreased only by 10%, once 3.00 mA cm^{-2} was reached.

The cell voltage in SLRFAB was not affected by the cathode side, catholyte included but only by the Li. Li overpotential was indeed 1.00 V vs. Li^+/Li after 40h discharge, probably due to its depletion, causing the decreasing of the V_{cell}.

A second test concerned the repetition of consecutive 1h-discharge and 1h-recharge steps from 0.25 mA cm^{-2} up to 4.00 mA cm^{-2}, with 0.25 mA cm^{-2} as step, was then performed. The cathode potential cut-offs were 2.00 V vs. Li^+/Li and 3.70 V vs. Li^+/Li, during the discharge and recharge, respectively (99).

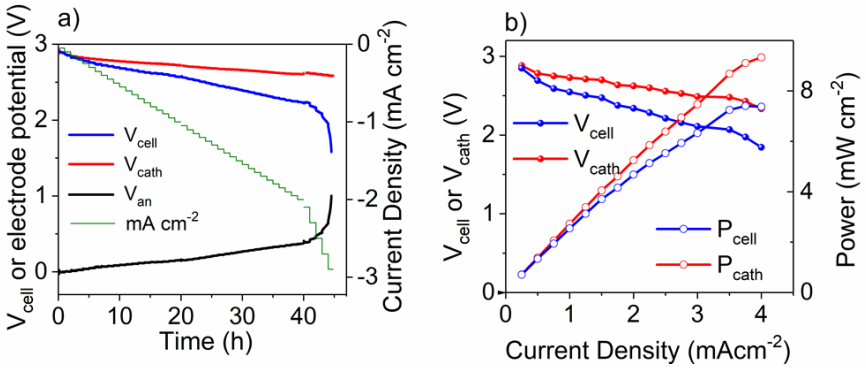

Figure 6.1.2.4. a) Potentials of RVCSP cathode (V_{cath}), Li anode (V_{an}) and cell voltage (V_{cell}) during 1h-discharge steps from 0.05 mA cm^{-2} up to 2.75 mA cm^{-2}; b) V_{cath}, V_{cell}, P_{cath} and P_{cell} vs. currents during 1h-discharge and recharge steps from 0.25 mA cm^{-2} up to 4 mA cm^{-2}. Reprinted and adapted from ref. (99), with permission from Elsevier.

The decrease of the step length and the introduction of the recharge contributed to hinder the Li depletion. Figure 6.1.2.4b shows the related polarization curve, i.e. the value of power values vs. the current density (mA cm^{-2}). V_{cell} or V_{cath} are also reported (blue and red line with solid dots). The power values (P_{cell} or P_{cath}), expressed in mW cm^{-2}, were obtained by multiply the V_{cell} or V_{cath} with the current density (blue and red line with empty dots).

The highest values obtained at 4.00 mA cm^{-2} were 10 mW cm^{-2} and P_{cell} of 7.5 mW cm^{-2}.

According to Figure 6.1.2.4b, it is also interesting to note that V_{cath} did not significantly change up to 3.00 mA cm^{-2}, decreasing from 2.90 to 2.50 V vs. Li^+/Li. However, at higher currents, the O_2-diffusion limitation caused a 20% potential drop and the V_{cath} reached 2.30 V vs. Li^+/Li at 4.00 mA cm^{-2}.

While the O_2-diffusion can be improved by increasing the flow rate, the V_{an} mainly limits the cell voltage of the SLRFAB: at 4 mA cm^{-2}, V_{cell} was indeed 1.84 V, almost 500 mV below the V_{cath} value.

The Nyquist plots reported in Figure 6.1.2.5, obtained during the 1h-discharge and 1h-recharge test from 0.25 mA cm^{-2} up to 4 mA cm^{-2}, also demonstrate that Li is the electrode that mainly contributes to total cell impedance that increases over cycling (99). The Li anode impedance increased probably because the SEI was not optimized and the O_2 can cross the separator giving the O_2 crossover, considering that the separator was only made of glass fiber.

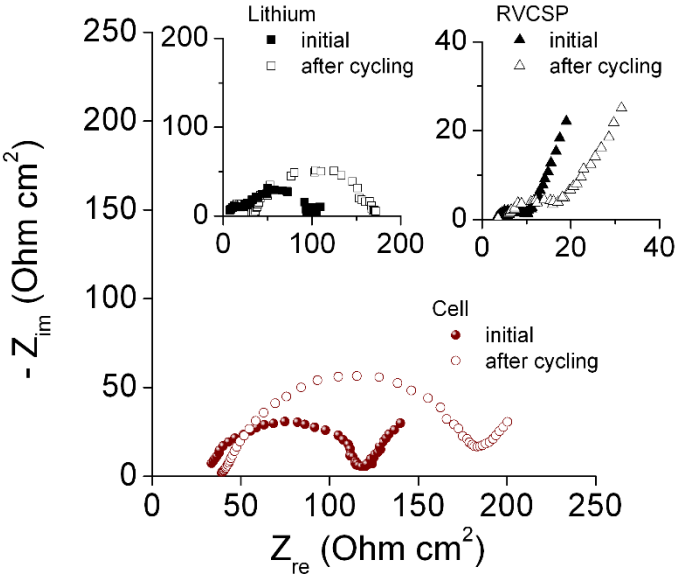

Figure 6.1.2.5. Nyquist plots of the SLRFAB cell before and after repeated 1h-discharge and recharge steps at different current densities (2-electrode mode). The insets report the Li and RVCSP Nyquist plots (3-electrode mode). Reprinted from ref. (99), with permission from Elsevier.

Figure 6.1.2.6 reports the flow SLRFAB cycling test at 1.25 mA cm^{-2} by limiting the time of the discharge to 5 h and the anodic cut-off to 3.70 V vs. Li^+/Li during the recharge, with RVCSP as current collector, 2SP as catholyte and Li as anode. The use of the 2SP catholyte can thus allow to cycle the Li/O_2 battery at outstanding currents and very high capacity (6.25 mAh cm^{-2}). While the V_{cath} was high at about 2.70 V vs. Li^+/Li, the V_{an} potential was 0.20 V vs. Li^+/Li, a value that drammatically affects the V_{cell}, being 2.50 V. Furthermore, during the Li plating, i.e. the battery recharge, the potential was not stable but decreased over time and reached the value of – 2.00 V vs. Li^+/Li during the 6^{th} recharge. Once again, these results suggest that the Li interface is not stable in the SLRFAB.

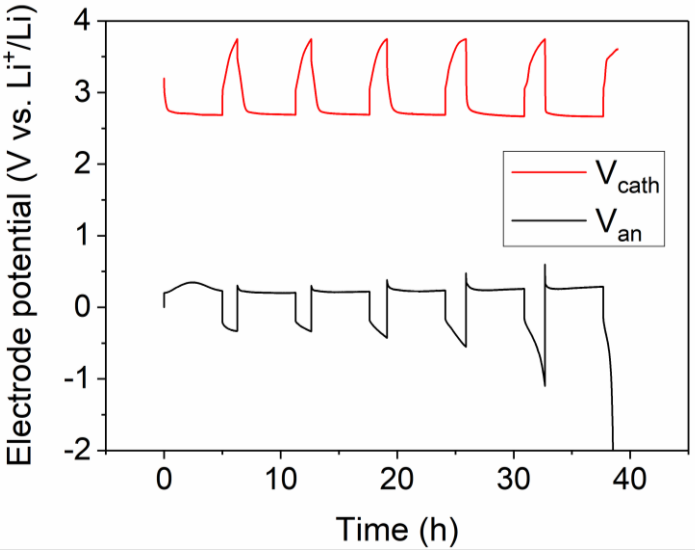

Figure 6.1.2.6. RVCSP (V_{cath}) and Li (V_{an}) profile during galvanostatic discharge/charge at 1.25 mA cm^{-2}, with 5 h as time limit and 2.00 and 3.70 V vs Li^+/Li as cathodic and anodic cut-off in SLRFAB flow cell, with 2SP O_2-saturated catholyte.

6.2 Conclusions

Chapter 6 thus demonstrates the concept of semi-solid flow Li/O_2 battery (SLRFAB) in simulated and real flow conditions, as reported in Paragraph 6.1.1 and 6.1.2, respectively. The ORR mainly occurs on a single particle dispersed in the O_2-saturated carbon-based catholyte, alleviating the fast clogging of the cathode current collector. Moreover, the percolating network given by the carbon particles in the catholyte increases the ORR active sites, decreasing the overpotential and increasing the current density. The concept has been demonstrated with the catholyte based on 2% wt. Super-P in 0.5 m LiTFSI in TEGDME (2SP). The discharge areal capacity of 175 mAh cm^{-2}, obtained in the stirred catholyte, is an outstanding value never reported in conventional Li/O_2 cathode. Additionally, in the flow SLRFAB prototype, the use of the semi-solid catholyte has enabled high potential at high discharge current density, being up to 4 mA cm^{-2}. The results also suggest that the SLRFAB cell voltage is affected by the Li anode overpotential that increased with the current (Figure 6.1.2.4, 6.1.2.5 and Figure 6.1.2.6). The cathode (current collector) featured instead high potential value thanks to the use of the catholyte and the optimized O_2 mass transport by the flow (Figure 6.1.2.3).

Chapter 7 Simulation of the SLRFAB performance

Chapter 7 concerns about the practical and projected performance of the SLRFAB (flow cell configuration) with regard to specific energy (Wh kg^{-1}), energy density (Wh L^{-1}) and power (W kg^{-1}, W L^{-1}). The results of the study derive from some galvanostatic discharges at different flow rate (Figure 6.1.2.3) and current densities. Projections of the SLRFAB performance have considered the Li/catholyte mass ratio, Li and cathode current collector thicknesses and the amount of carbon dispersed in the semi-solid catholyte.

7.1 Projected performance of the lab-scale flow SLRFAB

As already introduced in Paragraph 1.8, the use of O_2-catholyte, i.e. the saturated electrolyte which carries the cathodic active species, is a valuable strategy to develop batteries that are not limited by the O_2-mass transport, which is the main drawback of conventional air-breathing Li/O_2 and by any solubility issues of the active material. In the O_2-saturated electrolyte, indeed, the amount of the active species dissolved in the liquid is constant as the O_2 comes continuously from outside. The flow of the O_2-catholyte then optimizes the mass transport of the active species from the bulk of the electrolyte to the electrode/electrolyte interface. This allows an unceasing concentration gradient, and thus, if the passivation process is awhile neglected, a constant ORR kinetics at the interface.

The optimization of the O_2 diffusion occurs once the peristaltic pump rate is 200 rpm in the lab-prototype flow SLRFAB, as already reported in Paragraph 6.1.2 and Figure 6.1.2.3. Furthermore, the use of a semi-solid catholyte dramatically increases the capacity of the flow Li/O_2 battery and the synergic effect of the percolating network combined to the constant O_2 content in the catholyte render the SLRFAB voltage being mainly affected by the Li anode (Chapter 6).

Composition and features of the Li anode employed in the lab-scale SLRFAB prototype used in Paragraph 6.1.2, normalized to 1 cm^2 as surface, are thus reported in Table 7.1.1, together with the 2SP catholyte and the RVC current collector features (116).

Table 7.1.1. Composition and performance of the SLRFAB lab-scale prototype and of the cell with balanced Li-to-catholyte mass ratio (symbols are explained in the main text).

Component		Unit	Lab-scale SLRFAB	Balanced SLRFAB
Li	t_{Li}	cm	0.12	
	d_{Li}	g cm^{-3}	0.53	
	m_{Li}	mg cm^{-2}	64	
	Area	cm^{-2}	1	
	$Q°_{Li}$	mAh g^{-1}	3860	
	Q_{Li}	mAh cm^{-2}	200	
Catholyte	$Q°_{SP}$	mAh g^{-1}	3500	
	% SP	%	2	
	$V_{catholyte}$	cm^3	30	2.77
	m_{SP}	g	0.6	0.057
	$m_{catholyte}$	g	30	2.8
	$Q_{catholyte}$	mAh	2100	200
Current Collector	t_{cc}	cm	0.5	0.5
	m_{cc}	g	0.02	0.05
	V_{cc}	cm^3	0.19	0.5
Cell	E_{areal}	mWh cm^{-2}	555	
	P_{areal}	mWcm^{-2}	6.5	

One can easily understand that Li and catholyte are not mass balanced in the prototype and that the cell discharge capacity (Q_{cell}) cannot be higher than the Li discharge capacity (Q_{Li}), i.e 200 mAh cm^{-2}.

Indeed, in the SLRFAB lab-scale cell, the anode electrode is made up of 4 Li disks, each having 300 μm as thickness (total t_{Li} 1200 μm). The areal loading can be thus calculated being 64 mg cm^{-2} (m_{Li}), considering the Li density (d_{Li}) of 0.53 g cm^{-3}.

The Li areal capacity available for cell discharge (Q_{Li}) is thus 200 mAh cm^{-2}, since that the theoretical specific capacity of Li ($Q°_{Li}$) is 3860 mAh g^{-1} and that ca. 80% is available for discharge (the rest has been supposed to be used for secondary reactions and to form the SEI) (Equation 13).

$$Q_{Li} = t_{Li} \cdot Q_{Li}° \cdot d_{Li} \cdot 0.8 \quad (13)$$

Furthermore, the catholyte used in the prototype has a volume of 30 mL ($V_{catholyte}$) with 2% wt. of SP. The 2SP catholyte (0.5m + 2% wt. of SP) has a density ($d_{catholyte}$) of ca. 1 g mL^{-1} and thus the catholyte mass ($m_{catholyte}$) is ca. 30 g.

Considering then that has been reported that SP carbon can provide in Li/O_2 battery a discharge capacity ($Q°_{SP}$) of 3500 mAh g^{-1}, the fully discharge of the SP in the catholyte (being 600 mg) results in 2100 mAh (116). This value ($Q_{catholyte}$) is, as already introduced, 10 times higher than the Q_{Li}, causing a not proper cell balancing, as reported in Table 7.1.1. However, it is also worth to noting that the Q_{cell} of 200 mAh is much higher than that obtained with the conventional Li/O_2 cells (116).

Figure 7.1.1 reports the cell voltage (V_{cell}) and electrode potential profiles (V_{cath} and V_{an}) of SLRFAB discharge with 2.6 mAh cm^{-2} and 2.00 V vs. Li^+/Li as capacity and time limit (116). The pump rate was 200 rpm and the current densities ranged from 1.0 mA cm^{-2} to 4.0 mA cm^{-2}, with 0.5 mA cm^{-2} as step. After each discharge, a recharge at 0.5 mA cm^{-2} limited by 2.6 mAh cm^{-2} followed.

As expected, the overpotentials increase with current density. Anode and cathode overpotentials likewise contribute to the V_{cell} up to 3.0 mA cm^{-2}.

Above this value, Li is the electrode that mainly affects V_{cell} and limits cell capacity, probably due to the low diffusion of the Li^+ ions in the bulk electrolyte and/or across the solid electrolyte interface (SEI), as already suggested by the EIS reported in Figure 6.1.2.5.

This test demonstrates that at high flow rate (ca. 145 ml min^{-1}) and current density (3 - 4 mA cm^{-2}), in the flow SLRFAB, the cell performance are affected by Li anode overpotential.

Based on the experimental results reported in both Figure 6.1.2.3 and Figure 7.1.1, the following practical and projected performance of the SLRFAB cell (always normalized to 1 cm^2 of Li) can be predicted.

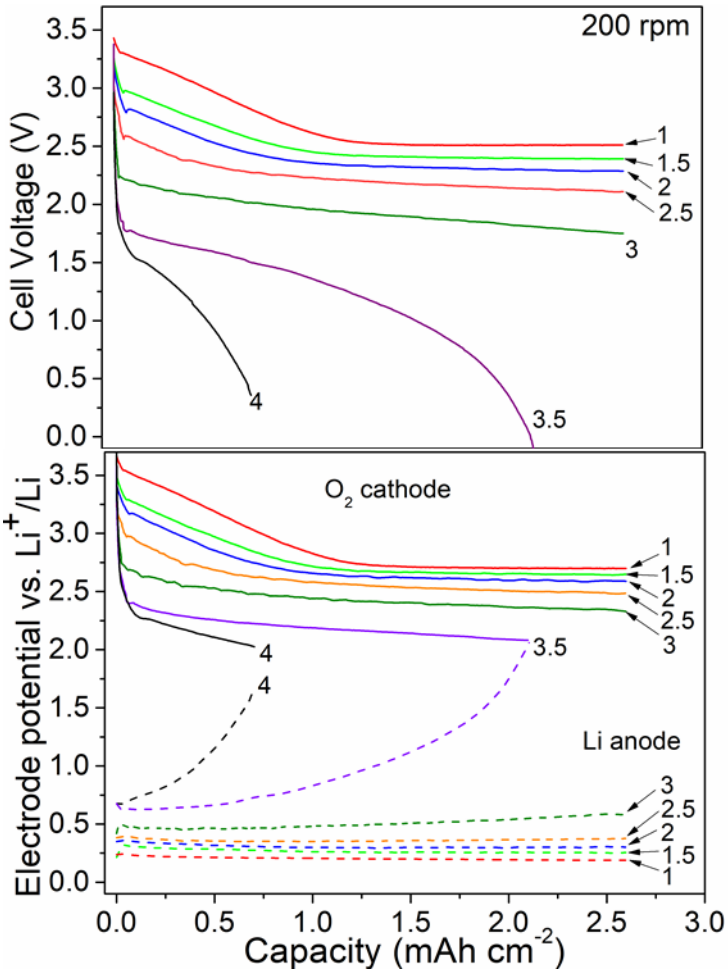

Figure 7.1.1. SLRFAB cell voltage and electrode potential profiles under galvanostatic discharges at different current densities (1-4 mA cm^{-2}). The capacity cut-off and cathodic potential cut-off were 2.6 mAh cm^2 and 2.00 V vs Li^+/Li, respectively. Reprinted and adapted from ref. (116), with permission from The Electrochemical Society. Copyright 2016.

At the current being 0.5 mA cm^{-2} and 200 rpm as pump rate, the cell voltage V_{cell} was 2.80 V (Figure 6.1.2.3) and the corresponding areal energy density, E_{areal}, is 555 mWh cm^{-2}, according to Equation 14:

$$E_{areal} = Q_{cell} \cdot V_{cell} \quad (14)$$

The specific energy ($E_{Li+Cath}$) and energy density ($E_{Li+Cath}$') that consider one the weight and the other the volume of Li and catholyte, can be thus calculated by the Equations 15-21:

$$E_{Li+cath} = E_{areal} (m_{Li} + m_{catholyte})^{-1} \quad (15)$$

$$E_{Li+cath}' = E_{areal} (V_{Li} + V_{catholyte})^{-1} \quad (16)$$

$$m_{Li} = t_{Li} \cdot d_{Li} \cdot 1\ cm^2, \quad (17)$$

$$V_{Li} = t_{Li} \cdot 1\ cm^2 \quad (18)$$

$$m_{catholyte} = 100 \cdot m_{SP}\ \%SP^{-1}, \quad (19)$$

$$V_{catholyte} = m_{catholyte}\ d_{cathoyte}^{-1}, \quad (20)$$

$$d_{catholyte} = d_{electrolyte} + \%SP\ 100^{-1} \quad (21)$$

The catholyte excess, as already reported, affects the specific energy and energy density of the not-balanced cell. Indeed, the values can be now calculated, resulting in 18.45 Wh kg^{-1} and 18.4 Wh L^{-1} ($d_{electrolyte}$ is 1 g cm^{-3}) for $E_{Li+Cath}$ and $E_{Li+Cath}$', respectively. Additionally, a proper cell balance requires that:

$$m_{SP} = Q_{Li} / Q_{SP}° = t_{Li} \cdot Q_{Li}° \cdot d_{Li} \cdot 0.8 / Q_{SP}° = 0.63 \cdot t_{Li} \quad (22)$$

In Table 7.1.1, the last column shows that in the balanced SLRFAB cell, only 57 mg of SP and thus 2.8 g of catholyte are enough (total Li and catholyte mass 2.9 g). The corrisponding $E_{Li+cath}$ and $E_{Li+cath}$' values thus increase to 192 Wh Kg^{-1} and 192 Wh L^{-1}. A further increase of $E_{Li+cath}$ and $E_{Li+cath}$', considering the balanced SLRFAB cell, can be obtained by increasing the carbon content in the catholyte (wt.% carbon), as reported in Figure 7.1.2a (116).

A 10-fold rise by the increase of the carbon wt.% from 2% to 10% allows to reach the outstanding values of 1 kWh kg^{-1} and 1 kWh L^{-1}. As already mentioned, in the lab-scale prototype, RVC was used as current collector (CC), having a thickness of 0.5 cm (t_{cc}), density of 0.1 g cm^{-3} (d_{cc}), mass of 20 mg (m_{cc}) and volume of 0.19 cm^3 (V_{cc}) (see Table 7.1.1). The specific energy ($E_{Li+cath+cc}$) and energy density ($E_{Li+cath+cc}$') values that also include the CC mass and volume are calculated by the following equations:

$$E_{Li+cath+cc} = E_{areal} / (m_{Li} + m_{catholyte} + m_{cc}) \quad (23)$$

$$E_{Li+cath+cc}' = E_{areal} / (V_{Li} + V_{catholyte} + V_{cc}) \quad (24)$$

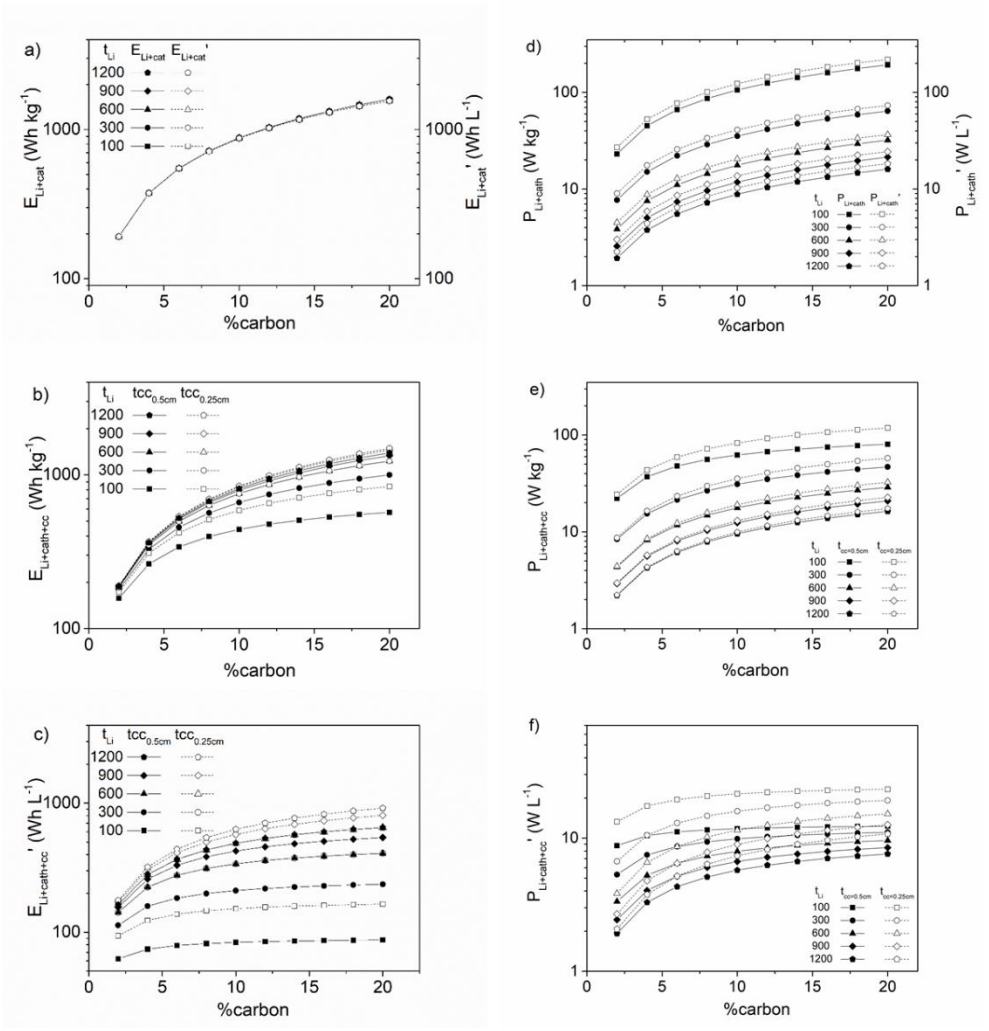

Figure 7.1.2. (a) Specific energy ($E_{Li+cath}$) and energy density ($E_{Li+cath}$') normalized to t_{Li} and catholyte mass and volume; (b-c) specific energy and energy density normalized to Li, catholyte and current collector mass or volume ($E_{Li+cath+cc}$ and $E_{Li+cath+cc}$'); (d) specific power ($P_{Li+cath}$) and power density ($P_{Li+cath}$') normalized to Li and catholyte mass and volume; (e-f) specific power and power density normalized to Li, catholyte and current collector mass or volume $P_{Li+cath+cc}$ and $P_{Li+cath+cc}$'. Reprinted and adapted from ref. (116), with permission from The Electrochemical Society. Copyright 2016.

The trends of $E_{Li+cath+cc}$ and $E_{Li+cath+cc}$' with carbon % for balanced SLRFAB, considering different t_{Li} (100-300-600-900-1200 μm) and t_{cc} (0.25-0.5 cm) are reported in Figure 7.1.2b and Figure 7.1.2c, respectively (116). The trends depend on both t_{Li} and t_{CC}, and specifically, the CC impact on the energy projections is more evident at the lowest t_{Li}.

At carbon %=12% and for t_{Li}=100 μm, for instance, $E_{Li+cath+cc}$ is 480 Wh kg^{-1} and indeed becomes 650 Wh kg^{-1} if t_{CC} is halved (t_{CC} = 0.25 cm). The CC mass contribution to $E_{Li+cath+cc}$ becomes negligible for t_{Li}> 600 μm (Figure 7.1.2b).

As found in $E_{Li+cath+cc}$, $E_{Li+cath+cc}$' dependence with t_{CC} decreases with the increase of t_{Li}. $E_{Li+cath+cc}$', for the lowest t_{Li} (100 μm), CC is limiting the performance to a value of 140-150 Wh L^{-1} at carbon %>6% but the value can double with t_{cc} = 0.25 cm. However, when t_{Li} is 1200 μm and carbon %=12, $E_{Li+cath+cc}$' is 530 Wh L^{-1} with t_{cc} of 0.5 cm and increses by only 30 % (700 Wh L^{-1}) once have halved the t_{cc} (Figure 7.1.2c) (116).

Furthermore, according to Figure 7.1.1, the highest areal power density value (P_{areal}) of the SLRFAB lab-scale prototype is achieved at 4 mA cm^{-2} and corresponds to 6.5 mW cm^{-2}, according to Equation 25:

$$P_{areal} = i \cdot V_{cell}, \qquad i = \text{current density} \qquad (25)$$

The above reported value has been then used to project the power performance of the balanced SLRFAB with increased %carbon, considering different both t_{Li} and t_{CC}. As first done to project the $E_{Li+cath}$ and $E_{Li+cath}$'

values, the data have been first normalized only to Li and catholyte mass and volume, as by Equation 26 and Equation 27:

$$P_{Li+cath} = P_{areal} (m_{Li} + m_{catholyte})^{-1} \quad (26)$$

$$P_{Li+cath}' = P_{areal} (V_{Li} + V_{catholyte})^{-1} \quad (27)$$

The results are reported in Figure 7.1.2d. Unlike the $E_{Li+cath}$ and $E_{Li+cath}'$, the $P_{Li+cath}$ and $P_{Li+cath}'$ values are instead strongly affected by t_{Li}. As a comparison, considering 12% of carbon dispersed in the catholyte (carbon % = 12%), $P_{Li+cath}$ and $P_{Li+cath}'$ are 12.2 W kg^{-1} and 12 W L^{-1} and 146 W kg^{-1} and 144 W L^{-1} for t_{Li} = 1200 μm and 100 μm, respectively. Furthermore, Figure 7.1.2e and Figure 7.1.2f show the values considering the total mass and volume of Li, catholyte and CC (Equation 28 and Equation 29) (116).

$$P_{Li+cath+cc} = P_{areal} / (m_{Li} + m_{catholyte} + m_{cc}) \quad (28)$$

$$P_{Li+cath+cc}' = P_{areal} / (V_{Li} + V_{catholyte} + V_{cc}) \quad (29)$$

At 12% of carbon in the catholyte and t_{Li}= 100 μm, the $P_{Li+cath+cc}$ is 68 W kg^{-1} for t_{cc}=0.5 cm, while it becomes 93 W kg^{-1}, with t_{cc}=0.25 cm. The current collector size affects the $P_{Li+cath+cc}$ only for t_{Li} < 600 μm. As it concerns $P_{Li+cath+cc}'$, the highest values of 18-21 W L^{-1} are achievable with 5-8% of carbon and using t_{Li}= 100 μm and t_{cc}=0.25 cm. For t_{Li}= 1200 μm, $P_{Li+cath+cc}'$ is only 8.3 W L^{-1}, with 12% of carbon and t_{cc}=0.25 cm. As

suggested above, the energy and power of the SLRFAB can be considered as decoupled, i.e. the main feature of the RFBs. Specifically, 1 kWh kg^{-1} ($E_{Li+cath+cc}$) and 700 Wh L^{-1} ($E_{Li+cath+cc}$') might be achievable by using t_{Li}= 1200 μm, t_{cc}= 0.25 cm and 12% of carbon. The highest projected $P_{Li+cath+cc}$ and $P_{Li+cath+cc}$' of 70 W kg^{-1} and 20 W L^{-1} could be obtained instead with a thin t_{Li}= 100 μm, t_{cc}= 0.25 cm and 6-8% of carbon.

7.2 Conclusions

The study reported in Chapter 7 points to the projected value of the SLRFAB in terms of energy and power, once have demonstrated that the lab-scale prototype of the SLRFAB reported in Paragraph 6.1.2 of this PhD thesis was not mass balanced in terms of Li/catholyte charge (mAh) (Table 7.1.1).
According to the calculation of the SLRFAB with Li/catholyte balanced, the higher is the percentage of carbon dispersed in the catholyte, the higher are both gravimetric and volumetric performance of the energy and power, as suggested in Figure 7.1.2a and Figure 7.1.2d. A great rise of the SLRFAB performance is predicted increasing the carbon wt.% up to 10-12%. At higher carbon %, the energy and power value slightly increase. This is due considering that the small increase in energy and power value with carbon % > 12% is counterbalanced by the higher viscosity of the slurry, that causes an increase in the energy spent by the pump to flow the catholyte. A part from the catholyte formulation, the thicknesses of both Li and current collector are key factors for the SLRFAB and the energy and power projections have been then simulated taking in consideration both, as reported in Figure 7.1.2b, Figure 7.1.2c, Figure 7.1.2e and Figure 7.1.2f. The results suggest that if the

current collector thickness is small, i.e. 0.25 cm, it does not dramatically affect the energy and power of the SLRFAB featuring a Li thickness higher than 600 μm.

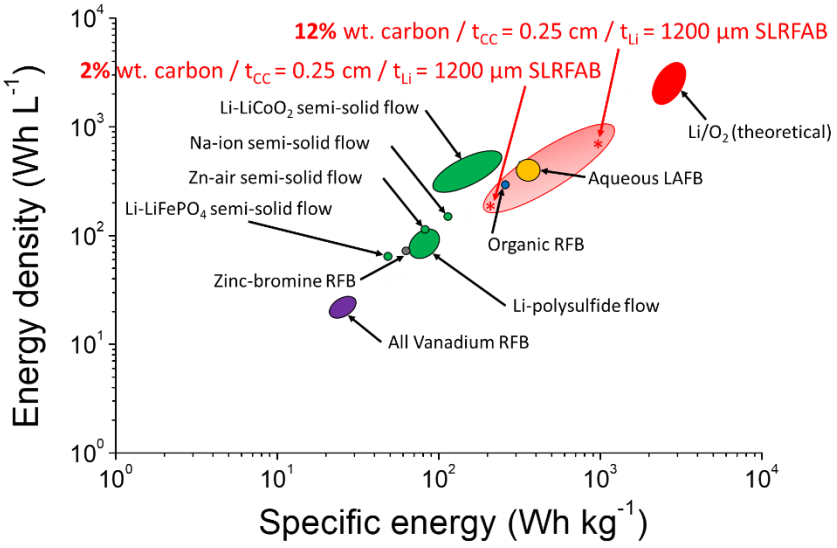

Figure 7.2.1. Projection energy density and specific energy of different flow battery, the theoretical not-flow Li/O_2 battery and SLRFAB (2% wt. carbon or 12% wt. carbon /0.25 cm-thick current collector and 1200 μm-thick Li). Reprinted and adapted from ref. (99), with permission from Elsevier.

Lastly, Figure 7.2.1 compares the projected energy value of the SLRFAB in terms of specific energy and energy density with the theoretical target of the Li/O_2 battery and other flow batteries proposed in the literature, included semi-solid redox flow batteries and Li redox flow air battery (Paragraph 1.7 and Paragraph 1.8) (99). The Figure shows how the SLRFAB values outperform all the other projected ones, demonstrating that it can be an effective strategy to boost up the energy content of the batteries.

Chapter 8 Novel carbonaceous catholyte for SLRFAB

Chapter 8 reports a study on the electrochemical performance of different formulations of carbon-based catholyte of SLRFAB in the glass electrochemical cell, where the catholytes were fed with O_2 and continuously stirred. The catholytes are made of two different carbon black (Super-P® and Pureblack®) and different weight percentages, added to the 0.5m LiTFSI in TEGDME electrolyte (0.5m). The electrochemical performance are discussed considering the electronic conductivity, morphology and rheological properties of the different catholyte formulations.

8.1 How conductivity, morphology and rheological properties of the catholytes affect the electrochemical performance

As already discussed in Chapter 6 and Chapter 7, the use of a semi-solid catholyte in a flow Li/O_2 batteries is a powerful strategy to improve the battery performance. The catholyte permits to increase the energy of the battery, delaying the carbon electrode passivation. Outstanding values of current density not achieved in conventional air breathing Li/O_2 cells can be obtained because the percolating network multiplies the redox sites.

In the SLRFAB, the capacity depends only on the carbon content in the liquid electrode, being the component that is passivated during the battery operation. As suggested in Chapter 7, the increase of the carbon content in the catholyte allows the enhancing of the SLRFAB energy. However, the use of high-carbon content catholyte is challenging because its carbon amount affects the viscosity of the slurry, decreasing the energy produced by SLRFAB.

Indeed, it is necessary to find the best compromise between the energy output of the SLRFAB and that energy amount, spent by the pump required to flow the catholyte. In this contest, the rheological, conductive and morphological properties of the investigated catholytes are important features that have to be well thought-out for the development of semi-solid flow batteries with high-energy content. These features dramatically depend on the morphology of the carbon nanostructure and on their surface chemistry, which affect the carbon agglomeration in the media (117), (118), (119), (128), (121).

In this PhD thesis, semi-solid catholytes based on two carbon black particles, being SP and Pureblack® 315 (PB) have been studied and the electronic conductivity, morphology and rheological properties are discussed in order to better explain the obtained electrochemical results. As already reported in Paragraph 2.1, the catholyte studied were 2SP and SP5, the latter only in relation to the rheological performance and featuring 2wt.% and 5wt.% of SP, and PB2 and PB10 with 2 and 10wt.% of PB.

8.1.1 Electronic conductivity, morphology and rheological properties of the catholytes

In order to get insight into the different morphological features of SP and PB carbon, TEM analyses was performed and the images are reported in Figure 8.1.1.1a and Figure 8.1.1.1c. Figure 8.1.1.1b and Figure 8.1.1.1d show the HRTEM of both SP and PB (122), (123), (124).

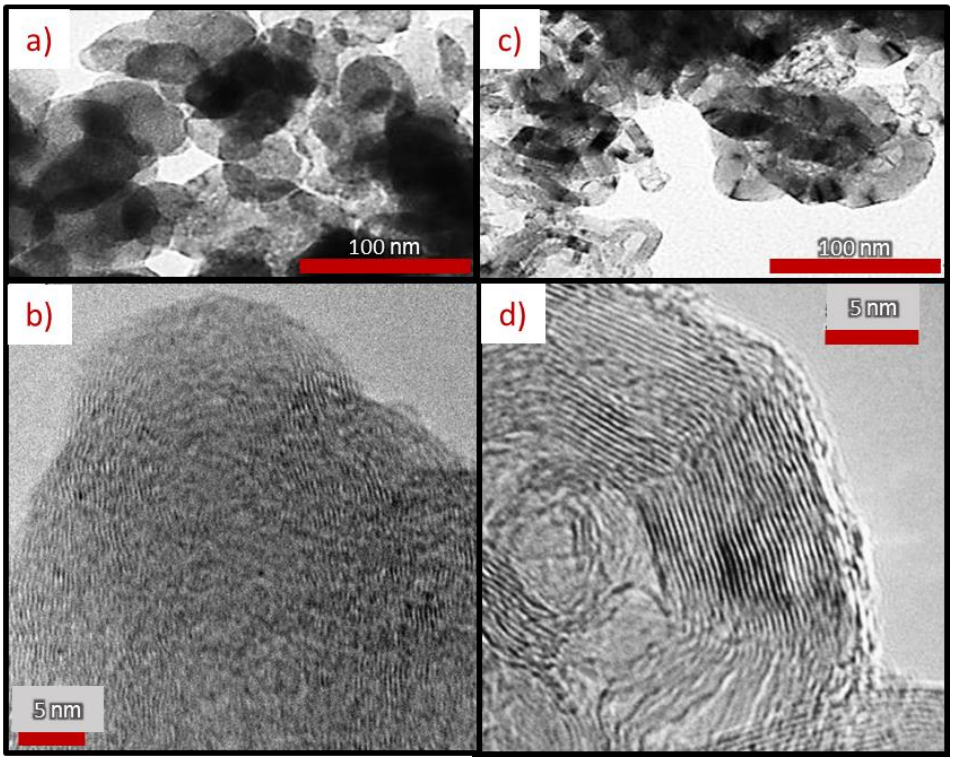

Figure 8.1.1.1. TEM images of (a) SP and (c) PB carbon. HRTEM images are also reported: (b) SP and (d) PB. Reprinted and adapted from ref. (122), ref. (123) and ref. (124), with permission from Elsevier.

Furthermore, the carbon agglomerates presented in the different catholytes have been also investigated by the optical fluorescence microscopy. The relative images are reported in Figure 8.1.1.2.

According to Figure 8.1.1.1, PB and SP are mainly made of particles of ca. 40 nm but while SP is mainly constituted by spherical and homogenous particles, BP has different shape and dimension. The PB particles indeed are even smaller than 40 nm with a higher graphitic planes content (122).

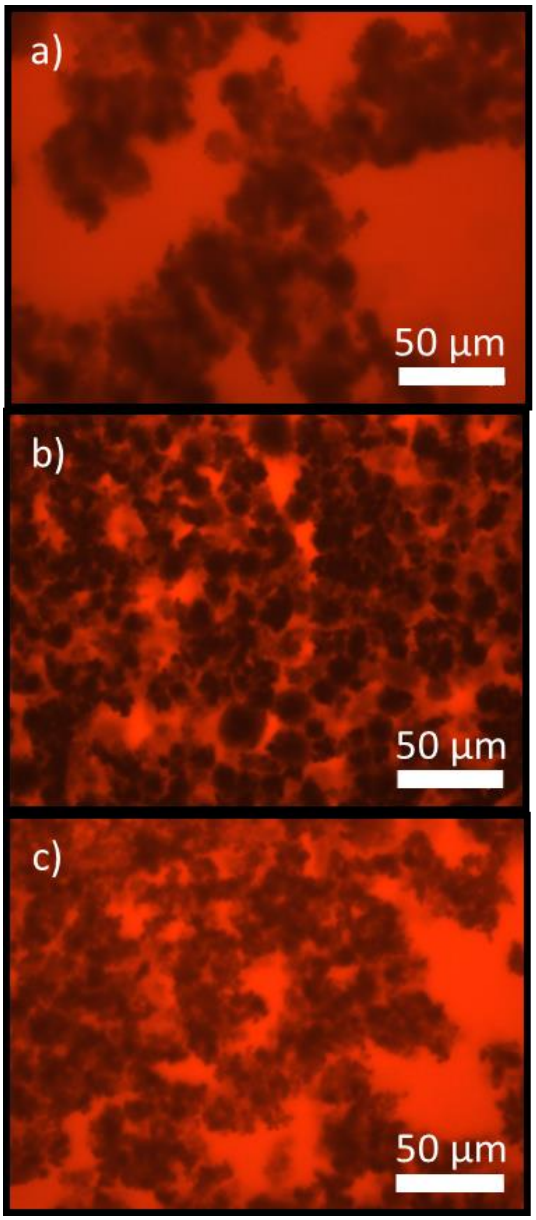

Figure 8.1.1.2. Optical fluorescence microscope images of (a) 2PB, (b) 10PB and (c) 2SP. Reprinted and adapted from ref. (122), with permission from Elsevier.

Additionally, the electronic conductivity of the percolating network (PN) is considered a key parameter for an efficient electron transfer across the catholyte, during the battery operation that permits to study the SLRFAB even at high current.

The electronic conductivity of the percolating network of the catholytes was measured at room temperature and the relative values of R_b, ρ, σ_{IC+PN} and σ_{PN} (catholyte resistance, resistivity, ionic and electronic catholyte conductivity) of 2PB, 2SP and 10PB, respectively, are reported in Table 8.1.1.1.

The σ_{PN} values have been obtained by subtracting the ionic conductivity (σ_{IC}) of 0.5m at room temperature (1.79 mS cm^{-1}) to the total ionic conductivity and electronic percolating network conductivity (σ_{IC+PN}) (103), (122).

Table 8.1.1.1. Electric properties of the catholytes with different carbons and carbon percentages. R_b = catholyte resistance; ρ = catholyte resistivity; σ_{IC+PN} = ionic and electronic PN conductivity; σ_{PN} = electronic PN conductivity.

	2PB	2SP	10PB
R_b (Ω)	706	536	301
ρ (Ω cm)	515	391	220
σ_{IC+PN} (mS cm^{-1})	1.95	2.55	4.66
σ_{PN} (mS cm^{-1})	0.16	0.76	2.87

Lastly, the rheological properties of the 2PB, 2SP and 10PB catholytes have been investigated. According to the Newton's law, viscosity (η) is correlated to the shear rate ($\dot{\gamma}$) and the shear stress (τ):

$$\tau = \eta \cdot \dot{\gamma} \quad (30)$$

Particle shape, dimension, quantity and attraction or repulsion forces with the dispersant agent are key factors that affect the rheological performance of a carbon-based catholyte during the application of an external shear stress. The obtained values of viscosity of the catholytes, in relation to a shear rate (from 0 to 200 s^{-1}) are reported in Figure 8.1.1.3 (122).

5SP (5 wt. % SP added to the electrolyte) was also characterized and it is clear that its rheological behaviour deters any use in semi-solid flow electrode application. Indeed, as a comparison, at 200 s^{-1}, 5SP is 3 times higher viscous than 2SP (0.136 Pa s vs. 0.06 Pa s). For this reason the electrochemical performance of the cell with 5SP as catholyte were not evaluated.

While 2PB features a quasi-newtonian behaviour (constant and low viscosity of ca. 0.01 Pa s), 2SP, 5SP and 10PB catholytes have a shear-thinning behaviour, i.e. the viscosity η decreases and a non-linear increase of the shear stress (τ) takes place with the shear rate ($\dot{\gamma}$).

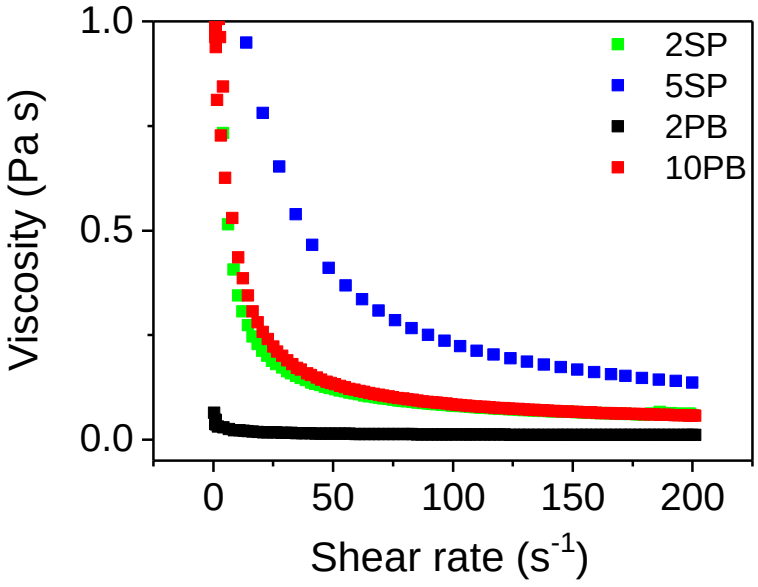

Figure 8.1.1.3. Viscosity (η) vs. shear rate $(\dot{\gamma})$ of the 2SP, 5SP, 2PB and 10PB catholytes. The shear rate $(\dot{\gamma})$ varied from 0 to 200 s^{-1} with 0.2 s^{-1} as sweep rate. Reprinted from ref. (122), with permission from Elsevier.

8.1.2 Effect of catholyte formulation on the electrochemical performance

Polarization tests at constant current were performed in order to electrochemically characterize the 2SP, 2PB and 10 PB.

The study was carried out in the electrochemical glass cell and the catholytes were continuously fed with O_2 and stirred. The test consisted in repetition of galvanostatic discharges from 0.25 mA cm^{-2} to 4.50 mA cm^{-2} with 0.25 mA cm^{-2} as step, 1 h as duration, and 2 mAh cm^{-2} and 2.00 V vs. Li^{+}/Li as capacity as cathodic potential cut-off.

Figure 8.1.2.1 reports the trends of the CP electrode potentials in the different catholytes. The CP/catholyte open circuit potentials were 2.70, 2.90

and 3.25 V vs. Li^+/Li before the test, for PB2, SP2 and PB10, respectively (122).

At 0.25 mA cm^{-2}, the CP potentials were 2.32, 2.47 and 2.74 V vs. Li/Li^+ for PB2, SP2 and PB10. While the potential reached the cut-off of 2.00 V vs. Li^+/Li at 0.50 mA cm^{-2} and 0.75 mA cm^{-2} for the SP2 and PB2 catholyte, the use of PB10 permitted to use current densities higher than 4 mA cm^{-2}.

At 4.50 mA cm^{-2}, the potential of CP with PB10 was almost 300 mV above the cut-off, i.e. 2.27 V vs. Li^+/Li.

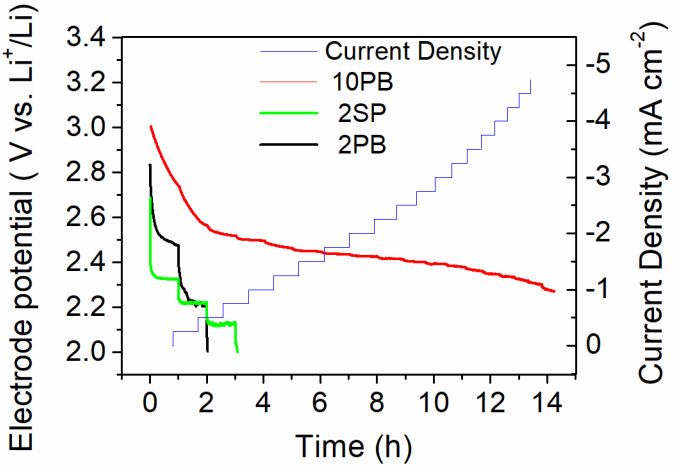

Figure 8.1.2.1. CP (0.5 cm^2) potential in the cell with 2SP, 2PB and 10PB as catholyte during 1h-discharge steps from 0.25 mA cm^{-2} to 4.50 mA cm^{-2} with 1 h and 2 mAh cm^{-2} as time and areal capacity limit. The catholytes were fed with O_2 and stirred. Reprinted from ref. (122), with permission from Elsevier.

Furthermore, in the carbon-based catholyte, beside the faradaic reaction of the ORR, a non-faradaic process related to the charge separation at the carbon/electrolyte interface occurs. The constant current technique cannot separate the two contributions.

Chronoamperometric measurements (i.e. constant potential) were performed, because here the output current is only related to faradaic reactions, i.e. the ORR process (108). The test consists of potential steps (PSs) of 100 mV from 2.90 to 2.00 V vs. Li^+/Li of the CP electrode, with 5h and 2 mAh cm^{-2} as time and capacity limit.

The output currents have been normalized to the surface of CP (0.5 cm^{-2}) and are reported in Figure 8.1.2.2, in relation to the set electrode potential (122).

By the use of the 10PB catholyte, higher currents are achievable. At 2.30 V vs. Li^+/Li, for instance, the current densities were 0.60, 1.00 and 2.25 mA cm^{-2} for 2PB, 2SP and 10PB, respectively.

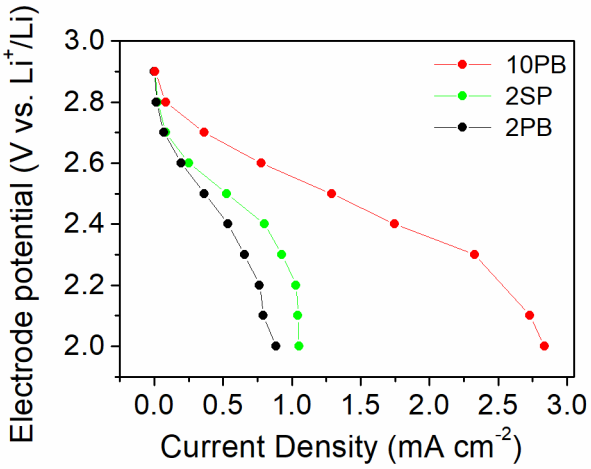

Figure 8.1.2.2. CP discharge polarization curves with 2SP, 2PB and 10PB catholyte obtained by PSs from 2.90 V vs. Li^+/Li to 2.00 V vs. Li^+/Li with time and capacity cut-off of 5h and 1 mAh; the output current has been normalized to the CP surface (0.5 cm^2). Reprinted from ref. (122), with permission from Elsevier.

8.1.3 Discussion

As suggested in Paragraph 8.1.2, the increasing of the PB carbon content decreases the overpotentials, enabling a CP potential of 2.70 V vs. Li^+/Li at 4.50 mA cm^{-2} in the 10PB catholyte (Figure 8.1.2.1).

Furthermore, the use 10PB, which is a high-carbon content catholyte, decreases the ohmic losses in the middle-range current regime and increases the output current during the chronoamperometric test (Figure 8.1.2.2).

Considering that the catholytes have been only stirred to simulate the flow condition in a glass electrochemical cell with a low-cost CP current collector, the results of the 10PB are promising.

2PB and 2SP catholytes featured similar electrochemical response: the cell with 2SP reached the CP potential cut-off at 0.75 mA cm^{-2} and with 2PB at 0.5 mA cm^{-2} (Figure 8.1.2.1), and the output current density at 2.00 V vs. Li/Li^{+} for 2SP was ca. 1 mA cm^{-2} and ca. 0.75 mA cm^{-2} for 2PB (Figure 8.1.2.2).

The electrochemical performance can be related to the electrical, morphological and rheological properties of the investigated catholytes.

The carbon nature affects the $\sigma_{PN.}$ Indeed, according to Table 8.1.1.1, 2SP σ_{PN} has a σ_{PN} value 5 times higher than that of 2PB, i.e. 0.76 mS cm^{-2} vs. 0.16 mS cm^{-2}, explaining why 2SP featured better electrochemical performance than 2PB (Figure 8.1.2.1). 10PB has the highest σ_{PN} value, being 2.87 mS cm^{-2}, which is more than 10 times higher than the other ones.

The good operation of the PN mainly lies in the disposition of the carbon arrays along the liquid media. According to the optical fluorescence microscope images, bigger and not dispersed agglomerates of carbon that do not occupy the whole volume constitute the 2PB catholyte (Figure 8.1.1.2a). This can explain the low electrochemical performance of 2PB of Figure 8.1.2.1 and Figure 8.1.2.2.

In 10PB catholyte, the carbon aggregates are more uniform and homogeneous in a condition similar to the 2SP (Figure 8.1.1.2b and Figure 8.1.1.1c), making the percolating network so much efficient that its conductivity increases and the electrochemical performance are ameliorated.

As already suggested, TEM shows that the SP and PB carbon present radically different morphologies (Figure 8.1.1.1). This bring about the conclusion that, considering the same carbon content, i.e. 2% wt., the fragmental and fractured nature of PB particles accounts for less ordered

networks in the catholyte, where isolated clusters are formed (Figure 8.1.1.2a).

On the other hand, in 10PB (amount of carbon 5 times higher than 2PB), the smaller particles are placed between the bigger ones. This create a compacted and continuous network, where the electronic conductivity is outperforming (Figure 8.1.1.2b). Because the different nature of the carbon, not only the electronic conductivity of PN is improved but also the rheological performance. Indeed, by only change the carbon, passing from SP to PB, a high-carbon content catholyte with 10%wt. of carbon has been obtained, thus increasing the energy content.

While the SP percentage higher than 5% provides catholyte viscosity very high that does not permit an easy management of the flow, the 2SP and 10 PB display similar viscosities, even though the latter features electrochemical outperforming results, as reported in Figure 8.1.1.3. This can be due to the smaller particles of PB that can behave like lubricant where the bigger particle can easily flow (119), (121).

8.2 Conclusions

According to the indication suggested in Chapter 7, a catholyte with high carbon content can increase the performance of SLRFAB. In Chapter 8, a range of catholytes has been investigated, using different carbon (Super-P and Pureblack, SP and PB respectively) and carbon contents (2 or 10 %).

The study points out that the morphology, rheology and electrical conductivity of the catholytes, reported in Paragraph 8.1.1, affect the electrochemical performance (Paragraph 8.1.2). By the use of PB carbon, it

has been possible to obtain and characterize an high carbon content catholyte, featuring similar rehological properties of the catholyte based on 2% of SP, with a relative positive contribution of the battery performance (Figure 8.1.2.1 and Figure 8.1.2.2) and SLRFAB energy content.

The electrochemical investigation has been done in electrochemical glass cell with the catholytes continuosly fed with O_2 and stirred. At 4.5 mA cm^{-2}, the current collector potential was above 300 mV respect its cut-off of 2.00 V vs. Li^+/Li, while with the other catholytes (2% of SP and 2% of PB) in the same conditions, the current collector reached the limit at current density < 1 mA cm^{-2}.

Moreover, the high-conductive percolating network of the catholyte based on 10% of PB cuts down any ohmic loss during the electrochemical test reported in Figure 8.1.2.1 and Figure 8.1.2.2.

Chapter 9 Conclusions

In this PhD thesis, in order to increase the battery performance of the Li/O_2 system, two strategies have been pursued. The first was the use of a novel concept of electrolyte based on superconcentrated solution of lithium bis(trifluoromethanesulfonyl)imide (LiTFSI) in tetraethylene glycol dimethyl ether (TEGDME) and the second was the use of a novel cell configuration that operates with a O_2-saturated carbon-based semi-solid catholyte.

Salt concentration has an impact on the ORR intermediates and products stability. Li_2O_2 formation mechanism is prone to change from a surface to a solution process moving from conventional low-concentrated solution to solvent-in-salt (SIS) solutions (molar ratio of the salt is the same or higher than the molar ratio of the solvent) based on LiTFSI and TEGDME.

Cycling stability of Li/O_2 batteries can be thus improved using these superconcentrated solutions because the fast passivation of the cathode that usually occurs in Li/O_2 batteries with conventional low-concentrated solution is delayed.

Furthermore, the use of Poly-Ionic-Liquids as binder for Li/O_2 battery cathode and as protective layer on Li to prevent the dendrite growth is an interesting approach. However, additional tests by the use of different techniques are required to better understand the effective mechanisms.

If the use of the SIS in Li/O_2 battery can be a attractive strategy for a novel designed electrolyte, as already mentioned, a novel semi-solid lithium redox flow air (O_2) battery (SLRFAB) technology has been also proposed.

ORR mainly takes place at the carbon particles that are dispersed in the catholyte. This process reduces the fast clogging of the cathode current collector that is caused by the deposition of Li_2O_2. The result is a dramatic increase of discharge capacity in terms of mAh cm^{-2} up to values never before reported for Li/O_2 cathodes.

The concept has been demonstrated by low cost, commercial material widely used in conventional Li/O_2 air-breathing cell and the catholyte consisted of 2% wt. of Super-P added to 0.5 m LiTFSI in TEGDME.

During the electrochemical test, Li has limited the cell response at high discharge currents because of its overpotential. Li interface optimization and SEI stabilization are issues that still remain not totally overcome in order to fully exploit the feasible SLRFAB.

Practical and projected performances of SLRFAB in terms of specific energy (Wh kg^{-1}), energy density (Wh L^{-1}) and power (W kg^{-1}, W L^{-1}) have been also simulated, taking into account the balancing of the Li and catholyte mass ratio, Li thickness, % of carbon dispersed in the catholyte and current collector thickness. In a certain way, the higher is the carbon content the higher are the energy and power performance.

However, catholytes with high carbon content and with peculiar features can be obtained only selecting the proper carbon, with particulary attention to the rheological and conductive properties.

A study on different catholyte formulation, in terms of selection of carbon and of its percentage in the catholyte, has been then performed. The highest pergentage (10 % wt.) of carbon dispersed in the 0.5 m LiTFSI in TEGDME has been obtained with Pureblack carbon. The particular features of this catholyte permitted to increase the energy content of the SLRFAB and the

electrochemical results have been explained considering the conductive, morphological and rheological features.

However, deeper fluid dynamic studies are required for a smart design of the SLRFAB considering the pressure drop and the energy spent to lead the flow of the catholyte.

Bibliography

1. Chen H, Cong TN, Yang W, Tan C, Li Y, Ding Y. *Prog Nat Sci*. 19 (2009) 291-312, DOI 10.1016/j.pnsc.2008.07.014.
2. Stock A, Stock P, Sahajwalla V. Powerful Potential: Battery Storage for Renewable Energy and Electric Cars. Climate Council of Australia Ltd, ISBN: 978-0-9944195-3-8, 2015
3. Kempener R, Borden E. Battery storage for renewables: market status and technology outlook. International Renewable Energy Agency (IRENA), 2015.
4. Cloonan G, Unger S. The world energy perspectives – E-mobility: Closing the emissions gap. World Energy Council, ISBN: 978-0-946121-48-9, 2016.
5. KPMG's Global Automotive Executive Survey 2017, © 2017 KPMG International Cooperative, (2017) 1-56, DOI 132042.
6. Scrosati B, Garche J, Tillmetz W. Advances in Battery Technologies for Electric Vehicles. In: Woodhead Publishing Series in Energy, Elsevier Ltd, 2015.
7. Yoo HD, Markevich E, Salitra G, Sharon D, Aurbach D. Mater Today 17 (2014) 3, 110-121, DOI 10.1016/j.mattod.2014.02.014.
8. a) Van Noorden R. Nature 507 (2014) 7490, 26-28, DOI 10.1038/507026a. b) Scosati B. J Solid State Electrochem (2011) 15, 1623–1630, DOI 10.1007/s10008-011-1386-8.
9. Zhang H, Li X, Zhang H. Li – S and Li – O_2 Batteries with High Specific Energy Research and Development, Springer Nature, Singapore 2017, DOI 10.1007/978-981-10-0746-0_1.
10. Lin D, Liu Y, Cui Y. Nature Nanotechnology 12 (2017) 3, 194-206, DOI 10.1038/nnano.2017.16.
11. Rao MLB. US Parent 3413154 (1968).
12. Rauh RD, Abraham KM, Pearson GF, Surprenant JK, Brummer SB. J Electrochem Soc. 126 (1979) 4, 523-527, DOI 10.1149/1.2129079.
13. Choi JW, Aurbach D. Nat Rev Mater. 1 (2016) 4, 16013, DOI 10.1038/natrevmats.2016.13.
14. https://oxisenergy.com/
15. Abraham KM, Jiang Z. J Electrochem Soc. 143 (1996) 1, 1-5, DOI 10.1149/1.1836378.
16. https://arpa-e.energy.gov/?q=pdfs/beest-polyplus

17. Julien C, Mauger A, Vijh A, Zaghib K, Lithium Batteries Science and Technology, Springer International Publishing, 2016, DOI 10.1007/978-3-319-19108-9_10.
18. Kordesch K, Taucher-Mautner W, Encycl. Electrochem. Power Sources, Elsevier, New York 2009, DOI 10.1016/B978-044452745-5.00003-4.
19. Jasinski R, High-energy batteries, 1967 Springer US.
20. Peled E. J. Electrochem. Soc. 126 (1979) 2047, DOI 10.1149/1.2128859.
21. Peled E, Menkin S. J. Electrochem. Soc. 164 (2017) A1703–A1719, DOI 10.1149/2.1441707jes.
22. Wang A, Kasam S, Li H, Shi S, Qi Y. npj Computational Materials 4 (2018) 15, DOI 10.1038/s41524-018-0064-0.
23. X.B. Cheng, R. Zhang, C.Z. Zhao, F. Wei, J.G. Zhang, Q. Zhang. Adv. Sci. 3 (2015) 1500213, DOI 10.1002/advs.201500213.
24. Braga MH, Grundish NS, Murchisona AJ, Goodenough JB. Energy Environ. Sci., (2017) 10, 331.
25. Guo Y, Li H, Zhai T. Adv Mater. 29 (2017) 29, 1-25, DOI 10.1002/adma.201700007.
26. Harry KJ, Hallinan DT, Parkinson DY, MacDowell A, Balsara NP. Nat Mater. 13 (2014) 1, 69-73, DOI 10.1038/nmat3793.
27. Li F, Zhang T, Yamada Y, Yamada A, Zhou H. Adv. Energy Mater. 3 (2013) 532.
28. Suo L, Hu YS, Li H, Armand M, Chen L, Nature Comm. 4, 1-9.
29. Mecerreyes D. Progress in Polymer Science 36 (2011) 1629–1648.
30. Delhorbe V, Bresser D, Mendil-Jakani H, Rannou P, Bernard L, Gutel T, Lyonnard S, Picard L. Macromolecules (2017) 50, 4309−4321.
31. Yuan J, Mecerreyes D, Antonietti M. Prog Polym Sci. 2013, DOI 10.1016/j.progpolymsci.2013.04.002.
32. Zhang S, Zhang Q, Zhang Y, Chen Z, Watanabe M, Deng Y. Prog Mater Sci. (2016) 77, 80-124, DOI 10.1016/j.pmatsci.2015.10.001.
33. Kerner M, Johansson P. Batteries 4 (2018) 10, DOI 10.3390/batteries4010010.
34. Li Y, Lu J. ACS Energy Lett. 2 (2017) 6, 1370-1377, DOI 10.1021/acsenergylett.7b00119.

35. Galbraith A. “The Lithium-Water-Air Battery for Automotive Propulsion”, in 4th International Electric Vehicle Symposium, Duesseldorf, West Germany (1976).
36. Ogasawara T, Debart A, Holzapfel M, Novak P, Bruce PG. J. Am. Chem. Soc. 128 (2006) 1390–1393.
37. Scrosati B, Abraham KM, van Schalkwijk W, Hassoun J. Lithium Batteries: Advanced Technologies and Applications Wiley 2013, ISBN: 978-1-118-18365-6.
38. Xu W, Xu K, Vilayanur V, Viswanathan, Townea SA, Hardy JS, Xiao J, Nie Z, Huc D, Wang D, Zhang JG. Journal of Power Sources, 196 (2011) 22, 9631-9639.
39. Balaish M, Kraytsberg A, Ein-Eli Y. Phys Chem Chem Phys. 16 (2014) 7, 2801-2822, DOI 10.1039/C3CP54165G.
40. Carboni M, Marrani AG, Spezia R, Brutti S. 165 (2018) 2, 1-9 DOI 10.1149/2.0331802jes.
41. Amanchukwu CV, Harding JR, Shao-Horn Y, Hammond PT. Chem Mater. 2015, DOI 10.1021/cm5040003.
42. Nasybulin E, Xu W, Engelhard MH, Nie Z, Li XS, Zhang JG. J Power Sources 2013, DOI 10.1016/j.jpowsour.2013.06.097.
43. Papp JK, Forster JD, Burke CM, Kim HW, Luntz AC, Shelby RM, Urban J, Jeffrey j, McClonskey BD.
J Phys Chem Lett. 2017, DOI 10.1021/acs.jpclett.7b00040.
44. Laoire CO, Mukerjee S, Abraham KM, Plichta EJ, Hendrickson MA. J Phys Chem C. 2010, DOI 10.1021/jp102019y.
45. Pearson RG. J. Am. Chem. Soc., 85 (1963) 21, 3533.
46. Laoire CO, Mukerjee S, Abraham KM. J. Phys. Chem. C, 113 (2009) 20127.
47. Aurbach D, McCloskey BD, Nazar LF, Bruce PG. Nat Energy 2016,. DOI 10.1038/nenergy.2016.128.
48. Ganapathy S, Adams BD, Stenou G, Anastasaki MS, Goubitz K, Miao XF, Nazar LF, Wagemaker M. J Am Chem Soc. 136 (2014) 46, 16335-16344, DOI 10.1021/ja508794r.
49. Adams BD, Radtke C, Black R, Trudeau ML, Zaghib K, Nazar LF. Energy Environ Sci. 6 (2013) 1772, DOI 10.1039/c3ee40697k.
50. Gallant BM, Kwabi DG, Mitchell RR, Zhou J, Thompson C V., Shao-Horn Y. Energy Environ Sci. 2013, DOI 10.1039/c3ee40998h.
51. Mandai T, Yoshida K, Tsuzuki S, Nozawa R, Masu H, Ueno K, Dokko K, Watanabe M. J Phys Chem B. 119 (2015) 4, 1523-1534,

DOI 10.1021/jp508100s.
52. Bryantsev VS. Chem Phys Lett. 2013, DOI 10.1016/j.cplett.2012.12.066.
53. Khetan A, Pitsch H, Viswanathan V. J Phys Chem Lett. 2014 DOI 10.1021/jz501154v.
54. Murphy T, Callear SK, Yepuri N, Shimizu K, Watanabe M,. Canongia Lopes JN, Darwish T,. Warrf GG, Atkin R. Phys Chem Chem Phys. 18 (2016) 26, 17224-17236, DOI 10.1039/C6CP00176A.
55. Seki S, Serizawa N, Takei K, Tsuzuki S, Umebayashi Y, Katayama Y, Miura T, Dokko K, Watanabe M. RSC Adv. 6 (2016) 39, 33043-33047, DOI 10.1039/C6RA04404B.
56. Li F, Zhang T, Yamada Y, Yamada A, Zhou H. Adv Energy Mater. 3 (2013) 4, 532-538, DOI 10.1002/aenm.201200776.
57. Kwon HM, Thomas ML, Tatara R, Oda Y, Kobayashi Y, Nakanishi A, Ueno K, Dokko K, Watanabe M. ACS Appl Mater Interfaces. 9 (2017) 7, 6014-6021, DOI 10.1021/acsami.6b14449.
58. Grygiel K, Lee JS, Sakaushi K, Antonietti M, Yuan J. ACS Macro Letters 4 (2015) 12, 1312-1316.
59. Lee JS, Sakaushi K, Antonietti M, Yuan J. RSC Adv. 2015, DOI 10.1039/C5RA16535K.
60. Eshetu GG, Armand M, Scrosati B, Passerini S. Angew Chemie - Int Ed. 53 (2014) 49, 13342-13359, DOI 10.1002/anie.201405910.
61. Von Zamory J, Bedu M, Fantini S, Passerini S, Paillard E. J Power Sources. 2013, DOI 10.1016/j.jpowsour.2013.04.127.
62. Ventosa E, Schuhmann W. Phys Chem Chem Phys. 17 (2015) 43, 28441-28450, DOI 10.1039/C5CP02268A.
63. Gunasekara I, Mukerjee S, Plichta EJ, Hendrickson MA, Abraham KM. J Electrochem Soc. 161 (2014) 3, A381-A392, DOI 10.1149/2.073403jes.
64. Schwager P, Fenske D, Wittstock G. J Electroanal Chem. 2015, 740, 82-87, DOI 10.1016/j.jelechem.2014.12.040.
65. Ravikumar MK, Rathod S, Jaiswal N, Patil S, Shukla A. J Solid State Electrochem. 21 (2017) 9, 2467-2488 DOI 10.1007/s10008-016-3472-4.
66. Dunn B, Kamath H, Tarascon J-M. Science 334 (2011) 6058, 928-935, DOI 10.1126/science.1212741.
67. Huang Q, Wang Q. ChemPlusChem 80 (2015) 312-322.
68. Soloveichik GL. Chem. Rev. 115 (2015) 11533–11558.

69. Darling RM, Gallagher KG, Kowalski JA, Ha S, Brushett FR. Energy Environ. Environ. Sci. 7 (2014) 3459–3477.
70. Leung P, Li X, Ponce de Leòn C, Berlouis L, Low CTJ, Walsh FC, RSC Adv. 2 (2012) 10125–10156.
71. Wang W, Luo Q, Li B, Wei X, Li L, Yang Z. Adv. Funct. Mater. 23 (2013) 970– 986.
72. Gong K, Fang Q, Gu S, Yau Li SF, Yan Y, Energy Environ. Sci. 8 (2015) 3515– 3530.
73. Skyllas-Kazacos M, Chakrabarti MH, Hajimolana SA, Mjalli FS, Saleem MJ. Electrochem. Soc. 158 (2011) R55–R79.
74. Perry ML, Weber AZ., Journal of The Electrochemical Society, 163 (2016) 1, A5064-A5067.
75. Wei TS, Fan FY, Helal A, Smith KC, McKinley GH, Chiang YM, Lewis JA. Adv. Energy Mater. 2015, 5, 1500535.
76. Wang C, Lai Q, Xu P, Li X, Zhang H. Chinese Chemical Letters 29 (2018) 716–718.
77. Monaco S, Soavi F, Mastragostino M. J Phys Chem Lett. 2013 4, 1379-1382, DOI 10.1021/jz4006256.
78. Zhao Y, Ding Y, Li Y, Peng L, Byron HR, Goodenough JB. Chem Soc Rev. 44 (2015) 22, 7968-7996, DOI 10.1039/c5cs00289c.
79. Zhu Y, Jia C, Yang J, Pan F, Huang Q, Wang Q. Chem Commun. 2015 51, 9451-9454, DOI 10.1039/C5CC01616A.
80. Bresser D, Paillard E, Passerini S. J Electrochem Sci Technol. 5 (2014) 2, 37-44, DOI 10.5229/JECST.2014.5.2.37.
81. Yang L, Frith JT, Garcia-Araez N, Owen JR. Chem Commun. 51 (2015) 9, 1705-1708, DOI 10.1039/c4cc09208b.
82. Appleby AJ, Jacquier MJ. J. Power Sources 1 (1976) 17–34.
83. Duduta M, Ho B, Wood VC, Limthongkul P, Brunini VE, Carter WC, Chiang YM. Adv. Energy Mater. 1 (2011) 511–516.
84. Jia C, Pan F, Zhu YG, Huang Q, Lu L, Wang Q. Sci. Adv. (2015), DOI 10.1126/sciadv.1500886.
85. Li Z, Smith KC, Dong Y, Baram N, Fan FY, Xie J, Limthongkul P, Carter WC, Chiang YM, Phys. Chem. Chem. Phys. 15 (2013) 15833–13839.
86. Hamelet S, Tzedakis T, Leriche JB, Sailler S, Larcher D, Taberna PL, Simon P, Tarascon JM. J. Electrochem. Soc. 159 (2012) A1360–1367.

87. Huang Q, Li H, Grätzel M, Wang Q. Phys. Chem. Chem. Phys. 15 (2013) 1793– 1797.
88. Youssry M, Madec L, Soudan P, Cerbelaud M, Guyimard D, Lestriex B. J. Power Sources 274 (2015) 424–431.
89. Hongning Chen, Nien-Chu Lai, and Yi-Chun Lu. Chem. Mater. 2017, 29, 7533−7542.
90. Soloveichik GL. Chem. Rev. 115 (2015) 11533–11558.
91. Dong K, Wang S, Yu J. RSC Adv. 4 (2014) 47517–47520.
92. Fan FY, Woodford WH, Li Z, Baram N, Smith KC, Helal A, McKinley GH, Carter WC, Chiang YM. Nano Lett. 14 (2014) 2210–2218.
93. Ventosa E, Buchholz D, Klink S, Flox C, Chagas LG, Vaalma C, Schuhmann W, Passerini S, Morante JR. Chem. Commun. 51 (2015) 7298–7301.
94. Presser V, Dennison CR, Campos J, Knehr KW, Kumbur EC, Gogotsi Y. Adv. Energy Mater. 2 (2012) 895–902.
95. Porada S, Lee J, Weingarth D, Presser V. Electrochem. Commun. 48 (2014) 178–181.
96. Boota M, Hatzell KB, Kumbur EC, Gogotsi Y. ChemSusChem 8 (2015) 835– 843.
97. http://24-m.com/
98. https://www.technologyreview.com/s/601500/24ms-batteries-could-better-harness-wind-and-solar-power/
99. Ruggeri I, Arbizzani C, Soavi F. Electrochim Acta. 2016 206, 291-300 DOI 10.1016/j.electacta.2016.04.139.
100. Bergner S, Vatsyayan P, Matysik FM. Anal Chim Acta. 2013 775, 1-13, DOI 10.1016/j.aca.2012.12.042.
101. Sun P, Laforge FO, Mirkin M V. Phys Chem Chem Phys. 9 (2007) 7, 802-823, DOI 10.1039/b612259k.
102. F. Messaggi. Electrolytes for Li/O_2 batteries, from salt-in-solvent to solvent-in-salt (2016).
103. Messaggi F., Ruggeri I., Genovese D., Zaccheroni N., Arbizzani C., Soavi F., Electrochimica Acta 245 (2017) 296–302.
104. Yoshida K, Tsuchiya M, Tachikawa N, Dokko K, Watanabe M. J. Phys. Chem. 115 (2011) 27, 18384-18394.
105. Mandai T, Yoshida K, Ueno K, Dokko K, Watanabe M. Phys. Chem. Chem. Phys., 2014 16, 8761-8772.

106. F. De Giorgio, F. Soavi, M. Mastragostino, Electrochem. Comm. 13 (2011) 1090.
107. S. Monaco, A.M. Arangio, F. Soavi, M. Mastragostino, E. Paillard, S. Passerini, Electrochim. Acta 83 (2012) 94.
108. A.J. Bard, L.R. Faulkner, Electrochemical Methods: Fundamentals and Applications, Applications, John Wiley & Sons, Inc, New York, USA, 2011.
109. Y. Nishikami, T. Konishi, R. Omoda, Y. Aihara, K. Oyaizu, H. Nishide, J. Mater. Chem. A 3 (2015) 10845.
110. O. Wijaya, P. Hartmann, R. Younesi, I.I.E. Markovits, A. Rinaldi, J. Janek, R. Yazami, J. Mater. Chem. A 3 (2015) 19061.
111. Giacco D., Carboni M., Brutti S, Marrani A. G., ACS Appl. Mater. Interfaces, DOI: 10.1021/acsami.7b05153.
112. Bobnar J, Lozinšek M, Kapun G, Njel C, Dedryvère R, Genorio B, Dominko R, Scientific Reports (2018) 8:5819.
113. F. Soavi, C. Arbizzani, I. Ruggeri, Patent WO2017021840A1.
114. G.A. Elia, J.-B. Park, B. Scrosati, Y.-K. Sun, J. Hassoun, Electrochem. Commun. 34 (2013) (2013) 250–253.
115. S. Freunberger, Y. Chen, N.E. Drewett, L.J. Hardwick, F. Bardé, P.G. Bruce, Angew. Chem. 50 (2011) 8609–8613.
116. F. Soavi, I. Ruggeri, C. Arbizzani, ECS Trans. 72 (2016) 1-9.
117. Youssry, L. Madec, P. Soudan, M. Cerbelaud, D. Guyomard, B. Lestriez, Phys. Chem. Chem. Phys. 15 (2013) 14476-14486.
118. Barnes HA. J. Non-Newtonian Fluid Mech. 70 (1997) 1-33.
119. Mueller S, Llewellin EW, Mader HM. Proc. R. Soc. A 466 (2010) 1201-1228.
120. Barrie CL, Griffiths PC, Abbott RJ, Grillo I, Kudryashov E, Smyth C. J. Colloid Interface Sci. 272 (2004) 210-217.
121. N. Willenbacher, K. Georgieva. Rheology of disperse systems, in: U. Bröckel, W. Meier, G. Wagner (Eds.), Product Design and Engineering, Wiley-VCH Verlag GmbH, Weinheim, 2013, 7-49.
122. Ruggeri I., Arbizzani C., Soavi F., Carbon 130 (2018) 749-757.
123. Wu CM, Pan PI, Cheng YW, Liu CP, Chang CC, Avdeev M, Lin SK. J. Power Sources 2017 314, 14-21, DOI 10.1016/j.jpowsour.2016.11.048.

124. Barsukov IV, Gallego MA, Doninger JE. J. Power Sources 153 (2006) 2, 288-299.